UNDERWATER COMMUNICATION CHANNEL CHARACTERIZATION IN THE SOUTHERN CALIFORNIA OFF-SHORE RANGE

BY

ARSEN ZOKSIMOVSKI

BS in Electrical Engineering,

University Of Novi Sad, Serbia and Montenegro, 2000

THESIS

Submitted to the University of New Hampshire

In Partial Fulfillment of

The Requirements for the Degree of

Master of Science

In

Electrical Engineering

December 2004

This thesis has been examined and approved.

Thesis Director, Christian de Moustier,
Professor

Kondagunta Sivaprasad,
Professor

Michael Carter,
Associate Professor

7 DECEMBER 2004

Date

ACKNOWLEDGEMENTS

I would like to express my gratitude and appreciation to Professor Christian de Moustier, my thesis advisor, who planned and directed the overall project and introduced me to the field of underwater acoustics, for his always-helpful suggestions and his support and guidance in all phases of this work.

I am also grateful to my colleagues from the Center for Coastal and Ocean Mapping at the University of New Hampshire, especially Daniel Brogan, for helping me resolve puzzles, inevitably encountered in research, and present the findings distinctly.

This thesis was much improved by sound propagation simulations, performed with the BELLHOP ray tracing software. I would like to thank Dr Michael B. Porter, from HLS Research Corporation, who made the software available, and to Dr Alec Duncan, from Curtin University of Technology, Australia, who wrote a MATLAB front-end version of the software and was very responsive to all my questions related to the application.

A part of this work (Chapter 5) was presented at the High Frequency Ocean Acoustics conference in La Jolla, California, 1 – 5 March 2004. [A. Zoksimovski and C. de Moustier, "Detection of direct-path arrivals for multi-narrowband sequences (3-30 kHz) in shallow water", in High Frequency Ocean Acoustics, AIP Conf. Proc. 728, pp. 478-488, 2004.]

For the experimental work that produced the data presented here, I wish to thank the Scripps Institution of Oceanography researchers who did the Feb. 2001 data collection, and Melissa Hock who compiled a preliminary report on these data.

The US Naval Oceanographic Office funded the data collection work. This thesis was supported in part by the Center for Coastal and Ocean Mapping (NOAA Grant NA170G2285) and by the Naval Oceanographic office through a grant administered by the Scripps Institution of Oceanography (Grant N00014-01-0370).

TABLE OF CONTENTS

ACKNOWLEDGEMENTS iii

LIST OF TABLES vii

LIST OF FIGURES ix

ABSTRACT xvii

C H A P T E R P A G E

INTRODUCTION 1

Motivation 1

Objective 2

Previous Work 2

Present Work 4

1. DESCRIPTION OF THE EXPERIMENT 8

2. POST-EVENT ANALYSIS 18

3. SONAR SIGNAL PROPAGATION 28

Tanner-Cortes Bank Site 29

South of China Point Site 41

San Nicolas Basin Site 45

Summary 55

4. BACKGROUND NOISE 56

Tanner-Cortes Bank Site 58

South of China Point Site 65

San Nicolas Basin Site 68

Summary 70

5. PULSE EXTRACTION 72

Summation of the Rectified Correlation Functions 79

Least Square Time Constraint 87

Summary 91

6. TRANSMISSION LOSS 93

Tanner-Cortes Bank Site 101

South of China Point Site 118

San Nicolas Basin Site 129

7. SUMMARY 140

Discussion 142

APPENDIX 147

A. RANGE-FREQUENCY VARIATION OF TRANSMISSION LOSS 148

LIST OF ABBREVIATIONS 150

LIST OF REFERENCES 152

LIST OF TABLES

Table 1.1 TL measurement schedule in February 2001. "Solid line" and "dashed line" refer to the sketches in Figure 1.2. 11

Table 1.2 Source depth and ship course schedules during the data collection; "solid line" and "dashed line" refer to the sketches in Figure 1.2; symbols "<" and ">" stand for "before" and "after", respectively; N, S, E, and W refer to North, South, East and West, respectively. 11

Table 3.1 Time differences among the clutter components from Figure 3.6. Source depth is 40 m and the range is 3 km. T_S=Surface reflection travel time; T_B=Bottom reflection travel time; T_{BS}=Bottom-Surface reflection travel time; T_{SB}=Surface-Bottom reflection travel time. 38

Table 3.2 Time differences among the clutter components similar to Figure 3.6. Source depth is 13 m and the range is 6 km. T_S=Surface reflection travel time; T_B=Bottom reflection travel time; T_{BS}=Bottom-Surface reflection travel time; T_{SB}=Surface-Bottom reflection travel time. 49

Table 4.1 Average slope (dB/oct) of the noise spectra from Figure 4.2. Negative range refers to the section before CPA. 62

Table 4.2 Average slope (dB/oct) of the noise spectra in Figure 4.5; negative range infers the section before CPA. 67

Table 4.3 Average slope (dB/oct) of the noise spectra in Figure 4.7. 70

Table 6.1 Near-field anomaly k_L (dB), and shallow water attenuation α_T (dB/bounce); data from Marsh and Shulkin [3]; sea state=3 [27]. 100

Table 6.2 Direct-path distances at the hydrophone depths, based on Figure 3.2 and Figure 3.3. nl = not limited. nr = not relevant; * ⇒ singularity. 101

Table 6.3 The skip distances computed with Equation 6.7 that correspond to the SSPs in Figure 3.1. 102

Table 6.4 Direct-path distances at the hydrophone depths, roughly estimated based on the analysis in Chapter 3 . nl = not limited. 118

Table 6.5 The skip distances computed with Equation 6.7 that correspond to the SSPs in Figure 3.8. 119

Table 6.6 Direct-path distances at the hydrophone depths, roughly estimated in Chapter 3. 130

LIST OF FIGURES

Figure 1.1 Region where the experiments were carried out. The rings show approximate positions of the three surveyed sites. 8

Figure 1.2 GPS coordinates of the ship along the data collection routes. Sign "-" means West in longitude. (a) Cortes-Tanner Bank (b) South of San Clemente Island's China Point (c) San Nicolas Basin. 9

Figure 1.3 Geometry of the experiment with moored sonobuoys. 12

Figure 1.4 Data acquisition frame-up. 13

Figure 1.5 (a) Source Level calibration of the ITC-1007 transducer and (b) Free Field Voltage Sensitivity calibration of the AN/SSQ-57B hydrophone. Measurements done at the US Navy's TRANSDEC facility in San Diego, CA. 13

Figure 1.6 FFVS calibration of the ITC-1042 reference hydrophone. Measurements done at the US Navy's TRANSDEC facility in San Diego, CA. 15

Figure 1.7 Spectrogram of the time series received in shallow water at a hydrophone for one transmission sequence (range ≅ 2 km). The trailing signals represent multipath arrivals. 16

Figure 1.8 Spectrogram of the time series received in deep water at a hydrophone for one transmission sequence (range ≅ 2 km). 17

Figure 2.1 Post event analysis elements. 18

Figure 2.2 Transfer function of a (a) FIR filter order 1000 and (b) IIR filter order 7. 21

Figure 2.3 Transmit sequence of pulses. Frequency of each pulse is higher than frequency of its neighbor on the left, following the arithmetical progressions 3 kHz to 12 kHz and 15 kHz to 30 kHz with 1 kHz and 3 kHz steps, respectively. 22

Figure 2.4 Pre-filtered transmit sequence at 10 kHz with: (a) 1000-order FIR filter (b) 2×3+1-order IIR filter. 23

Figure 2.5 Frequency response of a 10 ms CW pulse at 11 kHz and an FIR filter centered at 10 kHz, both 1000 points long. 24

Figure 2.6 The ripples at the time interval of the 11 kHz pulse for: (a) FIR pre-filter (b) IIR pre-filter. 25

Figure 2.7 Spectrogram of a 30 kHz pulse. Time unit is 1 second and frequency unit is 1 Hz. 26

Figure 3.1 SSP at the Tanner-Cortes Bank site, measured on February 20th 2001. 30

Figure 3.2 Ray tracing for the 6 AM SSP in Figure 3.1. The source depth, the span of the uniformly distributed starting depression angles and the corresponding number of beams are: (a) 19 m, -1° to 1°, 100 beams and (b) 40 m, -5° to 5°, 300 beams, with positive angles being read clockwise. The dashed beams highlight the longest estimated range with a direct-path arrival at 61 m depth. 32

Figure 3.3 A ray tracing diagram, assuming the noon SSP on 20th February 2001 at the Tanner-Cortes Bank site. The dashed line originates from a 19 m source, whereas source depth is 40 m for all the other rays. 33

Figure 3.4 (a) Simplified SSP from Figure 3.1 (b) Thin beams belong between the first angle that gives a direct path at 27 m and the smallest angle of incidence that does not produce the surface reflection. The two thick beams correspond to the first angle that gives a direct path and the sea surface reflected beam that intersects it at 27 m depth. 36

Figure 3.5 Time delay and range distribution for the direct and surface reflected beams that intersect at 27 m depth. 37

Figure 3.6 Clutter geometry under assumption of a constant sound speed throughout the water column; Water depth 116 m; the solid and dashed lines correspond to the 27 m and 61 m receiver depth, respectively. 39

Figure 3.7 Ray tracing for the 6 PM SSP in Figure 3.1 and source at depth 40 m. The starting angles of depression of the 300 selected beams are uniformly distributed inside -3 to 3 degrees window, with positive angles being read clockwise. The upper and the lower dashed beam signify the longest ranges with a direct-path arrival at 27 m and 61 m, respectively. 40

Figure 3.8 SSPs measured at noon and 6 PM on 24th and 19th February 2001, respectively, close to the sonobuoy locations at the South of China Point site. 42

Figure 3.9 Ray tracing for the early-afternoon SSP (Figure 3.8). The dashed beams for a source depth of 35 m and 60 m trace the longest direct-path ranges at 61 m and 27 m depth, respectively. 43

Figure 3.10 An early afternoon and a late afternoon SSP at the San Nicolas Basin site, measured on February 24th 2001. 45

Figure 3.11 (a) Part of the early afternoon SSP from Figure 3.10 (b) Ray tracing for source at 13 m depth. There are 1000 rays with uniformly distributed angles of depression between -10 and 10 degrees. 47

Figure 3.12 Shadow zone bounding rays from a 13 m source by the two SSPs in Figure 3.10. 48

Figure 3.13 Color scaled envelopes of a set of consecutive pings pre-filtered around 10 kHz for a section of the "solid line" track in Figure 1.2c. Time of the first arrival is normalized to 1 s. Sonobuoy depth is (a) 27 m (b) 122 m. 50

Figure 3.14 Envelopes of the 10 kHz signals from 6 km range with 13 m source depth: (a) First arrivals. (b) The later arrivals. 52

Figure 3.15 Some indicative beams for source depth of 83 m and the early afternoon SSP in Figure 3.10 from February 2001 in San Nicolas Basin. 53

Figure 4.1 Noise PSD at the reference hydrophone (3 m away from the source), measured at Tanner–Cortes Bank (Figure 1.2a, solid line). Conversion from voltage to pressure was done with the response in Figure 1.6. 59

Figure 4.2 Noise PSD at Tanner-Cortes Bank (Figure 1.2a, solid line); approximate range and hydrophone depth, respectively, are: (a) -3.5 km, 27 m; (b) -3.5 km, 61 m; (c) 200 m, 27 m; (d) 200 m, 61 m; (e) 3.5 km, 27 m; (f) 3.5 km, 61 m; negative range refers to the section before CPA. 60

Figure 4.3 Color scaled envelopes of a set of consecutive pings from the section of the "solid line" track in Figure 1.2a that crosses the CPA (range=200 m). Source depth: 40 m before CPA, 19 m past CPA. Carrier frequency and hydrophone depth, respectively, are: (a) 3 kHz, 27 m; (b) 3 kHz, 61 m; (c) 10 kHz, 27 m; (d) 10 kHz, 61 m; (e) 30 kHz, 27 m; (f) 30 kHz, 61 m. 64

Figure 4.4 Noise PSD at Tanner–Cortes Bank (Figure 1.2a, dashed line). The ship with the source transducer was moving away from the sonobuoys at a range of about r=3.5 km. Hydrophone depth: (a) 27 m (b) 61 m. 65

Figure 4.5 Noise PSD at China Point (Figure 1.2b, solid line); approximate range and hydrophone depth, respectively, are: (a) -3.5 km, 27 m; (b) -3.5 km, 61 m; (c) 300 m, 27 m; (d) 300 m, 61 m; (e) 3.5 km, 27 m; (f) 3.5 km, 61 m; negative range refers to the section before CPA. 66

Figure 4.6 Noise PSD at the reference hydrophone (3 m away from the source), measured in San Nicolas Basin (Figure 1.2c, solid line). Conversion from voltage to pressure was done with the response from Figure 1.6. 68

Figure 4.7 Noise PSD in San Nicolas Basin (Figure 1.2c solid line); approximate range and hydrophone depth, respectively, are: (a) 300 m, 27 m; (b) 300 m, 122 m; (e) 2 km, 27 m; (f) 2 km, 122 m. 69

Figure 5.1 Pressure envelopes (units of Pa) of the 10 kHz pulses, including clutter, from 6 consecutive pings from measurements made at the Tanner-Cortes Bank site (range ≅ 2 km). Depths of the source and the receiving hydrophones were respectively about 40 m, 27 m, and 61 m. The arrows point to the first arrivals of the signals at the two different receiver depths. 73

Figure 5.2 Illustration of Equation 5.1. 74

Figure 5.3 Envelopes of the signals and background noise at the transmitted frequencies. The snapshots correspond to the CPA point of "solid line" track in Figure 1.2a (range ≈ 200 m); hydrophone depth 27 m. Estimated first arrival time window: 90 ms – 100 ms. 75

Figure 5.4 Envelopes of the correlation functions for the snapshots from Figure 5.3. The vertical scales are not unified for display purposes. 76

Figure 5.5 Phase snapshots of the signals corresponding to the envelopes in Figure 5.3. 77

Figure 5.6 Envelope of a received signal with a strong multipath component. The direct-path arrival starts at 0.1 s and the taller peak starting at 0.13 s is due to multipath. The dashed line is the envelope of the signal detected by matched filtering. 78

Figure 5.7 Sum of 16 rectified correlation functions received for one transmission sequence. The arrow points to the detected direct path arrival(s). 81

Figure 5.8 Summation of the rectified correlation functions: a) the template b) a real signal sample from Figure 5.7. 82

Figure 5.9 Projected pulse envelopes at the 16 frequencies (range ≈ 1 km, before CPA), measured at Cortes-Tanner Bank (Figure 1.2a solid line), for hydrophone depth of 61 m. First arrival time window: 90 ms – 100 ms; the vertical scales are not unified for display purposes. 84

Figure 5.10 Phases that correspond to the envelope snapshots in Figure 5.9. First arrival time window: 90 ms – 100 ms; Recorded at: (a) Reference hydrophone. (b) Sonobuoy hydrophone. 85

Figure 5.11 An example of a successful signal detection completed after two iterations. The line with symbols represents the times. The parallel straight lines delimit the 5ms confidence region of the least square fit. 88

Figure 5.12 Spectrogram of the time series received at one hydrophone for one transmission sequence (range ≅ 2 km). Circles identify direct-path arrivals, and trailing signals represent multipath arrivals. 89

Figure 5.13 Pulses transmitted at the 16 frequencies (range ≈ 1 km), measured at the San Nicolas Basin site (Figure 1.2c solid line), for hydrophone depth of 122 m; source depth 13 m; first arrival time window: 90 ms – 100 ms. (a) Envelopes; the vertical scales are not unified for display purposes (b) Phases. 90

Figure 6.1 TL estimation for the Tanner-Cortes Bank based on the semi empirical equations (Equation 6.7 to Equation 6.10); data from Marsh and Shulkin [3]. The free-field curve includes spherical spreading plus absorption in water; data from François and Garrison [31] [32]. 103

Figure 6.2 TL vs. range at the 16 frequencies; location from Figure 1.2a (along the solid line), for hydrophone depth of 27 m. Source depth was 40 m and 19 m for negative and positive ranges, respectively; *exp* = experimental; *sph* = spherical spreading plus absorption in water; *cyl* = cylindrical spreading plus absorption in water; absorption data from François and Garrison [31-32]. 104

Figure 6.3 Blow-up of the TL vs. range at 15 kHz plot in Figure 6.3; hydrophone depth of 27 m; source depth was 40 m and 19 m for negative and positive ranges, respectively; *exp* = experimental; *sph* = spherical spreading plus absorption in water; *cyl* = cylindrical spreading plus absorption in water; absorption data from François and Garrison [31-32]. 105

Figure 6.4 TL vs. range at the 16 frequencies; location from Figure 1.2a (along the solid line); hydrophone depth 61 m. Source depth was 40 m and 19 m for negative and positive ranges, respectively; *exp* = experimental; *sph* = spherical spreading plus absorption in water; *cyl* = cylindrical spreading plus absorption in water; absorption data from François and Garrison [31-32]. 106

Figure 6.5 Difference in the measured TL at 61 m and 27 m at the 16 frequencies; location from Figure 1.2a (along the solid line). The differences in TL higher than 10 dB are not presented. Source depth was 40 m and 19 m for negative and positive ranges, respectively. 108

Figure 6.6 Contours of TL vs. range and frequency, measured at Cortes-Tanner Bank (Figure 1.2a along the solid line), for hydrophone depths of 27 m. The white regions correspond to SNR < 6 dB. Source depth was 40 m and 19 m for negative and positive ranges, respectively. 110

Figure 6.7 Contours of TL vs. range and frequency, measured at Cortes-Tanner Bank (Figure 1.2a along the solid line), for hydrophone depths of 61 m. The white regions correspond to SNR < 6 dB. Source depth was 40 m and 19 m for negative and positive ranges, respectively. 111

Figure 6.8 TL vs. range at the 16 frequencies; location from Figure 1.2a (along the dashed line); hydrophone depth 27 m. Source depth was 40 m; *exp* = experimental; *sph* = spherical spreading plus absorption in water; *cyl* = cylindrical spreading plus absorption in water; absorption data from François and Garrison [31-32]. 112

Figure 6.9 TL vs. range at the 16 frequencies; location from Figure 1.2a (along the dashed line); hydrophone depth 61 m. Source depth was 40 m; *exp* = experimental; *sph* = spherical spreading plus absorption in water; *cyl* = cylindrical spreading plus absorption in water; absorption data from François and Garrison [31-32]. 113

Figure 6.10 Difference in the measured TL at 61 m and 27 m at the 16 frequencies; location from Figure 1.2a (along the dashed line). Differences higher than 10 dB are not presented. 114

Figure 6.11 Contours of TL vs. range and frequency, location from Figure 1.2a (along the dashed line), for hydrophone depths of 27 m. 115

Figure 6.12 Contours of TL vs. range and frequency, measured at Cortes-Tanner Bank (Figure 1.2a along the dashed line), for hydrophone depths of 61 m. 116

Figure 6.13 TL vs. range at the 16 frequencies; location from Figure 1.2b (along the solid line); hydrophone depth 27 m. Source depth was about 60 m and 35 m for (-) and (+) ranges, respectively; *exp* = experimental; *sph* = spherical spreading plus absorption in water; *cyl* = cylindrical spreading plus absorption in water; absorption data from François and Garrison [31-32]. 120

Figure 6.14 TL vs. range at the 16 frequencies; location from Figure 1.2b (along the solid line); hydrophone depth 61 m. Source depth was about 60 m and 35 m for (-) and (+) ranges, respectively; *exp* = experimental; *sph* = spherical spreading plus absorption in water; *cyl* = cylindrical spreading plus absorption in water; absorption data from François and Garrison [31-32]. 121

Figure 6.15 Difference in the measured TL at 61 m and 27 m at the 16 frequencies; location from Figure 1.2b (along the solid line). The values higher than 10 dB are not presented. Source depth was about 60 m and 35 m for (-) and (+) ranges, respectively. 122

Figure 6.16 Contours of TL vs. range and frequency, location from Figure 1.2b (along the solid line); hydrophone depth 27 m. Source depth was about 60 m and 35 m for (-) and (+) ranges, respectively. 123

Figure 6.17 Contours of TL vs. range and frequency, location from Figure 1.2b (along the solid line); hydrophone depth 61 m. Source depth was about 60 m and 35 m for (-) and (+) ranges, respectively. 124

Figure 6.18 TL vs. range at the 16 frequencies; location from Figure 1.2b (along the dashed line); hydrophone depth 27 m. Source depth ≈ 18 m; *exp* = experimental; *sph* = spherical spreading plus absorption in water; *cyl* = cylindrical spreading plus absorption in water; absorption data from François and Garrison [31-32]. 125

Figure 6.19 TL vs. range at the 16 frequencies; location from Figure 1.2b (along the dashed line); hydrophone depth 61 m. Source depth ≈ 18 m; *exp* = experimental; *sph* = spherical spreading plus absorption in water; *cyl* = cylindrical spreading plus absorption in water; absorption data from François and Garrison [31-32]. 126

Figure 6.20 Difference in the measured TL at 61 m and 27 m at the 16 frequencies; location from Figure 1.2b (along the dashed line). The values higher than 10 dB are not presented. Source depth ≈ 18 m. 127

Figure 6.21 Contours of TL vs. range and frequency, location from Figure 1.2b (along the dashed line); hydrophone depth 27 m. Source depth ≈ 18 m. 128

Figure 6.22 Contours of TL vs. range and frequency, location from Figure 1.2b (along the dashed line); hydrophone depth 61 m. Source depth ≈ 18 m. 129

Figure 6.23 TL vs. range at the 16 frequencies; location from Figure 1.2c (along the solid line); hydrophone depth 27 m. Source ≈ 13 m; *exp* = experimental; *sph* = spherical spreading plus absorption in water; *cyl* = cylindrical spreading plus absorption in water; absorption data from François and Garrison [31-32]. 130

Figure 6.24 TL vs. range at the 16 frequencies; location from Figure 1.2c (along the solid line); hydrophone depth 122 m. Source ≈ 13 m; *exp* = experimental; *sph* = spherical spreading plus absorption in water; *cyl* = cylindrical spreading plus absorption in water; absorption data from François and Garrison [31-32]. 131

Figure 6.25 Difference in the measured TL at 122 m and 27 m at the 16 frequencies; location from Figure 1.2c (along the solid line). Source ≈ 13 m. 132

Figure 6.26 Contours of TL vs. range and frequency, location from Figure 1.2c (along the solid line); hydrophone depth 27 m. Source ≈ 13 m. 133

Figure 6.27 Contours of TL vs. range and frequency, location from Figure 1.2c (along the solid line); hydrophone depth 122 m. Source ≈ 13 m. 134

Figure 6.28 TL vs. range at the 16 frequencies; location from Figure 1.2c (along the dashed line); hydrophone depth 27 m. Source depth was about 13 m and 83 m before and after 1 km, respectively; *exp* = experimental; *sph* = spherical spreading plus absorption in water; *cyl* = cylindrical spreading plus absorption in water; absorption data from François and Garrison [31-32]. 135

Figure 6.29 TL vs. range at the 16 frequencies; location from Figure 1.2c (along the dashed line); hydrophone depth 122 m. Source depth was about 13 m and 83 m before and after 1 km, respectively; *exp* = experimental; *sph* = spherical spreading plus absorption in water; *cyl* = cylindrical spreading plus absorption in water; absorption data from François and Garrison [31-32]. 136

Figure 6.30 Difference in the measured TL at 122 m and 27 m at the 16 frequencies; location from Figure 1.2c (along the dashed line). Source depth was about 13 m and 83 m before and after 1 km, respectively. 137

Figure 6.31 Contours of TL vs. range and frequency, location from Figure 1.2c (along the dashed line); hydrophone depth 27 m. Source depth was about 13 m and 83 m before and after 1 km, respectively. 138

Figure 6.32 Contours of TL vs. range and frequency, location from Figure 1.2c (along the dashed line); hydrophone depth 122 m. Source depth was about 13 m and 83 m before and after 1 km, respectively. 139

Figure A.1 Comparison of contribution of the generic components of theoretical TL model, spherical spreading, cylindrical spreading and absorption [31-32] in frequency. Assumed temperature for the absorption calculation is 14 °C. 148

ABSTRACT

UNDERWATER COMMUNICATION CHANNEL
CHARACTERIZATION IN THE SOUTHERN
CALIFORNIA OFF-SHORE RANGE

by

Arsen Zoksimovski

University of New Hampshire, December 2004

A high frequency underwater acoustic communication experiment was conducted at two shallow water locations and one deep water location in the vicinity of San Clemente Island, CA, in February 2001. In order to measure underwater acoustic transmission loss over direct-path lengths ranging from a few hundred meters to ten kilometers, a sequence of 16 gated pure tones (3-30 kHz) was transmitted every 10 s from a towed source and received at two vertically displaced hydrophones. A set of simulations was performed with ray tracing software, showing that the sound speed profiles set range limits to direct-path propagation at the shallow and deep water sites. On the other hand, a number of local-minimum sub-layers in the sound speed profiles, particularly in shallow water, lead to extended direct-path ranges depending on the source/receiver depth. Signal recognition in multipath and noisy environment was obtained, in shallow water (<200 m), by searching for the direct-path arrival near the global maximum of the sum of the rectified correlation functions of the received sequences, and, in deep water (>1500 m), via iterative least square time constraints on the

arrival times across all frequencies in a sequence, based on the known time intervals between transmitted tones. Experimentally mapped direct-path zones, recognized as the ranges where the experimental transmission loss curves departed from the theoretical model of spherical spreading plus absorption, were between 3 km and 4 km in shallow water and between 4 km and 5 km in deep water. Some experimental transmission loss curves exhibited extended direct-path distances. Beyond these direct-path zones, there was a gradual transition to cylindrical spreading plus absorption, due to ray windowing and surface ducting in deep water, and boundary interaction in shallow water. In several cases, transmission loss did not show substantial increase with increase in frequency inside a frequency band of a few kHz at ranges as long as 2 km to 3 km.

INTRODUCTION

Motivation

In many sub sea applications there is a need to transfer signals from sub sea sensors and instruments to a distant submerged vehicle or a surface location. In many cases it is not practical to send data through an umbilical so an acoustic solution is required. To that end, acoustic modems are commercially available for a variety of depths and bit rates [1]. In order to achieve higher bit rates in digital transmission, higher frequencies are required. Furthermore, higher frequencies are required for downsizing of acoustic modems because the higher the operating frequency is the smaller the transducers, as well as the spacing in an array of transducers, need to be.

Regarding transmission loss (TL), two important propagation factors are significant for the sonar system design: spreading and absorption. Spreading is modeled either with a free-space spherical geometry leading to $1/r^2$ ($20\log_{10}R$ [dB, Re 1 m]) dependence for the signal intensity, or with a horizontally stratified (cylindrical) geometry with a $1/r$ ($10\log_{10}R$ [dB, Re 1 m]) dependence. Absorption losses vary with local temperature and pressure (depth), depend exponentially on range, and increase in proportion to the square of the acoustic frequency [2]. Other factors of acoustic field attenuation are refraction, reflections from the seafloor and the sea surface, various kinds of sound ducts existing in the sea, internal waves, and the multipath effects causing fluctuations in sound reception. All these issues have been, and still are, the subject of an intense amount of research. Although applications to military sonar have stimulated most

of the research, other areas such as oceanography, petroleum exploration, navigation, and coastal zone investigations have contributed significantly.

Objective

The goal of this thesis is two-fold: 1) use the result of a simple experiment to measure TL in the 3 kHz – 30 kHz frequency band for the given source/receiver depth and weigh it with respect to the mixed layer, an isothermal layer just below the sea surface with a nearly uniform sound speed vs. depth profile; in other words, predict how reliable and how far from the source, under the given circumstances (the equipment, the source/receiver depth, the choice of frequencies, expected sound speed profile etc), meaningful communication, with respect to the applied detection threshold (DT), could be achieved; 2) provide estimation of the direct-path horizontal range zone in the study region, for the given source/receiver depth; "direct-path" wave is a wave that was not reflected from either the sea-surface or the seafloor. The importance of direct-path arrival detection in both coherent and incoherent communication is its robustness because it does not suffer additional loss and phase distortion from boundary interaction.

Previous Work

According to Urick [2], the semi-empirical expressions published by Marsh and Shulkin [3], accompanied with the sea state and bottom type influence analysis, are particularly useful for shallow water transmission. These are based on some 100,000 measurements in shallow water in the frequency range 0.1 to 10 kHz. They suggest that, at ranges shorter than the skip distance, the spherical model is more appropriate whereas

at ranges longer than eight times the skip distance, the cylindrical model applies. The skip distance varies with the water depth and the mixed layer depth. For intermediate ranges, where interaction with the seabed is somewhat important, that experiment and theory suggest that a $1/r^{3/2}$ ($15\log_{10}R$ [dB]) dependence is appropriate. It is also suggested by these equations that TL in shallow water does not depend on the source/receiver depth.

The same authors [4] derived a series of formulas, later graphically represented by Urick [2], that gave the TL at 2 kHz and 8 kHz for various combinations of source and receiver depths, with respect to the mixed layer. It showed that TL is lower when the source and the receiver are both in the mixed layer than otherwise, although a setup with a source below and a receiver inside the mixed layer was not considered. It also showed that for fix source/receiver depths the gain was even greater with a deeper mixed layer.

It is common for both aforementioned TL models that the sound speed profile (SSP) is not considered beyond the mixed layer depth. Ferla and Porter [5] analyzed an optimal receiver depth problem with respect to TL at two frequencies below 1 kHz, based on a normal-mode model for summer and winter SSPs, respectively with and without the mixed layer, from deep water in the Mediterranean sea. A conclusion that emerged from their study was that, if the source depth is known then the receiver should be deployed at that depth or at a conjugate depth, where the sound speed matches that at the source. Absence of the mixed layer somewhat changed the energy distribution vs. depth and range, but the optimal depth criterion remained the same. In their study they made numerous assumptions of which the most important are: range/depth independent noise background, log-normal probability of detection, and range-independent environment.

Results obtained in the 50 Hz - 3.2 kHz frequency band by Jensen and Kuperman [6-7] have shown that in waters shallower than 100 m, the optimum underwater acoustic propagation frequency is around a few hundred Hz. It is the result of competing propagation and attenuation mechanisms at high and low frequencies. A survey conducted by Akal [8] confirmed that in the shallow polar waters.

Present Work

Due to environmental variability with location, TL model testing and improvement often requires measurements in a particular area. To that end, an experiment was conducted in February 2001 by Scripps Institution of Oceanography (SIO) researchers in the Southern California Bight. It was a bi-static setup based on the periodic transmission of sequences of sixteen 10 ms long CW pulses at various frequencies in the 3 kHz – 30 kHz frequency band, with a 10 s pause between two consecutive sequences, from an omni-directional source transducer towed by a ship that was passing by two moored, vertically displaced, omni-directional hydrophones that served as receivers. One of the receivers was intended to be in the mixed layer and the other one below the mixed layer, while the source would be kept in or below the mixed layer.

Chapter 1, *Description of the Experiment*, spells out the geometry of the experiment and the measurement framework, and provides basic specifications of the equipment used. Some basic signal processing tools that were used during the project and issues related to the signal properties are introduced in Chapter 2, *Post Event Analysis*. The computational part of the data processing was implemented partly in C++ and partly

in MATLAB. MATLAB Signal Processing Toolbox [9] was especially useful for the purposes of filtering and power spectral density estimations, while its graphical user interface (GUI) was used for various illustrations.

Understanding of the ocean environment and the physics of signal propagation is required to interpret what the sonar system is indicating to an observer. A large number of computer models, based upon mode theory, ray theory, or some combinations of both, are available (e.g. [10] [11]) for acoustic signal propagation modeling. Chapter 3, *Sonar Signal Propagation*, lays out an evaluation of the signal propagation in the study area based on ray theory and sets a foundation for the remaining chapters. The SSPs used in simulations were calculated from conductivity/temperature/depth (CTD) measurements conducted during the experiment.

Chapter 4, *Background Noise Analysis*, is devoted to the background noise related issues in the post event analysis, mainly regarding noise spectrum and distinguishing among possible sources of noise based on the measurements in the pause-time slots. The noise level (NL) radiated from the ship towing the source transducer was higher at short ranges, especially when the ship's propellers were facing the hydrophones while the ship was moving away from them. Therefore the noise could not be assumed to be range/depth independent.

Before experimental TL is evaluated in post event analysis, the transmitted pulses have to be properly detected, located and extracted from background noise. When the source signal is known, in the ideal case of a white-noise background, the detection is best achieved with a matched filter [12]. This filter detects a pulse at the correlation maximum of the time-reversed replica of the transmitted pulse and the received signal.

Although there are some suggestions for improvement of the conventional matched filter performance by accounting for the environmental effect in the correlation function, such as ray-model-based matched filter processing [13], in this thesis a correlation function is generated in the conventional way because the environment was insufficiently known for building a model of required accuracy, the estimated Doppler shift was smaller than the frequency resolution achieved, and it was simpler and less computationally demanding for implementation. Chapter 5, *Pulse Extraction*, describes two methods that were devised for resolving direct path arrival under severe multipath conditions in order to improve the pulse detection process in the post event analysis. Both methods take advantage of the frequency diversity obtained from the design of the experiment. One method is based on the summation of the rectified correlation functions at each frequency used, whereas the other method uses least square time constraint to gain accurate pulse localization.

After the signal and NL measurements were completed, experimental TL curves were calculated and compared to the most generic theoretical models that include spreading plus absorption. Chapter 6, *Transmission Loss Calculations*, summarizes the most important findings regarding TL measurements in this thesis. The findings are compared to the estimations based on simulations in Chapter 3, and contrasted with Marsh and Shulkin's model [3], particularly for the skip distances in shallow water. The depths at which the measurements were conducted are weighed with respect to TL by direct comparison. That serves as a basis for contrasting with another Marsh and Shulkin's model [4], which was graphically represented by Urick [2], having the source/receiver and mixed layer depth for parameters. Due to the nature of the

experiment, some theoretical assumptions made by Ferla and Porter [5] could not be met, and some other assumptions regarding technical limitations of the equipment and the nature of the experiment had to be made. Nonetheless, comparison of the experimental TL at the given depths serves as a simple test of the optimal depth rule. Another important aspect of the system/environment calibration is a depiction of the measured TL vs. range and frequency. The frequency band of interest is above 3 kHz, so the optimum frequency [6] is not expected in shallow water, but the significance of highly range/frequency dependent absorption in the TL mix with spreading is considered.

CHAPTER 1

DESCRIPTION OF THE EXPERIMENT

The experimental data were collected at three sites in the Southern California Offshore Range, West of San Clemente Island, in February 2001. Two sites were in water depths ranging from 100 m to 300 m, one was between Cortes and Tanner Bank (32°41'N/119°11.07'W), and the other was South of San Clemente Island's China Point (32°45.17'N/118°25'W). The third site was in deep water (1600 m) in San Nicolas Basin (32°55'N/118°54'W). The environmental part of the experiment included CTD measurements, as well as shipboard and moored acoustic Doppler current profiles.

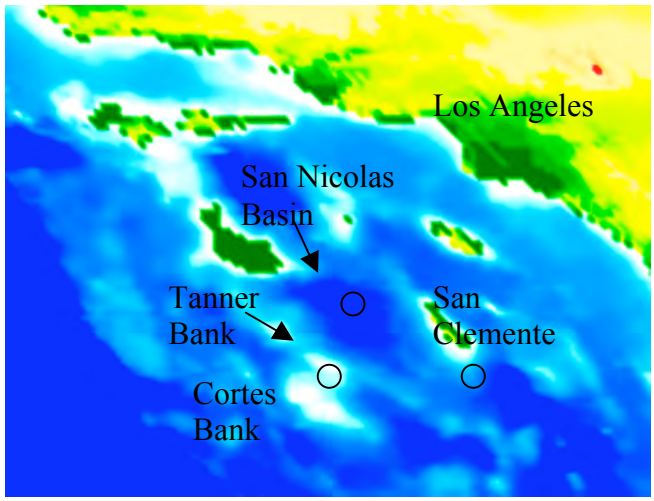

Figure 1.1 Region where the experiments were carried out. The rings show approximate positions of the three surveyed sites.

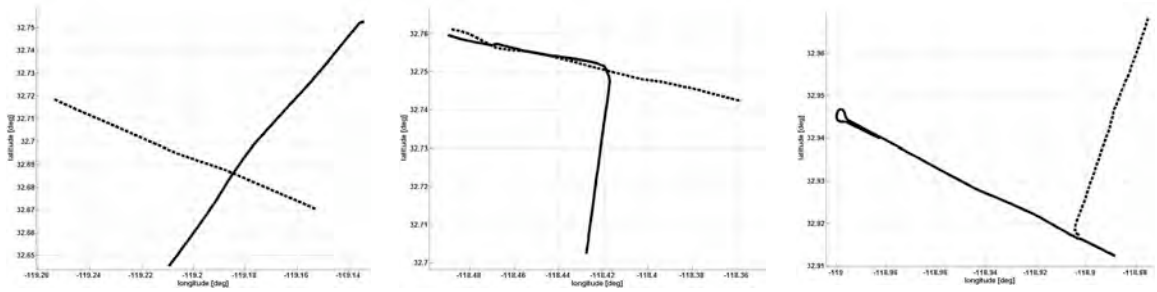

(a) (b) (c)

Figure 1.2 GPS coordinates of the ship along the data collection routes. Sign "-" means West in longitude. (a) Cortes-Tanner Bank (b) South of San Clemente Island's China Point (c) San Nicolas Basin.

The geometry of the experiments is shown in Figure 1.3. For the TL measurements, the acoustic signals were transmitted from an omni-directional transducer (ITC-1007) [14] towed by a ship, and were recorded at two identical AN/SSQ-57B sonobuoy hydrophones [15] deployed on a mooring line at 90 ft (27.4 m) and 200 ft (61 m) at the shallow water sites, and on a floating line at 90 ft and 400 ft (122 m) depths at the deep water site. Since this sonobuoy model is designed for 90 ft and 400 ft depth only, it had to be wrapped to reduce its depth from 400 ft to 200 ft. The intent was to place one hydrophone in, and one below the mixed layer. Likewise, the source was towed in and below the mixed layer.

As listed in Table 1.1, one experimental track was set in morning hours, while the other tracks took place during afternoon hours. The mixed layer depth is usually minimal in the afternoon due to ongoing exposure to sun heating the upper portion, thereby decreasing the gradient [16]. This heating effect eventually culminates in a negative gradient that leads to a downward refraction and the loss of sound from the layer. During night, surface cooling and wave mixing allow the isothermal layer to be reestablished so

it is typically present early in the morning. The surveys included sound speed measurements by CTD and expendable bathythermograph (XBT) instruments, as well as measurements of the currents, using an Acoustic Doppler Current Profiler (ADCP) device, and bathymetry of the shallow water sites. The CTD measurements were conducted, in the proximity of the sonobuoy location, around four different times of day: midnight, 6 AM, noon, 6 PM. The SSPs varied accordingly (See Chapter 3). The XBT measurements were conducted, at different times of day, at various locations along the acoustic data collection tracks (Figure 1.2).

Horizontal range between source and receiver can be calculated from GPS coordinates (Figure 1.2). The position of the moored sonobuoy system is assumed to be the last reading, right before it was unhooked from the ship, on the handheld GPS receiver it was equipped with. This assumption is more valid for the shallow water experiments (Figure 1.2a and b) because the sonobuoys system was moored, unlike the deep water site (Figure 1.2c) where it was floating. Therefore somewhat higher range uncertainty is expected for the deep water experiment.

Source depth schedule for each site is summarized in Table 1.2. The positions of the sonobuoys were in the vicinity of the intersections of the tracks at each site (Figure 1.2); therefore, in shallow water the ship towing the source transducer was passing by the sonobuoys with a closest point of approach (CPA) of a few hundred meters. At the deep water site, the ship towing the transducer was moving away from the sonobuoys; therefore the shortest range corresponded to the starting position of the ship.

Site/Track		Time window (local time) / Date	
South of China Point	Solid line	14:30 – 16:00	Feb 19th 2001
	Dashed line	16:30 – 18:00	
Tanner – Cortes Bank	Solid line	10:30 – 12:00	Feb 20th 2001
	Dashed line	14:30 – 15:30	
San Nicolas Basin	Solid line	16:00 – 17:00	Feb 22nd
	Dashed line	15:00 – 16:00	Feb 23rd

Table 1.1 TL measurement schedule in February 2001. "Solid line" and "dashed line" refer to the sketches in Figure 1.2.

Site/Track		Local time	Depth (m)	Direction
South of China Point	Solid line	< 15:05 (CPA)	60	SW-NE
		> 15:05	35	SE-NW
	Dashed line	All	18	NW-SE
Tanner – Cortes Bank	Solid line	< 11:05 (CPA)	40	SW-NE
		> 11:05	19	
	Dashed line	All	40	NW-SE
San Nicolas Basin	Solid line	All	13	SE-NW
	Dashed line	< 15:04 (r=1 km)	13	SW-NE
		> 15:04	83	

Table 1.2 Source depth and ship course schedules during the data collection; "solid line" and "dashed line" refer to the sketches in Figure 1.2; symbols "<" and ">" stand for "before" and "after", respectively; N, S, E, and W refer to North, South, East and West, respectively.

In the Southern California Bight, the depth of the mixed layer decreases from about 50 m in January, to around 20 m in April [17]. During the experiments, the base of the mixed layer was typically found between 10 m and 40 m below the sea surface. However, the mixed layer was not always strongly defined and the depth of its base varied along the transmission path.

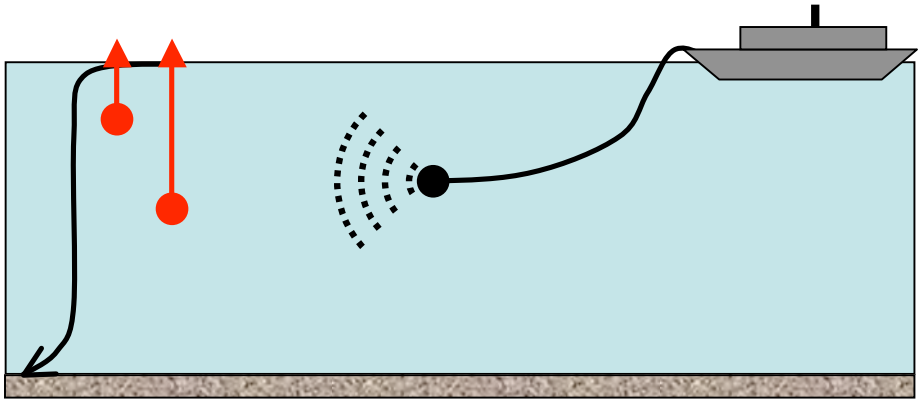

Figure 1.3 Geometry of the experiment with moored sonobuoys.

A transmission sequence consisted of 16 continuous wave (CW) pulses at discrete frequencies ranging from 3 kHz to 12 kHz in 1 kHz steps, and from 12 kHz to 30 kHz in 3 kHz steps. Each tone lasted 10 ms, with a 90 ms gap between pulses. The complete sequence lasted 1.6 s, followed by a 10 s quiescent period before the next transmission sequence, yielding a repetition period of 11.6 s for single frequency tones.

The data acquisition line is shown in Figure 1.4. After being transferred from the sonobuoys to the data acquisition computer on the ship through a radio link, acoustic signals and background noise were digitized at sampling rate of 100 kHz to 16 bit integer sequences. The dynamic range of the A / D converter was +/-20 V, setting digital resolution to $\Delta V = 40\ V / 2^{16} \approx 610.35\ \mu V$ for a quantization step.

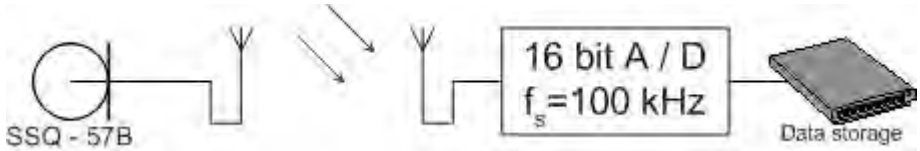

Figure 1.4 Data acquisition frame-up.

The sonobuoys used in the experiment are a part of the NAVY Consolidated Sonobuoys program [18]: Directional Frequency Analysis and Recording (DIFAR) Sonobuoy AN/SSQ-53B, Low Frequency Analysis and Recording (LOFAR) Sonobuoy AN/SSQ-57B, and Vertical Line Array Directional Frequency Analysis and Recording (VLAD) Sonobuoy AN/SSQ-77B. Particularly important for this thesis is the LOFAR AN/SSQ-57B, expendable, non-repairable, calibrated sonobuoy, which was used for the TL measurements. It consists of a broadband omni-directional hydrophone that descends through the bottom of the sonobuoy canister to a pre-selected depth (90 or 400 feet).

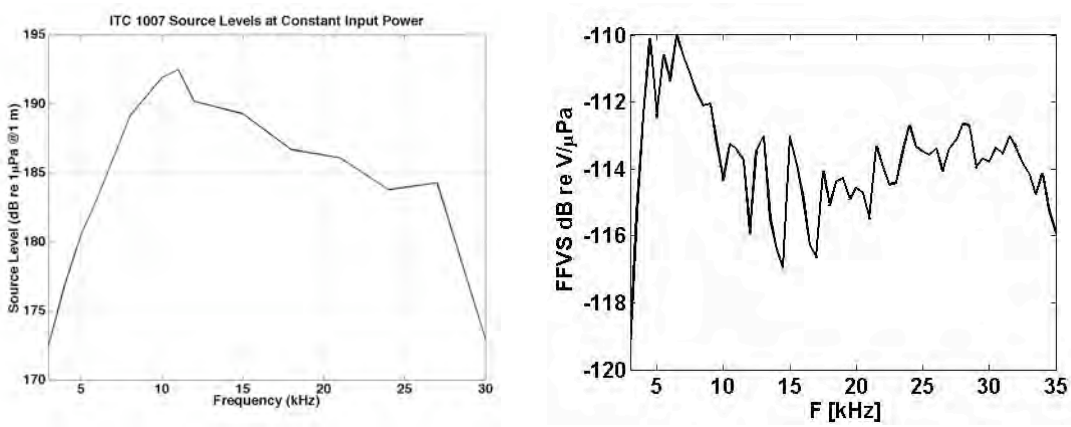

(a) (b)

Figure 1.5 (a) Source Level calibration of the ITC-1007 transducer and (b) Free Field Voltage Sensitivity calibration of the AN/SSQ-57B hydrophone. Measurements done at the US Navy's TRANSDEC facility in San Diego, CA.

As shown in Figure 1.5a, the transmitter source level (SL) ranged from 173 to 195dB re 1 μPa @ 1 m when driven at constant power. The transmitted signals were also recorded at an omni-directional reference hydrophone (ITC-1042) [14], attached on the towing line 3 m away from the source in order to monitor the SLs. Figure 1.5b shows the Free Field Voltage Sensitivity (FFVS) of the AN/SSQ-57B hydrophone. Equation 1.1 and Equation 1.2 show how FFVS is used for conversion of the stored signals from voltage to pressure.

$$P[\mu Pa] = \frac{V[V]}{ffvs[\frac{V}{\mu Pa}]}$$

Equation 1.1

$$FFVS[dB\,re\,{}^{V}\!/_{\mu Pa}] = 20\log_{10}\left(ffvs[\frac{V}{\mu Pa}]\right)$$

Equation 1.2

The ship towed the source at about 2.5 m/s on orthogonal traverses. To avoid saturation of the highly sensitive sonobuoy receivers (Figure 1.5b) when approaching those, SLs were reduced in 10 dB steps from the maximum values shown in Figure 1.5a.

The reference hydrophone sensitivity, i.e. the factor of conversion from pressure to voltage (Figure 1.6) is much lower than the sensitivity of the AN/SSQ-57B hydrophones. The calibration was conducted in a tank before the experiment.

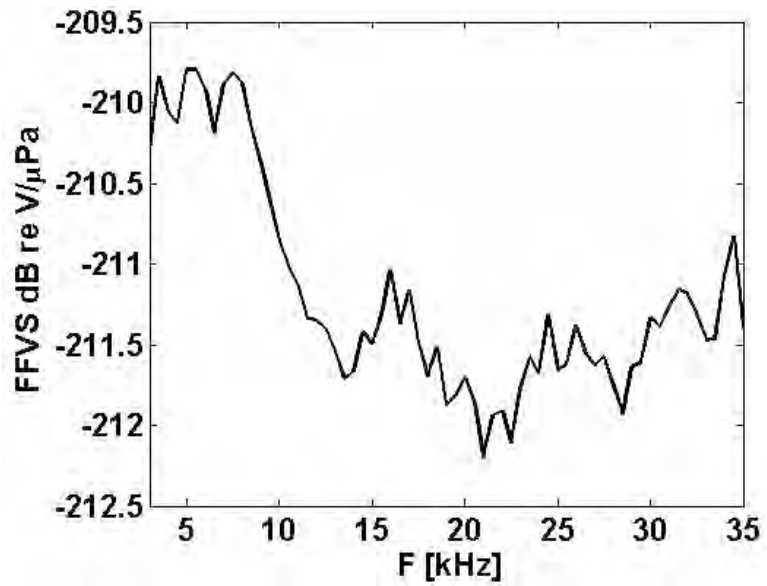

Figure 1.6 FFVS calibration of the ITC-1042 reference hydrophone. Measurements done at the US Navy's TRANSDEC facility in San Diego, CA.

A typical spectrogram of a received shallow water signal is shown in Figure 1.7. The received signals stand out in intensity at the corresponding frequencies. Significant acoustic intensity was detected at each transmitted frequency with longer duration than the transmission time of each pulse (10 ms). The extended time of each received signal is mostly the result of reflections from the seafloor and sea surface. Because of the limitations of the acoustic source used (Figure 1.5a), the transmitted power was stronger at the mid frequencies (8-12 kHz) than at the others, with a maximum at 11 kHz. Therefore, it takes longer for the acoustic field to settle back to the background NL after the transmission period for pulses near 11 kHz. Higher harmonics of some frequencies, e.g. 7, 8, 9, 10 kHz, are observable as well in Figure 1.7. Most notably, the strong third harmonics of these frequencies (21, 24, 27, and 30 kHz) fall in transmission bands, and are a possible cause of post analysis detection errors at those frequencies.

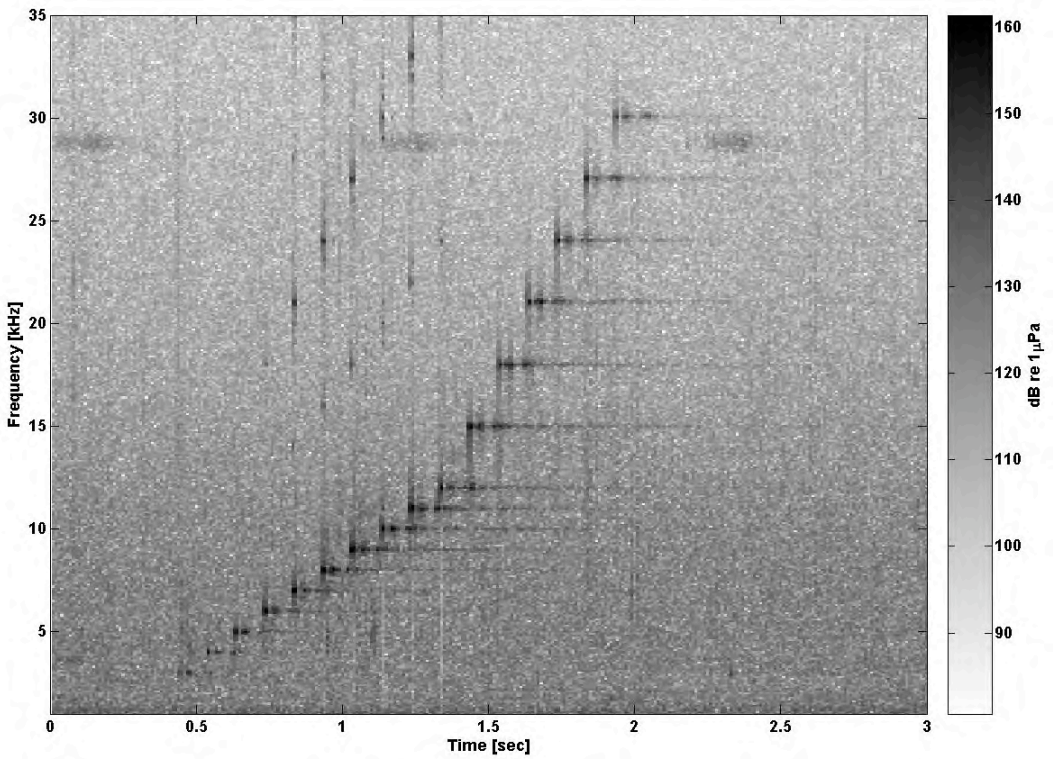

Figure 1.7 Spectrogram of the time series received in shallow water at a hydrophone for one transmission sequence (range ≅ 2 km). The trailing signals represent multipath arrivals.

According to Urick [2], the generation of harmonics of the fundamental frequency is caused by an effect of nonlinearity which is a dependence of propagation velocity on the pressure amplitude of the sound wave; high positive or negative pressures travel faster than low ones causing an initially sinusoidal waveform to progressively steepen as it propagates, eventually acquiring a saw-tooth-like waveform. The creation of harmonics occurs at the expense of the fundamental. This harmonic conversion process is greater at high amplitudes than at low ones so that, as the SL increases, the harmonic content increases also. A kind of saturation effect occurs, whereby an increase of SL does not give rise to a proportional increase in the level of the fundamental frequency. This saturation effect forms a limitation on the use of high acoustic powers in water,

manifesting itself as a negative feedback. If TL due to absorption is lower, signals travel at high amplitude, yielding loss of energy from the fundamental to higher harmonics.

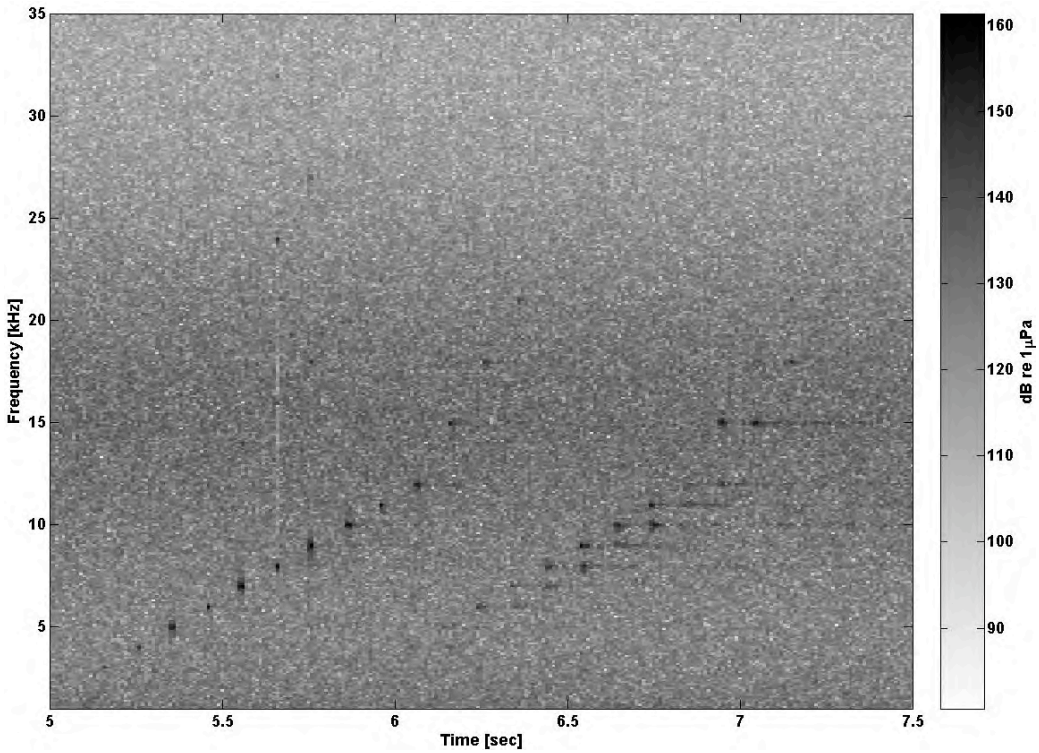

Figure 1.8 Spectrogram of the time series received in deep water at a hydrophone for one transmission sequence (range ≅ 2 km).

A typical spectrogram of a received deep water signal is shown in Figure 1.8. The multipath arrivals are clearly separated in time from the direct path arrival because of the distant boundaries. Higher harmonics of the carrier frequencies from the most efficient band of the projector transmit voltage response (TVR), illustrated in Figure 1.5a, appear in the picture with somewhat lower magnitude than in the aforementioned shallow water case.

CHAPTER 2

POST-EVENT ANALYSIS

Every telemetry system has to include some signal processing elements. If a broadband communication receiver is used, the received signals should be pre-filtered around the central frequencies of the transmit frequency bands. As the signal at the receiver has to be distinguished from noise, receivers have to have detection and estimation algorithm implemented. For demodulation purposes and offline analysis of the signals, it is often necessary to extract envelopes from the signals. Post event analysis of the signals from the experiment described in Chapter 1 is performed here through a set of three major sequential steps: (1) pre-filtering, (2) pulse extraction, (3) signal estimation, as shown in Figure 2.1.

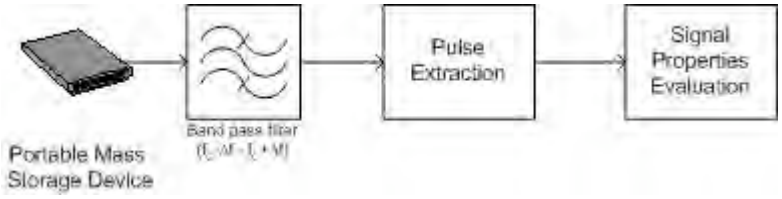

Figure 2.1 Post event analysis elements.

The purpose of pre-filtering is elimination of out-of-band noise before detection and estimation are applied. For example, if a continuous wave pulse were transmitted acoustically at frequency F, before matched filtering [19] should be applied for signal

detection, it would be very convenient to pre-filter the received sequence with a band-pass filter centered on the frequency F. A matched filter is an optimal detector for a known signal in White Gaussian Noise (WGN). Ambient noise in ocean acoustics is by no means white [2], as will be shown for the data presented in Chapter 4. As derived by Kay [20], for detection of signal buried in non-WGN, a matched filter could be generalized for optimal detection, if the covariance matrix of the noise were known. If that matrix is diagonal, whitening plus replica correlating is suggested for optimal performance [20]. For detection of known CW pulses, simple pre-filtering around the carrier frequency plays the role of the pre-whitener, assuming constant noise power spectral density (PSD) inside a narrow (< 100 Hz) frequency band.

The bandwidth of each band-pass filter should be at least as wide as the associated Doppler shift [2] Δf (Hz). In a section of water column without significant current, for a static receiver and a transmitter moving at speed v_s, sound speed c, and acoustic frequency f_m (Hz), the Doppler shift can be estimated as:

$$\Delta f = v_s f_m / c$$

Equation 2.1

For a ship speed v_s=2.5 m/s, sound speed c=1500 m/s, and acoustic frequency f_m (Hz), is given by Equation 2.1:

$$\Delta f = f_m / 600 \ \ (Hz)$$

Equation 2.2

By Equation 2.2, the maximum frequency shift relevant to our experiment was at 30 kHz, and was equal to 50 Hz. Depending on the geometry of an experiment, if the acoustic wave spends a significant amount of time inside a current or a jet, its speed, if known, should be included in v_s; however, this requires on site current measurements and accurate position of the ship track relative to the current. ADCP measurements conducted at Tanner-Cortes Bank showed the maximum current magnitude did not exceed 0.36 m/s. Its maximum effect would be when a ship track is matching the direction of the current. For sound speed c = 1500 m/s and the maximum relevant frequency of 30 kHz, it would change the frequency shift by:

$$\max(\Delta f_c) = \pm \frac{0.36\ \text{m/s}}{1500\ \text{m/s}} 30\,\text{kHz} = \pm\ 7.2\ \text{Hz}$$

Equation 2.3

After combining Equation 2.2 and Equation 2.3, total Doppler shift would be inside the following band:

$$\Delta f \leq 50\ \text{Hz} + 7.2\ \text{Hz} = 57.2\ \text{Hz}.$$

Equation 2.4

Another factor that sets a limit to the minimum bandwidth of a pre-filter is the effective (3 dB) bandwidth of a CW pulse. The frequency response of a CW pulse is a *sinc* function [22]. After approximating the frequency response of a CW pulse of length τ

($\text{sinc}^2(\tau W)$), with the first two terms of the corresponding Taylor series, the effective bandwidth W is approximately:

$$W \approx \frac{0.88}{\tau}$$

Equation 2.5

For τ=10 ms, the effective bandwidth is approximately W≈88 Hz, independent of the CW carrier frequency.

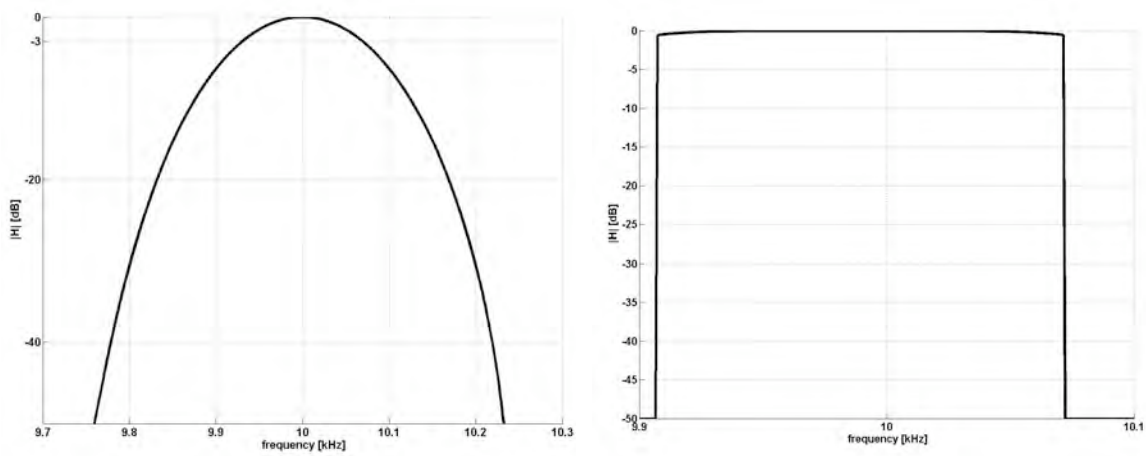

(a) (b)

Figure 2.2 Transfer function of a (a) FIR filter order 1000 and (b) IIR filter order 7.

Pre-filtering could be done using either finite impulse response (FIR) or infinite impulse response (IIR) filters. It is known [21] that an advantage of FIR filters is linear phase, whereas low order is on the side of IIR filters. However, for filtering very long

data sequences, the possibility of applying FFT based overlap-add convolution [22] makes FIR filtering very computationally efficient. In addition, IIR filters have stability issues. Therefore FIR should be more convenient for pre-filtering when phase information is important for signal analysis. For example, in Chapter 5 it is shown that phase information can be valuable for determining the nature of multipaths. IIR filter becomes a better choice if the filter order is a major concern, as is typically the case in hardware implementations. Although it was not used for this project because sufficient computing resources were available in the post event analysis, its brief parametric comparison to FIR filter is provided here for future reference.

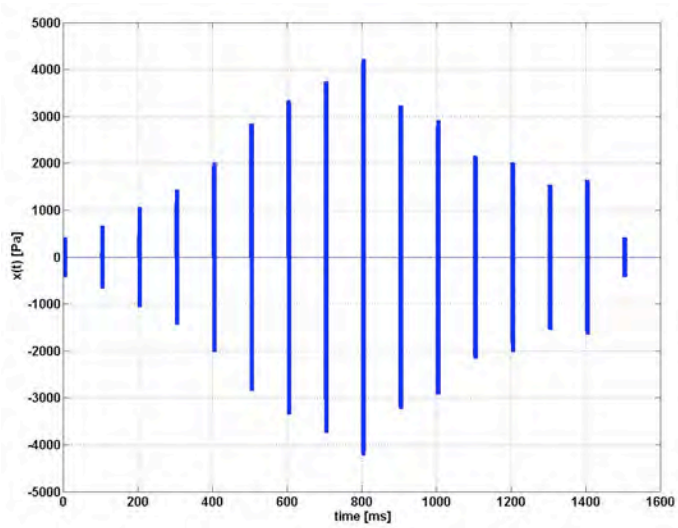

Figure 2.3 Transmit sequence of pulses. Frequency of each pulse is higher than frequency of its neighbor on the left, following the arithmetical progressions 3 kHz to 12 kHz and 15 kHz to 30 kHz with 1 kHz and 3 kHz steps, respectively.

Figure 2.2a shows a transfer function of a band-pass filter centered on 10 kHz, realized as an FIR filter of order 1000. Figure 2.2b shows a transfer function of a band-pass filter centered at 10 kHz, realized as a Chebyshev (Type II) IIR filter of order 7. The

IIR realization shows much steeper pass-band to stop-band roll-off, with much lower filter order. A slight asymmetry is noticeable in the transfer function of this filter, which is not the case with its FIR counterpart.

The steep roll-off factor of the IIR band-pass transfer function is achieved by placing its zeros and poles close to the unit circle. At the same time, zeros and poles have to be in certain positions with respect to each other. However, the accuracy of these positions is limited by the finite accuracy of discrete filter coefficients. Figure 2.2 therefore shows that the FIR filter is less sensitive to this problem because its transfer function is fully symmetric.

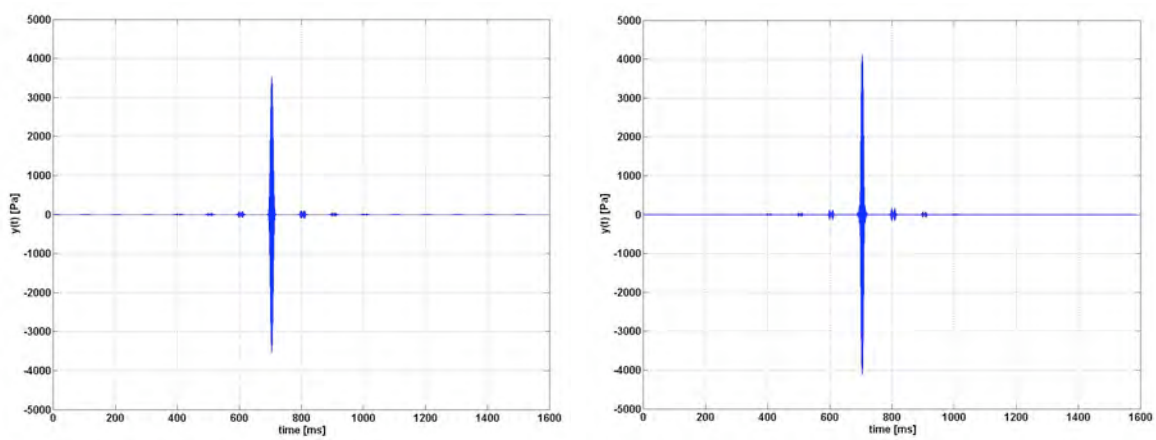

(a) (b)

Figure 2.4 Pre-filtered transmit sequence at 10 kHz with: (a) 1000-order FIR filter (b) 2×3+1-order IIR filter.

Another post-event analysis issue should be addressed in the time domain. Figure 2.3 illustrates a transmit sequence following the source function (Figure 1.5a) from the experiments. The vertical bars in the picture represent CW pulses at the transmit frequencies used in the experiments.

Figure 2.4a and b illustrate the time domain output of a Moving Average (MA) and Auto Regressive (AR) process on the input signal from Figure 2.3, respectively performed with the filters defined by the transfer functions from Figure 2.2a and b. Note (1) the ripples appear at the time intervals that correspond to non-10 kHz pulses and (2) the 10 kHz pulse magnitude in Figure 2.4b shows a slight gain in comparison to its original magnitude in Figure 2.3.

Since the frequency response of each CW pulse is a *sinc* function, there will be side-lobes spreading toward lower and higher frequencies from the center frequency. This is illustrated in Figure 2.5, together with the frequency response of the FIR filter from Figure 2.2a that was used for the result in Figure 2.4a. The overlap of the two spectra causes the ripples in Figure 2.4.

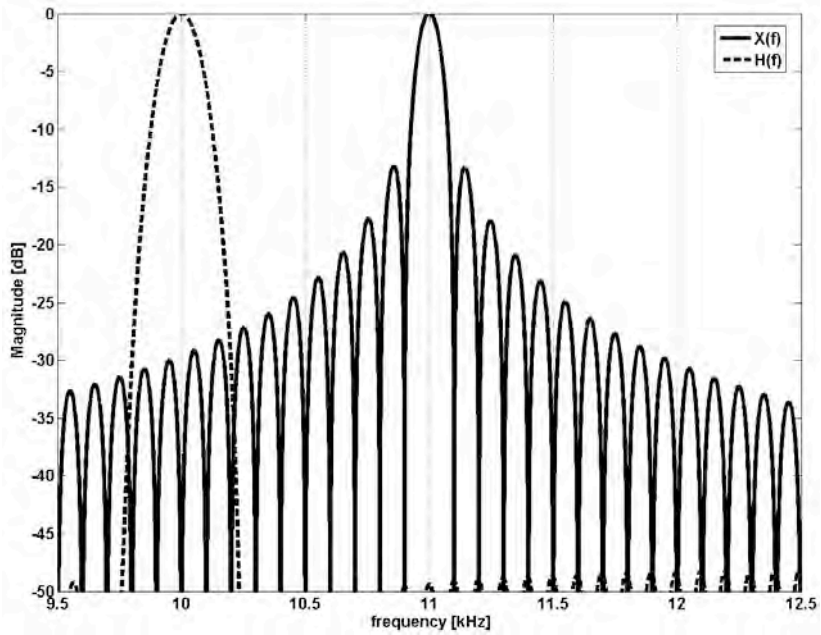

Figure 2.5 Frequency response of a 10 ms CW pulse at 11 kHz and an FIR filter centered at 10 kHz, both 1000 points long.

Figure 2.6 shows the ripples formed at the time interval of the 11 kHz pulse. The IIR filtered pulse shows slightly higher ripple magnitude in this realization. For an IIR and an FIR filtered pulse, the ripples come in pairs, one centered on the beginning, and the other one on the end of the pulse. The spectral overlap from Figure 2.5 indicates an attenuation of about 30 dB for the 11 kHz pulse that caused the ripples at 10 kHz. For the signal in Figure 2.4a, it gives 3740 Pa × $10^{-30/20}$ = 118 Pa, which is close to the ripple magnitude in Figure 2.6a.

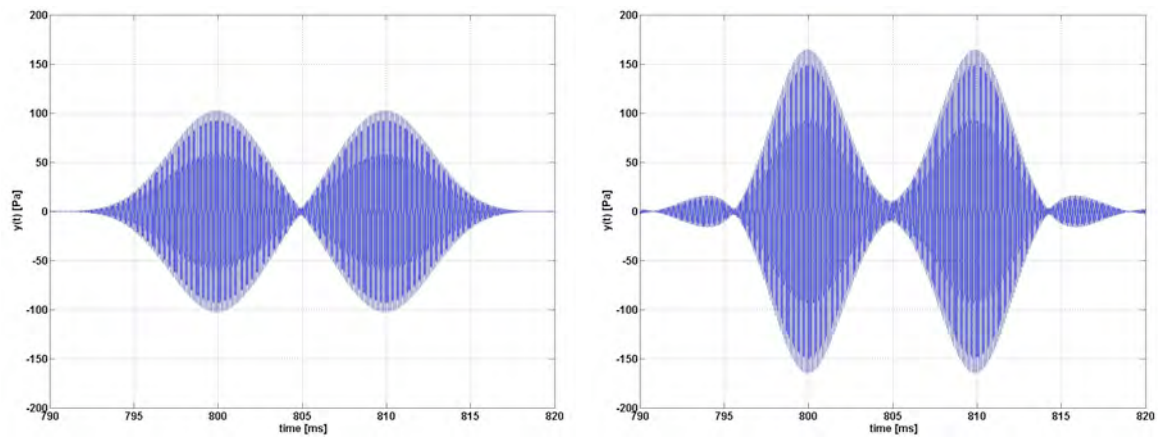

(a) (b)

Figure 2.6 The ripples at the time interval of the 11 kHz pulse for: (a) FIR pre-filter (b) IIR pre-filter.

Figure 2.7 illustrates the ripple effect through a time-frequency representation of the 30 kHz pulse. This spectrogram was calculated as a short time Fourier Transform with Kaiser Window and 0.1 ms per frame. Recalling the previous observation in Figure 2.6, it can be seen in Figure 2.7 that the frequency response rolls off from pass-band to stop-band slower at the beginning and at the end of the pulse, resulting in the ripples that are paired accordingly. It is important to be aware of this filtering artifact and avoid a

misleading observation. For example, when ambient noise is analyzed, the sections of the data where the ripples might occur should be avoided.

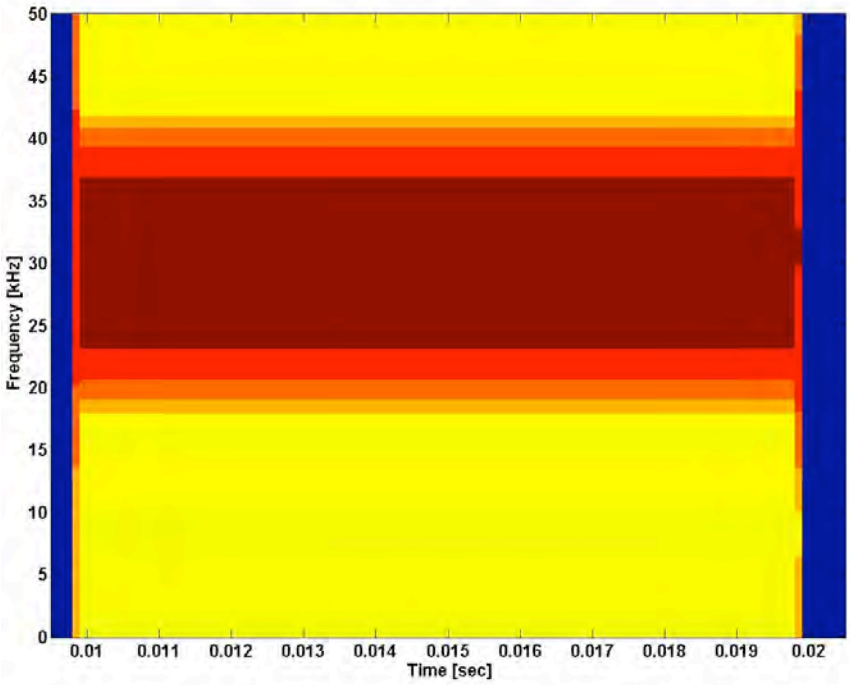

Figure 2.7 Spectrogram of a 30 kHz pulse. Time unit is 1 second and frequency unit is 1 Hz.

Matched filtering [19] is a commonly used linear method for detection of signals in noise. However, when noise (interference), like multipath, is highly correlated to the signal, linear filters are ineffective. In a real time application, adaptive equalization is usually performed [19] to compensate for Inter-Symbol Interference (ISI) caused by multipath propagation. Since the focus of this project is post-processing the data from the AN/SSQ-57B sonobuoy, signal detection is simpler because the signals were recorded on a uniform time schedule, providing a certain amount of predictability in the pulse's position inside a predetermined time window. Nevertheless, when the signal source is

moving, range changes from ping to ping, producing variable times of arrival of the transmitted pulses. In addition, system malfunction is always a possibility, yielding no signal when it was expected. Therefore specific signal detection algorithms should be employed for each ping, as will be discussed in more details in Chapter 5.

CHAPTER 3

SONAR SIGNAL PROPAGATION

Two common approaches in sound propagation modeling, in underwater acoustics, are mode and ray theory. While these theories are described thoroughly by Kinsler et al [16], the most important differences between them help decide which to use for simulations. Mode theory is convenient when the wavelength of a transmitted acoustic signal is at least comparable to the depth of the water column or its sub-layer if ducted propagation is in question. Wavelength that corresponds to a 3 kHz acoustic field, assuming sound speed c=1500 m/s, is λ=0.5 m. Since the shallowest site where the experiment was conducted was deeper than 80 m, the number of participating modes would be too high; therefore ray theory is more convenient for simulation of signal propagation at the frequencies used.

Each mode is characterized by a phase speed and a group speed of acoustic wave. Because of the dispersive medium, both of them vary with frequency. At high frequencies however phase speed and group speed become asymptotically equal to the sound speed. Therefore only the sound speed is used as a defining parameter of the environment in the ray tracing simulations.

The BELLHOP ray tracing program [10] was used for simulations of the ray propagation. Ray propagation is modeled based on SSPs calculated from the CTD measurements using the Chen – Millero model [23]. In the modeling, the environmental

characteristics were assumed to be both time and space invariant. The bathymetric measurements at the shallow water sites showed that water depth ranged between 80 and 120 m, which could not impact the direct-path arrivals at the hydrophone depths used much differently than a flat bottom.

Tanner-Cortes Bank Site

The site between Tanner Bank and Cortes Bank was in shallow water (Figure 1.1). The 6 AM SSP in Figure 3.1 indicates the existence of two sub-layers in the mixed layer. The upper sub-layer was 15 m deep and the lower one extended down to 27 m. The grossly negative gradients of the other two SSPs indicate that, for the time of the experiment at the site, the mixed layer was not clearly defined during the afternoon measurements. A closer look shows that the noon SSP does have an isothermal surface layer of about 7 m depth. In fact, we cannot be sure whether the 6 AM or the noon SSP is more applicable to the solid line track in Figure 1.2a, that was set in the morning hours.

The shallower source depth was 19 m and was inside the loosely defined mixed layer of the 6 AM SSP. More precisely, it was in the lower sub-layer of the loosely defined mixed layer, yielding a duct that could provide a direct-path arrival at 27 m depth at theoretically infinite range. The bounding grazing angles of the duct can be calculated from the Snell's Law [24] [16]:

$$\frac{c(z = Z_S)}{\cos\theta_S} = \frac{c(z = Z_R)}{\cos\theta_R}$$

Equation 3.1

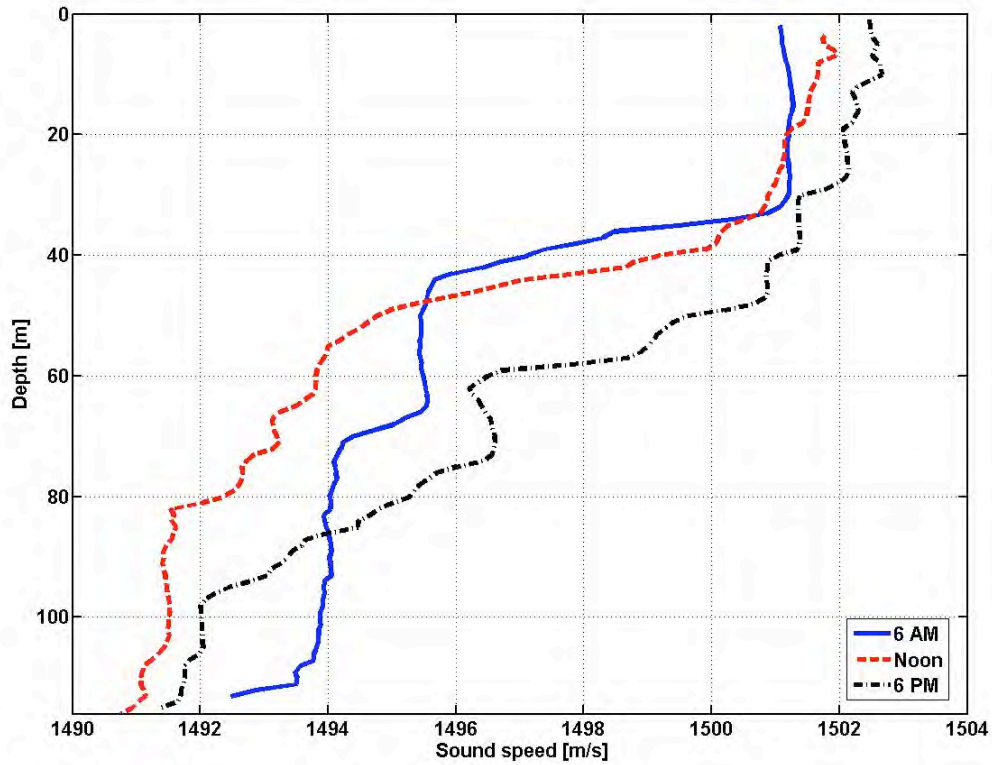

Figure 3.1 SSP at the Tanner-Cortes Bank site, measured on February 20th 2001.

Source and receiver depths are marked with Z_S and Z_R, and angles θ_S and θ_R stand for the grazing angles at the source and at the refraction point, respectively. A beam refraction condition, based on Equation 3.1, is:

$$\theta_S = \cos^{-1}\frac{c(z = Z_S)}{c(z = Z_R)} \quad c(z = Z_S) \le c(z = Z_R)$$

Equation 3.2

The rays trapped in the duct would have take-off angles:

$$\cos^{-1}\frac{c(z = Z_S)}{c(z = Z_L)} \geq \theta_S \geq -\cos^{-1}\frac{c(z = Z_S)}{c(z = Z_U)}$$

Equation 3.3

with positive angles being read clockwise. Depths of the upper and the lower boundary of the sub-layer are marked with Z_U and Z_L, respectively. Equation 3.2 implies that an infinite duct requires a local minimum of the sound speed in the sub-layer. For a 19 m deep source, assuming the 6 AM SSP, the corresponding boundaries are approximately: $0.3° \geq \theta_S \geq -0.6°$.

A receiver at 61 m depth could get direct paths at extended ranges from the beams that refract above the sub-layer, turn downward and upward a few times until they find a way out of the maze of sound speeds, like the thick dashed beam in Figure 3.2a. The shapes of the SSPs in Figure 3.1 exhibit a substantial number of local minima, suggesting countless direct paths at infinite and extended ranges depending on the source/receiver depth.

When a source is at 40 m, because of the downward refracting scenario in Figure 3.2b, caused by the negative gradient of the SSP, there are rays that travel in a group bouncing on the bottom and refracting in the water column without touching the sea surface. Due to the nature of the harmonic spherical waves [16], these beams will add up constructively if the differences in their path lengths are multiples of the wavelengths. More and more beams can be involved in this process as we shift to higher frequencies, because a smaller difference in path lengths can be a multiple of the wavelength. The ray tubes formed that way will have a combined pressure effect on the transducer that could

be larger than pressure due to direct-path arrivals. The overall scenario is similar to surface ducting, just with the sea bottom playing a role of the sea surface.

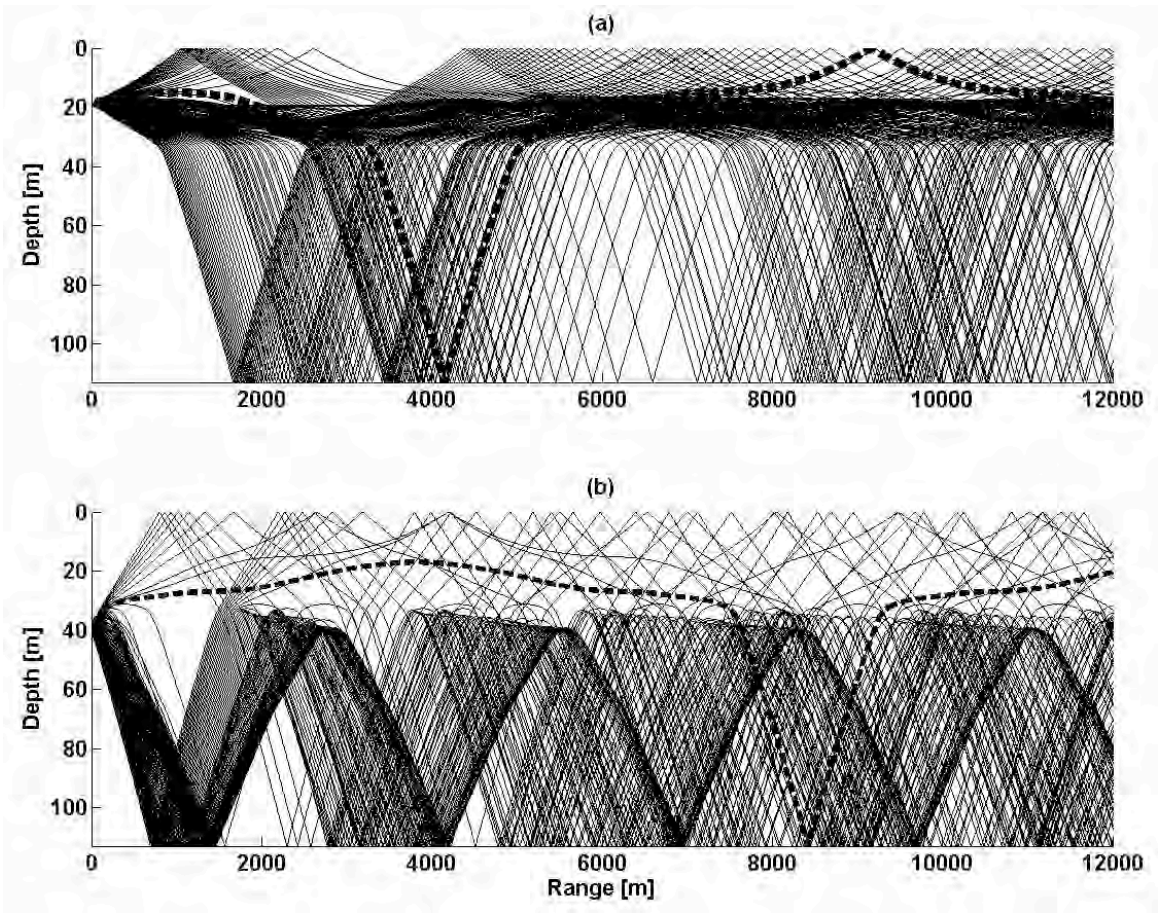

Figure 3.2 Ray tracing for the 6 AM SSP in Figure 3.1. The source depth, the span of the uniformly distributed starting depression angles and the corresponding number of beams are: (a) 19 m, -1° to 1°, 100 beams and (b) 40 m, -5° to 5°, 300 beams, with positive angles being read clockwise. The dashed beams highlight the longest estimated range with a direct-path arrival at 61 m depth.

There are zones where ray windowing [5], caused by refraction of some rays before they reach certain depths, results in no direct-path arrivals. However, some rays, like dashed thick ray in Figure 3.2b, enter the duct and get trapped along a certain range, ultimately turning steeply downward after the source depth and thereby source sound

speed is reached. Those rays could feed direct-path arrivals to receivers at 27 m and 61 m depths, at somewhat longer ranges than the limits set by the ray windowing.

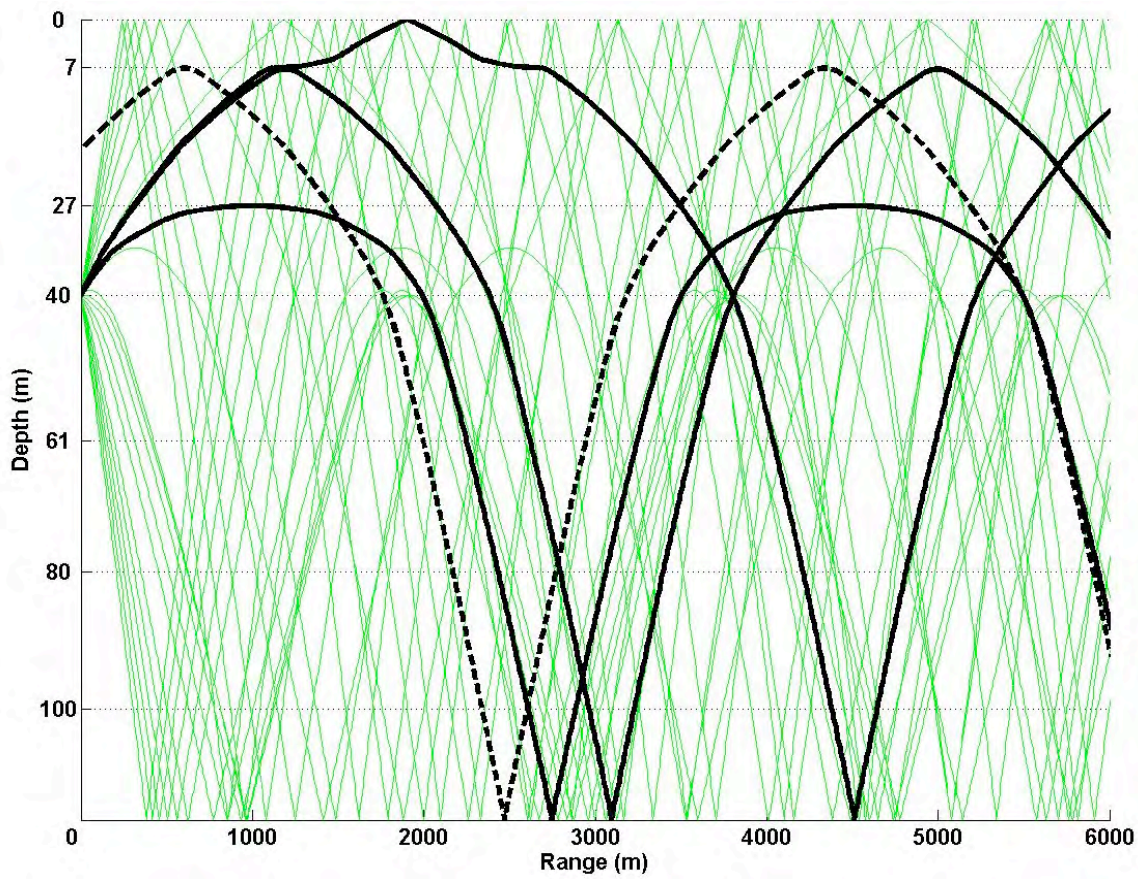

Figure 3.3 A ray tracing diagram, assuming the noon SSP on 20th February 2001 at the Tanner-Cortes Bank site. The dashed line originates from a 19 m source, whereas source depth is 40 m for all the other rays.

Figure 3.3 depicts ray propagation under the noon SSP. A bottom duct is present, but the subsurface duct shown in Figure 3.2a does not exist because of a very shallow mixed layer. That way, direct-path operating range with a 19 m deep source and a receiver at 27 m depth is not a subject to theoretically unlimited direct-path zone, which was the case in Figure 3.2a. On the other hand, the ray windowing effect for a 40 m deep

source is looser than in Figure 3.2b. The highlighted rays illustrate that a deeper source under these circumstances can project a direct wave further because the beams that bounce off the bottom of the isothermal surface layer, which is about 7 m deep, travel longer distances before bouncing.

The SSP shown in Figure 3.4a is a piece-wise linear approximation of the noon SSP in Figure 3.1. An advantage of having a linear gradient for each section of the SSP is the availability of analytical expressions for calculated range and travel time between two points inside an SSP section. These expressions, whose detailed derivations are available in the literature [24], can be summarized into the following two equations for travel time *t* and the corresponding horizontally swept distance *r*:

$$t = \sum_{s=0}^{S-1} \frac{1}{b_s} \log_e \frac{c(z_{s+1})(1+\cos\theta_s)}{c(z_s)(1+\cos\theta_{s+1})}$$

Equation 3.4

$$r = \frac{c(z_0)}{\sin\theta_0} \sum_{s=0}^{S-1} \frac{1}{b_s} (\cos\theta_s - \cos\theta_{s+1})$$

Equation 3.5

The beginning of each sub section (*s*) of an SSP, with a constant gradient b_S, is denoted by an index, with s=0 and s=S indicating the starting and the ending point of the whole trace. For example, if a path from a 40 m deep source to a 27 m deep receiver is

being traced, assuming the SSP in Figure 3.4a, depths z_0 and z_S equal 40 m and 27 m, respectively.

The beams in Figure 3.4b are bound by the beam that is refracted right underneath the sea surface, and the beam that is refracted at 27 m depth, which is the depth of one of the hydrophones in the experiment. The take-off angles of these two limiting beams were calculated based on Snell's Law (Equation 3.1).

In the case of an omni-directional transmitter, each beam inside the fan of refracted beams shown in Figure 3.4b will appear at a depth of 27 m at the same range as a sea surface reflection. The highlighted beams represent the beam that refracts at 27 m depth and the surface reflection that crosses that depth at the same range, assuming a flat surface. The travel time difference for each pair of refracted and sea surface reflected beams in the beam fan for this simplified case is found as:

$$\Delta t = t_S - t_d$$

Equation 3.6

where travel times t_s and t_d stand for surface reflected and direct arrival, respectively, computed by Equation 3.4.

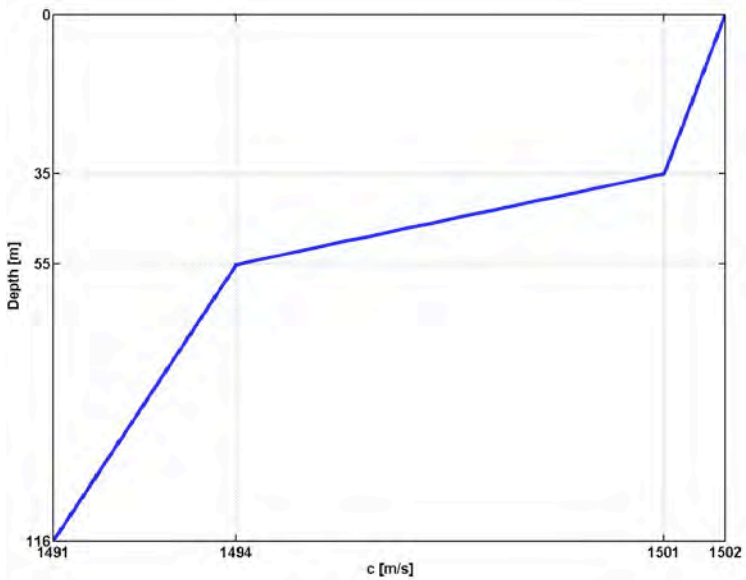

(a)

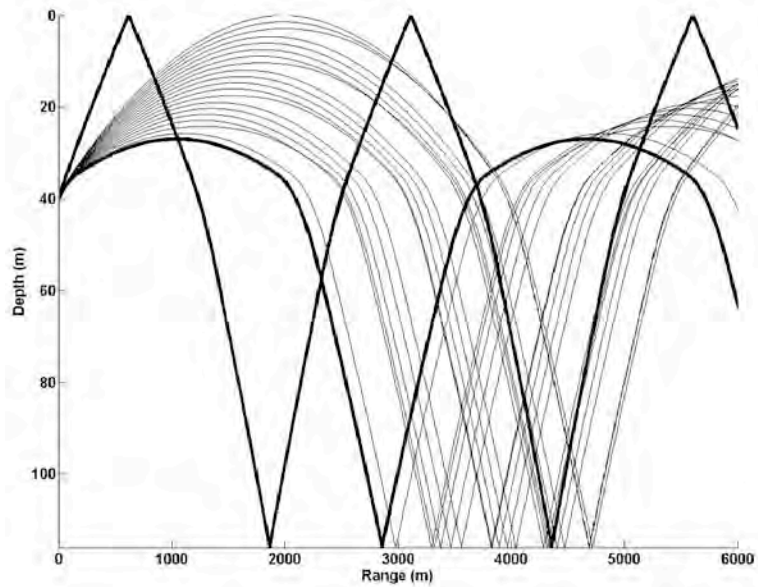

(b)

Figure 3.4 (a) Simplified SSP from Figure 3.1 (b) Thin beams belong between the first angle that gives a direct path at 27 m and the smallest angle of incidence that does not produce the surface reflection. The two thick beams correspond to the first angle that gives a direct path and the sea surface reflected beam that intersects it at 27 m depth.

The travel time difference Δt was calculated for a finite number of beam pairs, intersecting at 27 m depth before refraction points of the refracted beams, and plotted in Figure 3.5. It can be seen that, assuming the SSP from Figure 3.4a, Δt is steeply approaching 0 ms, falling to 10 ms for range R=135.1 m. Past that range time resolution of 10 ms is insufficient for a complete direct path arrival separation from a sea-surface reflection. That zone extends to the range where sea-surface reflections start being windowed out. In Figure 3.4b, it is somewhat before 4 km.

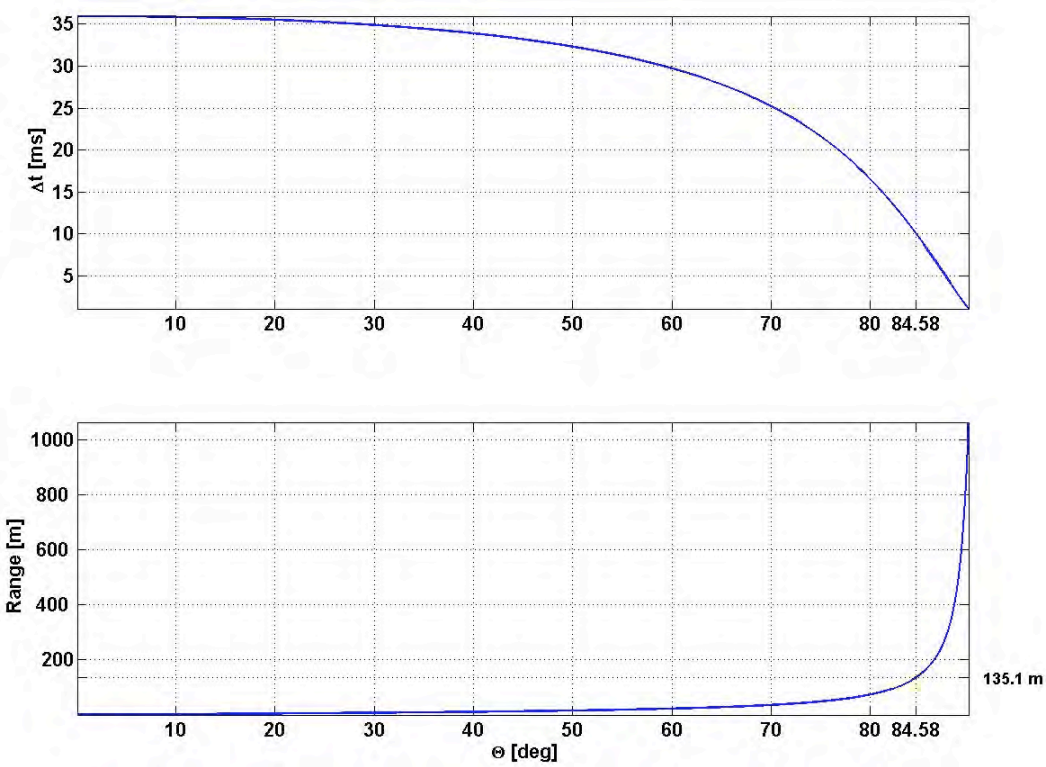

Figure 3.5 Time delay and range distribution for the direct and surface reflected beams that intersect at 27 m depth.

The time difference analysis (Equation 3.6) could be continued for the intersections after the refraction point; however including additional sections of the ray

paths would make it more computationally demanding and the insufficient accuracy of the model would not justify the effort. A more authentic test of existence of direct-path at the ranges of interest is comparison between the measured and modeled TL data, which is presented in Chapter 6.

At the ranges that belong to, or exceed, the downward refracting zone, which is between 1 km and 2 km in Figure 3.4b, the refracted rays start intersecting each other, eventually causing amplitude and phase fluctuations in the intersection points because of the different travel times. Furthermore, the common clutter components, illustrated in Figure 3.6, contribute to the field variations across the water column.

Z_R [m]	$T_B - T_S$ [ms]	$T_{BS} - T_S$ [ms]	$T_{SB} - T_S$ [ms]	$T_{BS} - T_B$ [ms]	$T_{SB} - T_B$ [ms]
27	10.5	10.6	8.4	-1.7	-0.4
61	8.8	10.0	7.8	1.2	-1.0

Table 3.1 Time differences among the clutter components from Figure 3.6. Source depth is 40 m and the range is 3 km. T_S=Surface reflection travel time; T_B=Bottom reflection travel time; T_{BS}=Bottom-Surface reflection travel time; T_{SB}=Surface-Bottom reflection travel time.

Assumed sound speeds for the calculations of the time delays in Table 3.1 are c=1496 m/s, c_s=1499 m/s and c_b=1493 m/s, for the rays that reflect from both the surface and the bottom, the surface only and the bottom only, respectively. The first sound speed is an approximation of the mean value of the SSP in Figure 3.1. It appears to be a fair assumption because a beam that reflects from both boundaries travels through the entire water column. By the same rationale, the other two sound speeds were obtained by

averaging over respectively the upper and the lower portion of the SSP divided at the source depth.

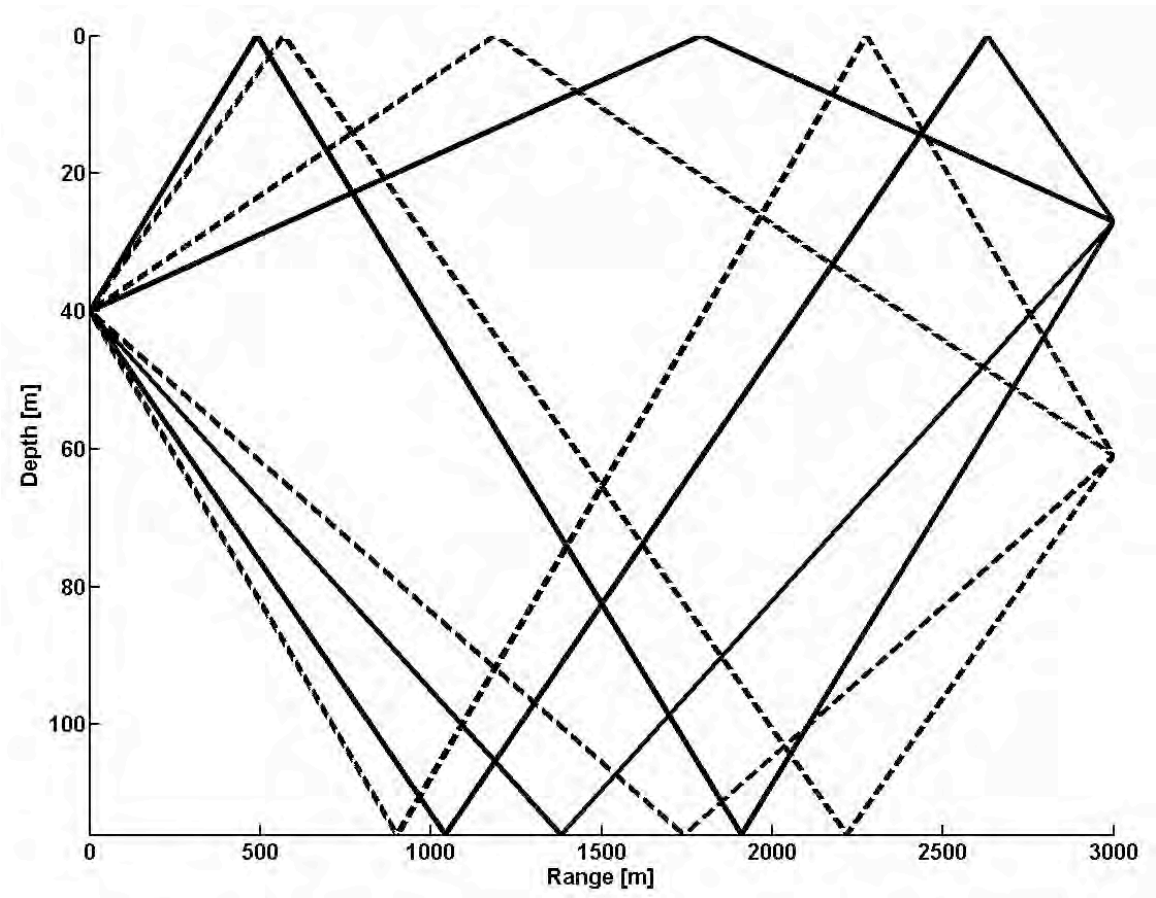

Figure 3.6 Clutter geometry under assumption of a constant sound speed throughout the water column; Water depth 116 m; the solid and dashed lines correspond to the 27 m and 61 m receiver depth, respectively.

Although that simplification of the SSP introduces a two layer model, which according to Snell's law [16] changes the ray paths through refraction at the interface, it is tacitly assumed that the beams do not refract inside the water column. This assumption is justified because the refracting factor equals the ratio of the sound speeds at the interface, which in this case is very close to 1; therefore ignoring the refraction is a

reasonable simplification. The swept distances along the beams in Figure 3.6 for the calculations of the time delays in Table 3.1 were obtained by application of some straightforward geometric laws. The travel times were then obtained by their simple division by the assigned sound speeds.

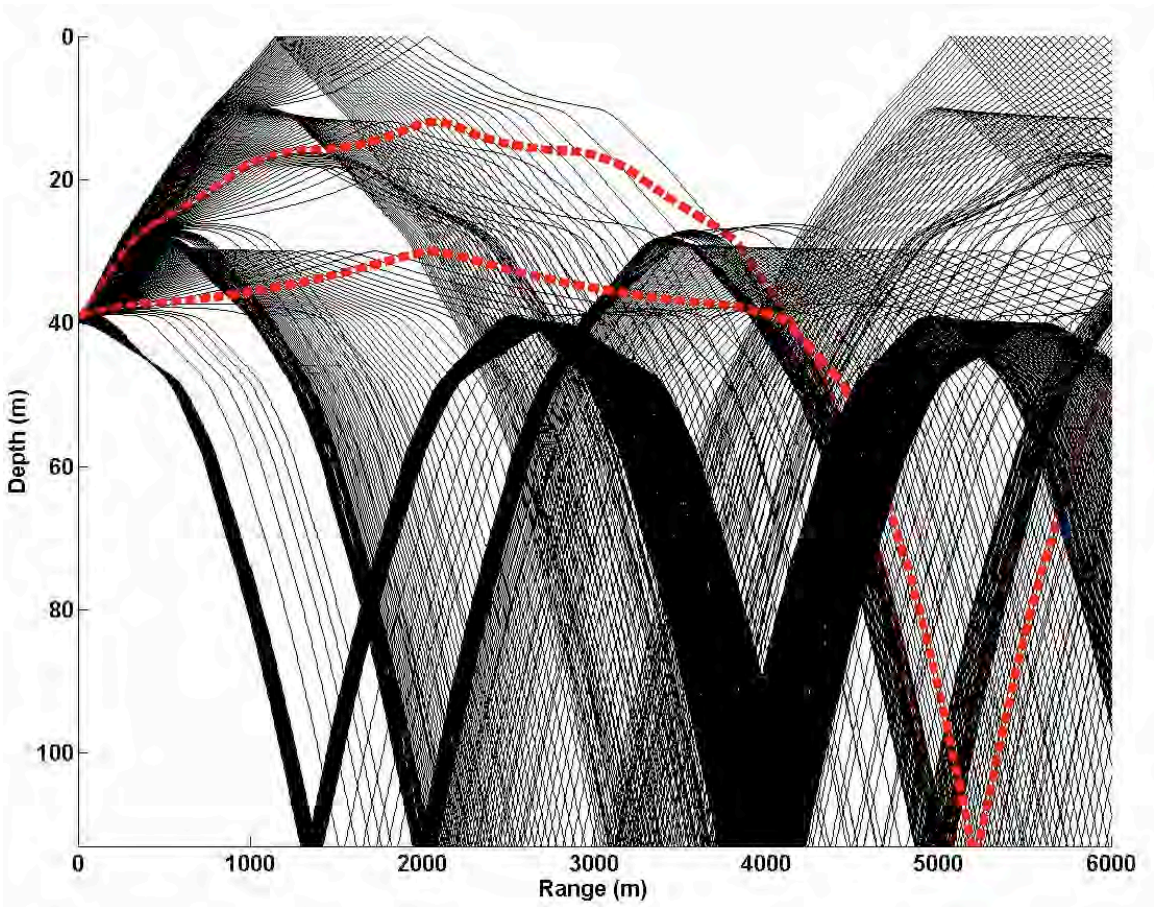

Figure 3.7 Ray tracing for the 6 PM SSP in Figure 3.1 and source at depth 40 m. The starting angles of depression of the 300 selected beams are uniformly distributed inside -3 to 3 degrees window, with positive angles being read clockwise. The upper and the lower dashed beam signify the longest ranges with a direct-path arrival at 27 m and 61 m, respectively.

Finally, the 6 PM SSP could be relevant for the second track (dashed line in Figure 1.2a), set during the afternoon hours (Table 1.1). The source transducer depth

during the second track was kept at 40 m. Figure 3.7 shows a layered example of ray windowing, which is a result of the step-like upper portion of the SSP. The steep falls on the dashed rays happen when the rays, after traveling through a maze of sound speeds, reach the starting speed that is in the downward refracting section. This is another example of how a step-like SSP can extend the direct-path zone.

South of China Point Site

The site South of San Clemente Island's China Point was also in shallow water (Figure 1.1). The afternoon period, when both tracks at this site were run, is characterized by a decrease in the mixed layer depth from approximately 55 m to 30 m (Figure 3.8). Along the first track at this site (solid line in Figure 1.2b), according to the source depth schedule provided in Table 1.2, the source transducer was below the mixed layer before the CPA, and possibly but not definitely in the layer after that.

Figure 3.9 shows that, when transmitted from 35 m depth, with the given SSP, more energy is confined to the mixed layer. When a source is 60 m deep a great amount of energy bounces off the bottom of the mixed layer in a downward refraction and travels inside the bottom duct. The longest direct paths between a source at 60 m and 35 m depth, and a receiver at 27 m and 61 m depth, respectively, are on the highlighted dashed beams. A 27 m deep receiver gets direct path at maximum ranges of about 3 km, for a source at either 60 m or 35 m depth. Because the early afternoon SSP is narrowly shelved around 60 m, when the source is at that depth a part of the transmitted energy is channeled through the narrow layer, allowing direct-path arrivals at 61 m at longer ranges than if the SSP were changing more steeply around the source depth.

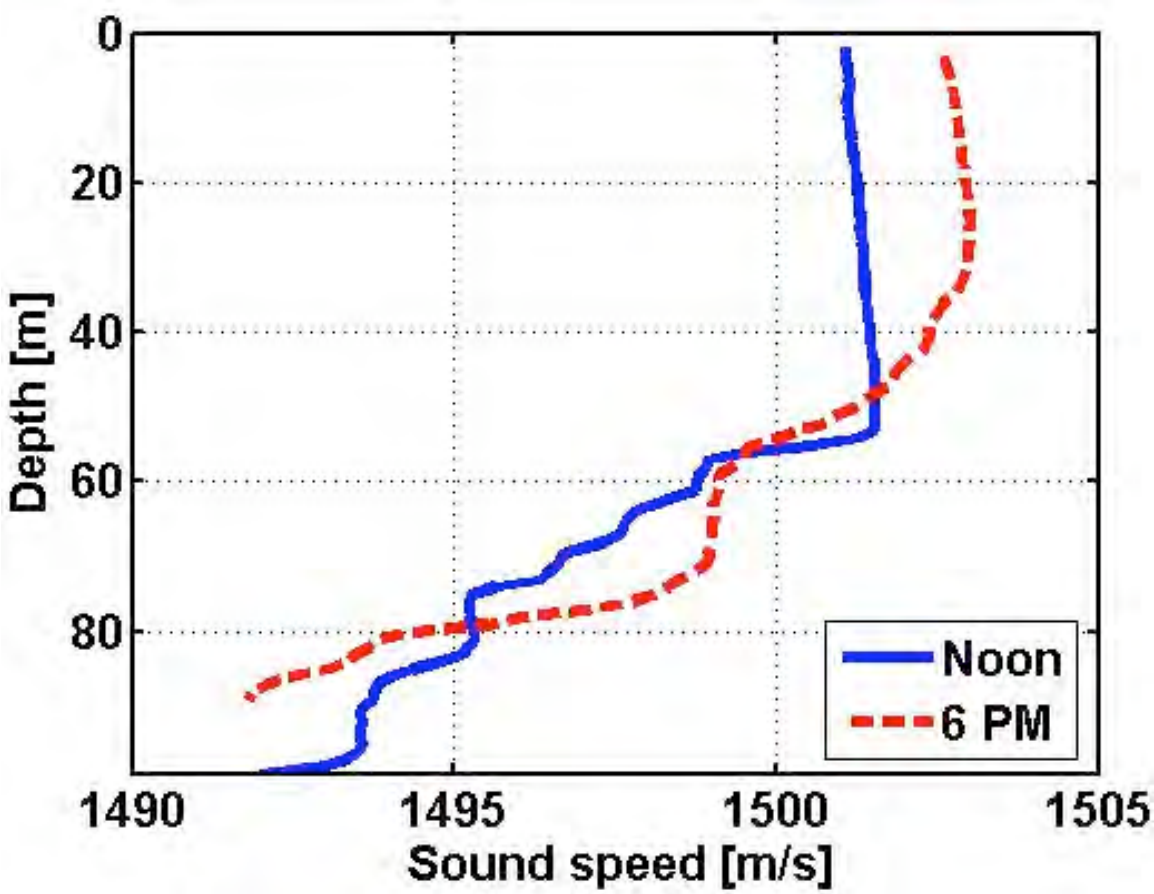

Figure 3.8 SSPs measured at noon and 6 PM on 24th and 19th February 2001, respectively, close to the sonobuoy locations at the South of China Point site.

The beams with take-off angles (θ_S) greater than the angle that satisfies the refracting condition are projected to deeper depths, otherwise they are trapped in the duct. Similar to the derivation above in this chapter that led to Equation 3.3, the duct leakage condition can be derived as:

$$\theta_S > \cos^{-1}\frac{c(z = Z_S)}{c(z = Z_M)} \quad \text{for} \quad c(z = Z_S) \le c(z = Z_M)$$

Equation 3.7

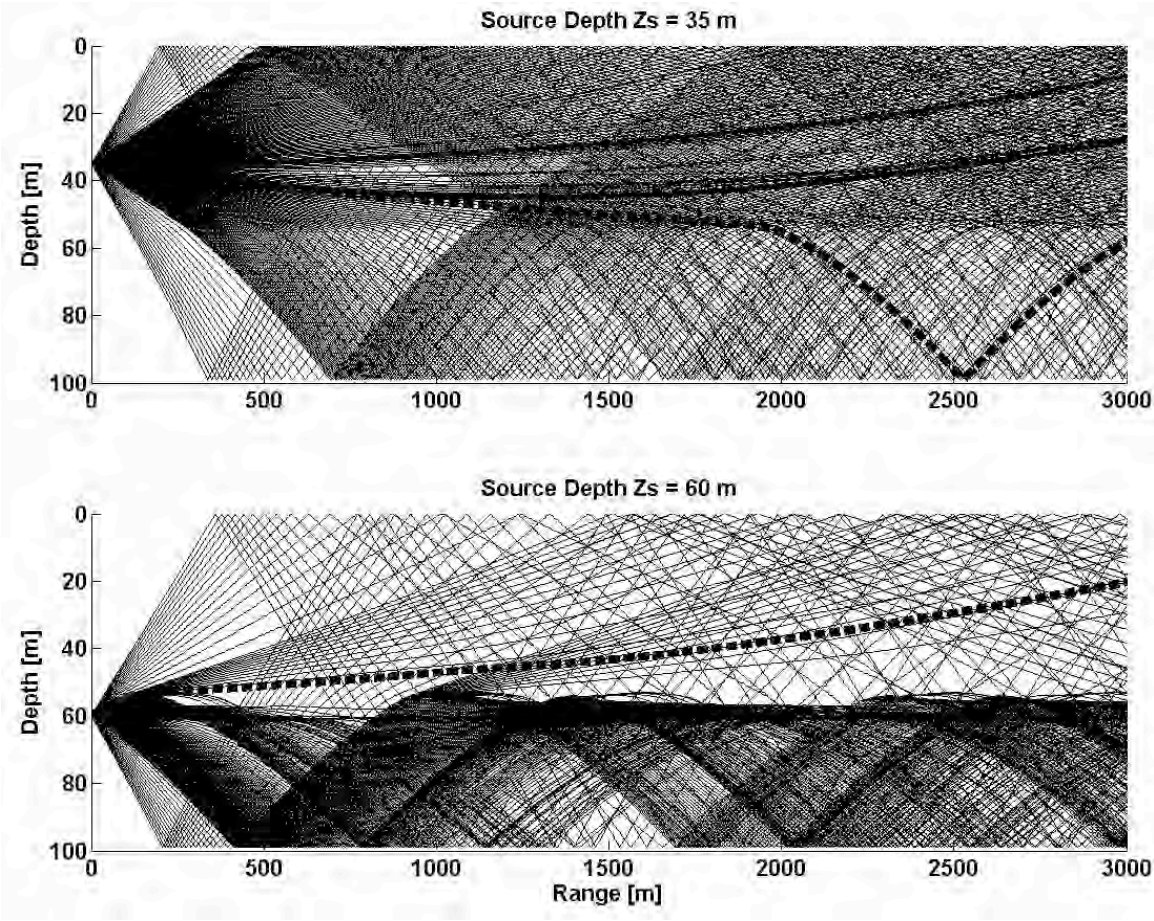

Figure 3.9 Ray tracing for the early-afternoon SSP (Figure 3.8). The dashed beams for a source depth of 35 m and 60 m trace the longest direct-path ranges at 61 m and 27 m depth, respectively.

Z_S is the depth of the source, and Z_M is the depth of the mixed layer. Duct leaking happens after a bundle of beams bounces off a rough boundary, such as the sea surface and the seafloor for the upper and the lower duct, respectively. Figure 3.9 does not illustrate that effect because flat boundaries were assumed in the model, which is sufficient for direct-path analysis. The highlighted dashed beams in Figure 3.9 belong to the group of beams that satisfy the condition in Equation 3.7 and never enter a duct. Notice that, when a source is 60 m deep, direct rays are projected into the complementary section of the water column to longer ranges than in the bottom duct. This excludes

internal ducting in the local-minimum SSP layer because it is not a coherent part of either the bottom or the surface ducting but a local effect that could exist anywhere in the water column.

For a given source depth, number of beams that are projected into a duct, and those that are not, depends on two factors: the layer depth and the SSP steepness in the layer. A bigger value of either of these parameters causes a larger difference between $c(z = Z_S)$ and $c(z = Z_M)$ thereby causing a higher number of take-off angles not to satisfy the condition in Equation 3.7. Finally a greater part of the total transmitted energy is windowed into the layer.

If the late afternoon SSP is employed in a ray tracing simulation, both 35 m and 60 m depths are below the corresponding mixed layer. The major differences in propagation conditions from the noon environment are that for a 35 m source depth, a greater part of transmitted energy gets trapped in the lower section of the water column, and for a 60 m source depth, energy becomes more evenly distributed in depth and there is a slight multi-layer ray windowing that resembles Figure 3.7. For a 35 m deep source, the maximum direct-path horizontal range at 27 m is comparable to the maximum direct-path horizontal range at the same depth for a 60 m deep source in the early afternoon SSP.

Source transducer depth was kept at 18 m all along the second track (Figure 1.2b "dashed" line); thus the source transducer was inside the mixed layer for either SSP in Figure 3.8. The plateaus around 60 m in both SSPs cause somewhat extended direct-path distance for the deeper receiver from the beams that enter the layer under shallow angles. The longest direct-path ranges at 27 m and 61 m depths, assuming the noon SSP in

Figure 3.8, are around 4.2 km and 3.8 km, respectively; assuming the late afternoon SSP in Figure 3.8, the corresponding ranges are around 2.5 km and 3.5 km, respectively.

San Nicolas Basin Site

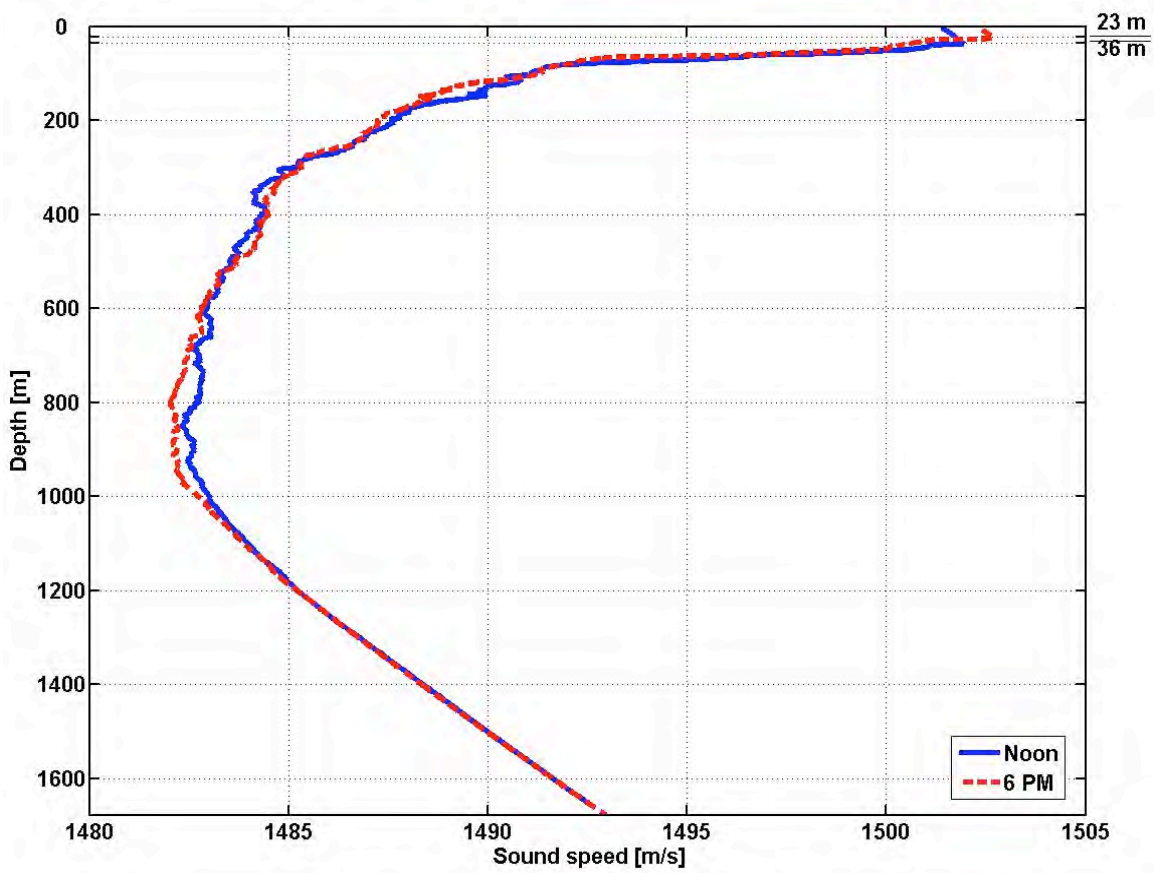

Figure 3.10 An early afternoon and a late afternoon SSP at the San Nicolas Basin site, measured on February 24th 2001.

The site in San Nicolas Basin was in deep water. Both tracks at this site were run during afternoon hours (Table 1.1); thus the SSPs in Figure 3.10 are the most relevant. The noon mixed layer depth was the maximum among the four measurements on that day. It reduced from 36 m to 23 m between the noon and the evening measurement.

Figure 3.11 illustrates acoustic field propagation conditions for a source inside the mixed layer that goes down to 36 m. As explained in the previous section, a great number of beams that originate inside the mixed layer are windowed into the layer and theoretically never leave that part of the water column, forming a surface duct. The beams with take-off angles that satisfy condition in Equation 3.7 are windowed out of the layer, causing a wide shadow zone with no energy directly projected from the source.

Figure 3.12 points out an SSP related difference in the size of the shadow zone, assuming a source in the mixed layer. Both pairs of beams represent the paths along which a direct-path arrival could reach a receiver at the maximum range in and below the mixed layer. A deeper mixed layer with approximately equal SSP steepness allows the upward refracting beam more space, whereas the beam that leaks out of the surface-duct can reach shorter ranges. The former is more convenient for a receiver inside the layer, whereas the latter is better for a deeper receiver.

Since the depth of the 6 PM mixed layer is shallower than 27 m, the shallower hydrophone is below the mixed layer, getting energy directly from the source only from the rays not trapped in the surface duct. That reduces its direct-path distance from direct-path distance obtained with the noon SSP for approximately 1.5 km.

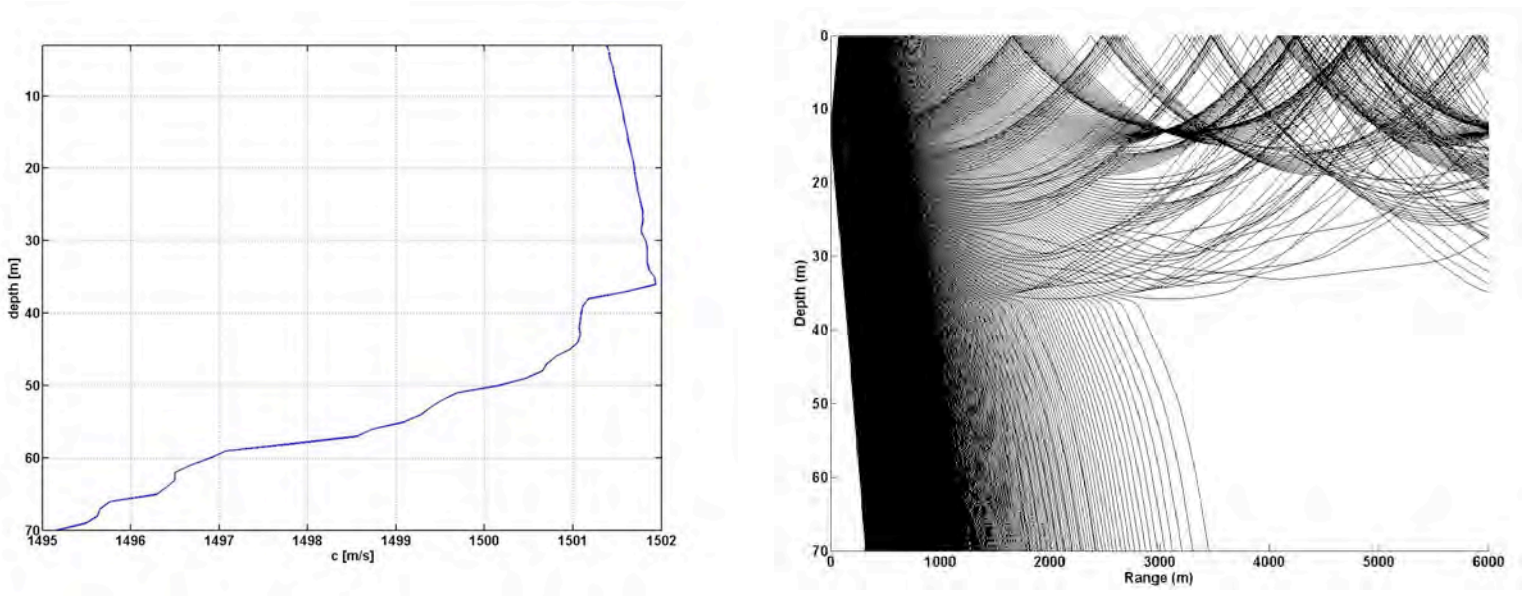

(a) (b)

Figure 3.11 (a) Part of the early afternoon SSP from Figure 3.10 (b) Ray tracing for source at 13 m depth. There are 1000 rays with uniformly distributed angles of depression between -10 and 10 degrees.

Some pulses and background noise corresponding to range between 6.2 km and 7 km are presented in Figure 3.13. By Figure 3.12, there should be no direct-path arrival at either receiver. According to Urick [2], [0]the high frequency sound field at long ranges below the layer is in fact surface-scattered sound. At the ranges covered in the figure, bottom reflections can still be expected to have enough energy to reach the receivers that are placed close to the surface. The first arrival at the shallower receiver was most likely carried in-duct, while at the deeper hydrophone it leaked out of the duct. The latter has lower magnitude because the leaked beams scatter off the sea surface under steeper angles than those trapped in the layer, thereby experiencing smaller reflection coefficient [16].

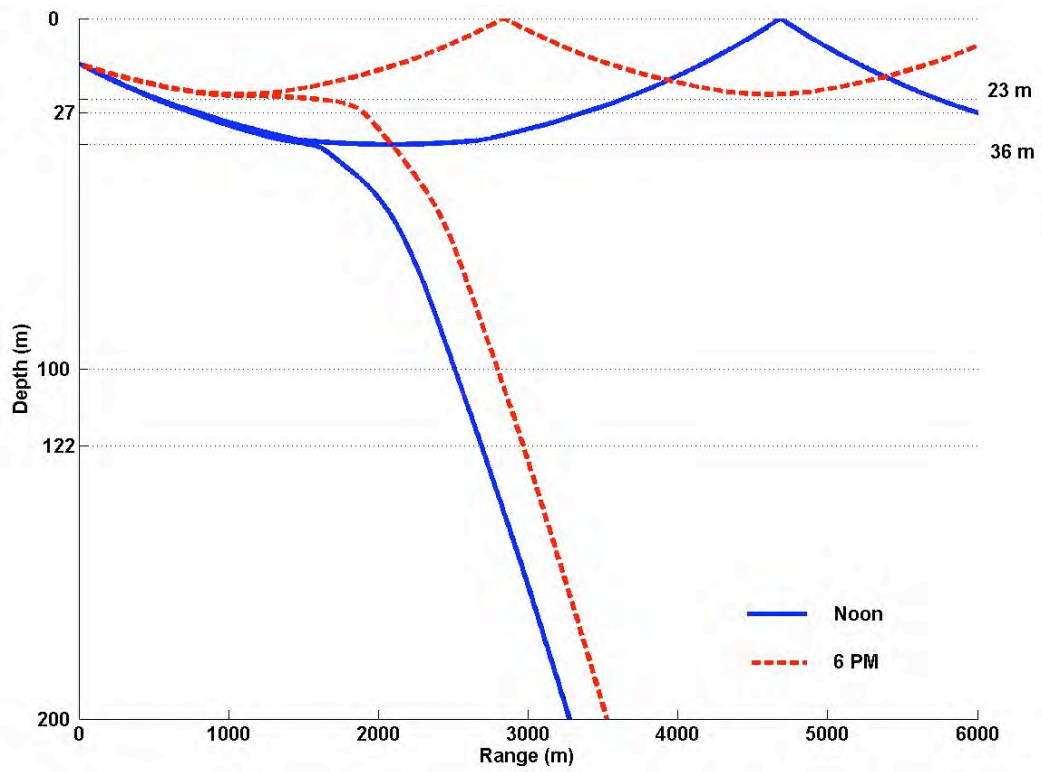

Figure 3.12 Shadow zone bounding rays from a 13 m source by the two SSPs in Figure 3.10.

Generally an important aspect of the duct-leaked rays is that they can refract up from the deep water channel and make a very strong arrival at ranges on the order of several tens of kilometers [25]. Those ranges are out of the scope of the experiment therefore any chance of an existence of that kind of arrival is excluded.

A sketch similar to that shown in Figure 3.6 can be drawn for the deep water SSP of Figure 3.10. It would contain the same components, just naturally longer ranges. In the case of a shallow receiver, beams that bounce off the sea surface under a steep angle merge with the beams that go straight to the bottom. Therefore these arrivals are not likely to be separable. Table 3.2 provides some indicative travel time differences that should support this explanation. Assumed sound speeds for the calculations of the time delays in Table 3.2 are c=1493 m/s, c_s=1498 m/s and c_b=1488 m/s, for the rays that reflect from both the surface and the bottom, the surface only and the bottom only, respectively.

Z_R [m]	$T_B - T_S$ [ms]	$T_{BS} - T_S$ [ms]	$T_{SB} - T_S$ [ms]	$T_{BS} - T_B$ [ms]	$T_{SB} - T_B$ [ms]
27	585.5	587.5	552	2.0	-3.1
122	554.3	617.6	551	63.3	-3.3

Table 3.2 Time differences among the clutter components similar to Figure 3.6. Source depth is 13 m and the range is 6 km. T_S=Surface reflection travel time; T_B=Bottom reflection travel time; T_{BS}=Bottom-Surface reflection travel time; T_{SB}=Surface-Bottom reflection travel time.

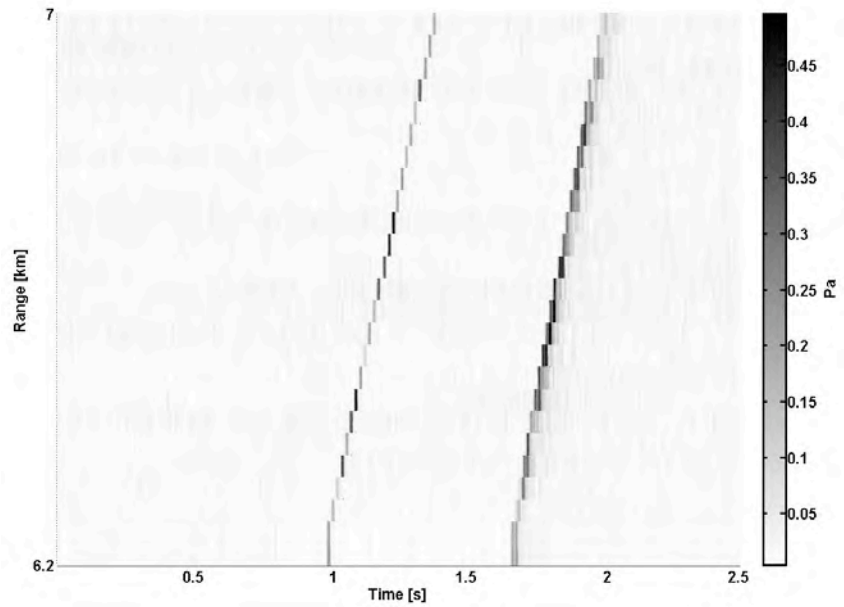

(a)

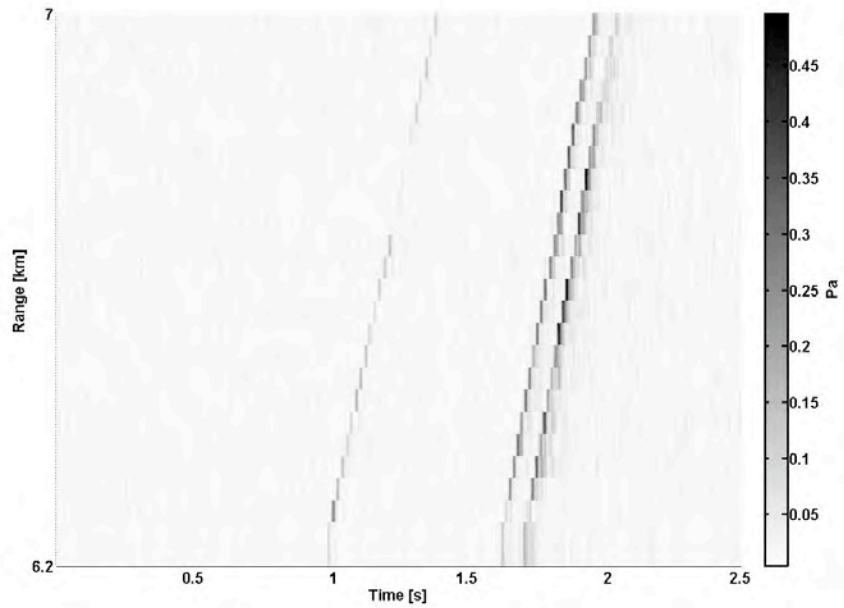

(b)

Figure 3.13 Color scaled envelopes of a set of consecutive pings pre-filtered around 10 kHz for a section of the "solid line" track in Figure 1.2c. Time of the first arrival is normalized to 1 s. Sonobuoy depth is (a) 27 m (b) 122 m.

Along the track at the deep site the ship was moving away from the sonobuoys, with the source transducer facing the hydrophones. Since the hydrophones were offset not only vertically but also horizontally, the deeper hydrophone was closer to the source in this case. That is why the signal in Figure 3.14 that comes from the 122 m deep receiver appears before the signal from the shallower receiver.

The values in Table 3.2 do not match the time differences between the first and the later arrivals in Figure 3.14 accurately. Nonetheless, the greater time difference between the second and the first arrival in the deeper channel over the shallower channel supports the anticipated order of arrivals.

For a communication channel defined by the early afternoon SSP from Figure 3.10 and the source depth Z_S=83 m, the beam that is marked by the shallowest downward refraction, indicated in Figure 3.15, sets the limit to non-reflected arrivals at a receiver at 122 m depth to around 2.5 km. The shallowest and the deepest upward refractions happen at ranges greater than 20 km, as indicated in Figure 3.15. The ray tube bound by these beams will produce a new group of non-reflected arrivals for a 122 m receiver at around 40 km, but that is far out of the range of the experiment.

Although the source is below the mixed layer, shadow zones are present. Since the mixed layer depth is 36 m, rays are windowed before they reach 27 m depth therefore the shallower receiver was subjected to ray windowing. The only non-reflected beams it can get are those that enter the mixed layer starting by satisfying the condition in Equation 3.7, with depression angle (θ_S) viewed counterclockwise. According to Figure 3.15 the longest direct path range for that receiver is around 3 km.

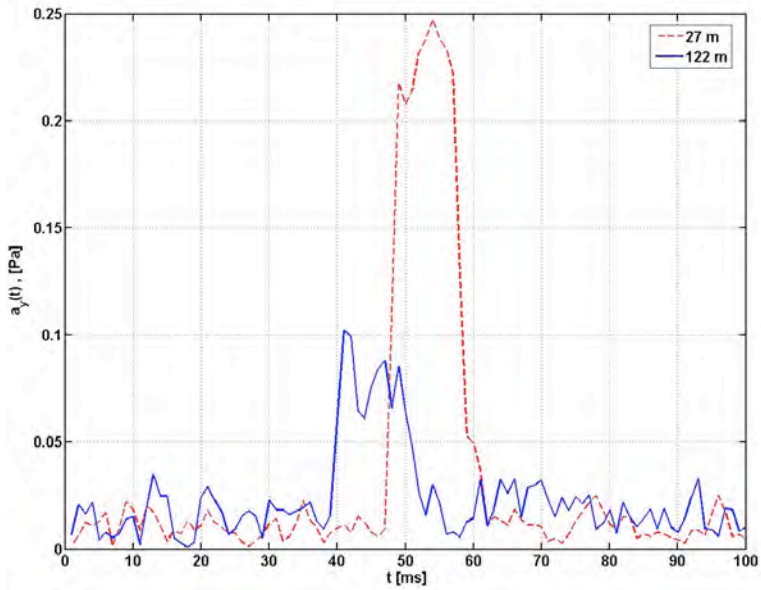

(a)

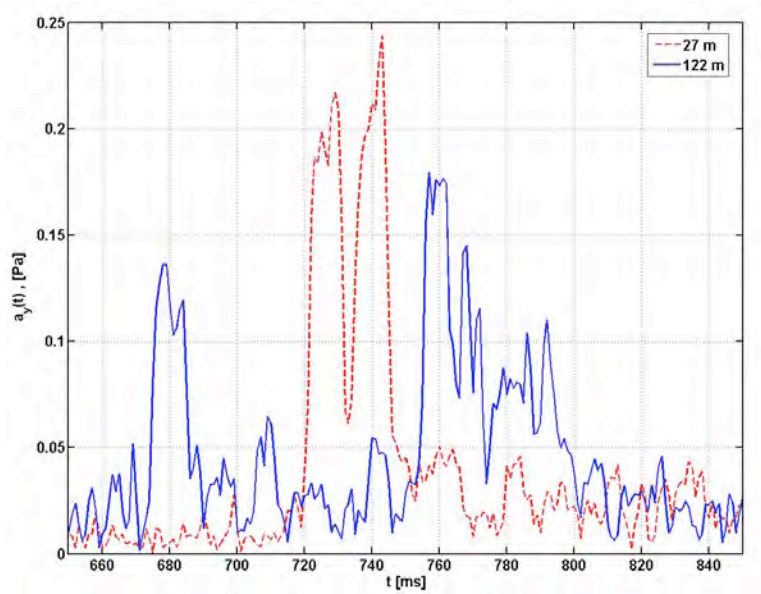

(b)

Figure 3.14 Envelopes of the 10 kHz signals from 6 km range with 13 m source depth: (a) First arrivals. (b) The later arrivals.

Ray tracing with the 6 PM SSP shows that maximum direct-path distances at 27 m and 122 m depth are 2.3 km and 3.3 km, respectively. The maximum direct-path distance at both 27 m and 122 m is determined by the bundles of beams that refract at the depth of the bottom of the mixed layer, which is now at 23 m depth. The almost constant sound speed in a very narrow layer around the bottom of the mixed layer causes sound channeling to somewhat longer ranges than would be the case with a smoother SSP. The layers in an SSP that cause sound to be projected through narrow channels, as mentioned throughout this chapter, increase variability of direct-path distance.

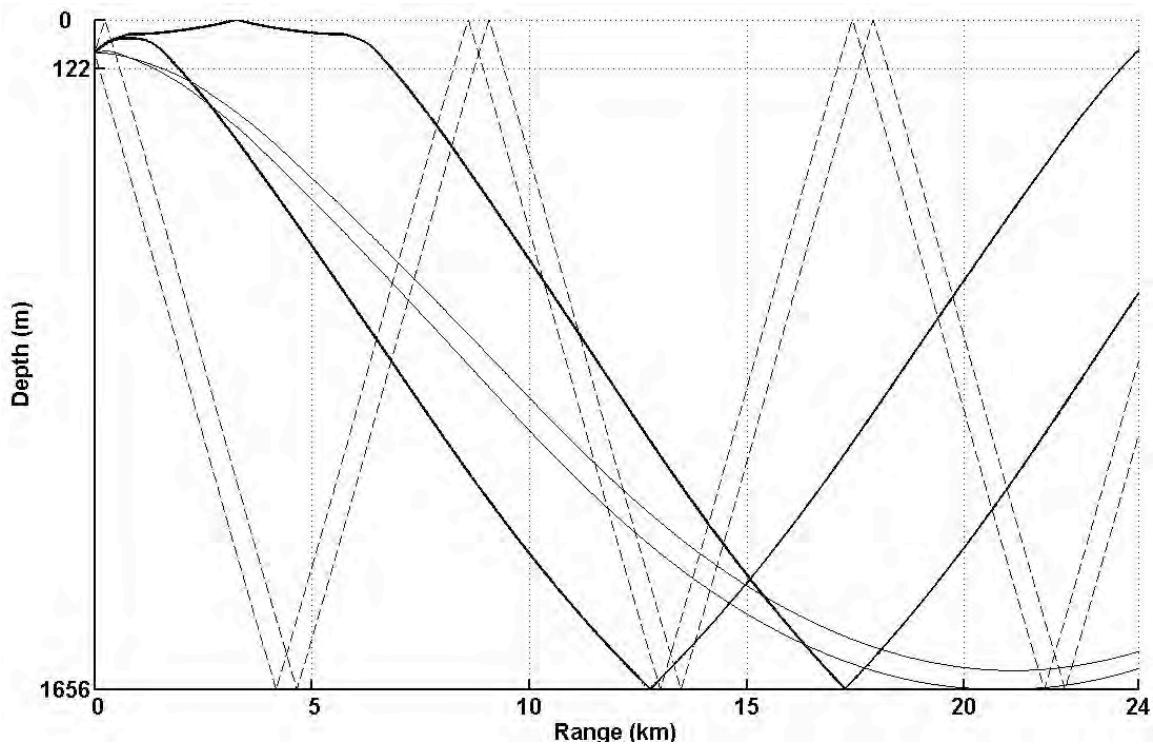

Figure 3.15 Some indicative beams for source depth of 83 m and the early afternoon SSP in Figure 3.10 from February 2001 in San Nicolas Basin.

Ferla and Porter [5] provided an analysis of the optimal receiver depth for bi-static sonar systems, based on a summer and a winter SSP from deep water in the Mediterranean Sea. A conclusion was that if the source depth is known, then the best receiver depth is either the source depth or the conjugate depth (where the sound speed is the same as that at the source). In terms of ray theory, they explained this phenomenon as a combined effect of ray windowing and ray tube projection. First, whenever the sound speed is greater than that at the source, then some of the rays corresponding to shallow take-off angles are turned before reaching the receiver and therefore make no contribution. Secondly, those particular depths where the average ray angle at the receiver is shallowest are favored where the receiver sound speed is less than the sound speed at the source. This in turn occurs when the receiver sound speed is the same as that at the source. In fact, both of these effects were taking place at the shallow water sites except that the source depth did not have its conjugate pairs.

The average value of the mixed layer in the region is 50 m for that part of year [17]. Therefore direct-path arrivals can be expected at shorter or longer ranges on a different day, which is why the analysis based on the SSPs in Figure 3.10 provides an isolated perspective. For instance, Urick [2] pointed out that over short distances the thickness of the mixed layer may vary because of internal waves in the thermocline below. However, importance of the foregoing analysis is for understanding some major characteristics of the sonar signal propagation in the area at that time of year.

Summary

Ray propagation simulations showed that transmission in shallow and deep water featured ray-windowing effects at short ranges (< 3 km) and ducting at mid/long ranges (> 3 km). Ray windowing limited direct path distances to a few kilometers, independent of frequency. For a source in the mixed layer, with increase in the mixed-layer depth, the direct-path distance was shown to increase in, and decrease below, the mixed layer. If a source and a receiver were below the mixed layer, the downward refracting medium would shed direct-path beams to longer ranges if the mixed layer were shallower. The SSPs exhibited a number of local minimum sub-layers, suggesting extended direct-path ranges, especially if a source and a receiver were in such a layer.

CHAPTER 4

BACKGROUND NOISE

Three basic kinds of underwater noise [26], relevant for a bi-static setup, emerge in the sonar process: *radiated noise*, *self-noise*, and *ambient noise*. Radiated noise is the acoustic output of marine vehicles, such as ships, submarines, autonomous underwater vehicles (AUV), etc., which can be received by sensors that are not associated with the systems of the noise-generating vehicle. Noise spectra of radiated noise are of two basically different types [2]. One type is *broadband noise* having a spectrum that is a continuous function of frequency. The other basic type of noise is *tonal noise* having a discontinuous spectrum. The radiated noise of vessels consists of a mixture of these two types of noise over much of the frequency range and may be characterized as having a continuous spectrum containing superposed line components. Here, radiated noise from the ship that towed the source transducer during the experiment represented undesired sound that impacted the sound pressure level (SPL), especially at short ranges.

Self-noise differs from radiated noise in that the measurement hydrophone is located on board the noise-making vessel and stays/travels with it, instead of being at a location some distance away. Since the hydrophones were attached to a couple of simple moored/floating sonobuoys without an engine, they were not affected by this kind of noise. However, the reference hydrophone was constantly exposed to the machinery noise from the ship, including the propeller noise. Self-noise of a ship or an underwater

vehicle used in communication can be calibrated, but the environmental impact on propagation causes the machinery noise radiated on the transmit side of a communication link to be yet another unknown for a sonar design engineer.

Ambient noise is the noise associated with the given environment and is the limiting noise, if and when the other components are sufficiently reduced or eliminated. Its level depends on various factors such as wind speed and distant shipping, and varies with frequency. According to Wenz [26], from about 500 Hz to 25 kHz, the usual slope is negative at −6 dB/oct to −5 dB/oct. The source of this noise is in the agitation of the sea surface and, as it was shown by earlier measurements, the NLs correlate well with wind speed and wave-height. Above 25 kHz thermal noise, associated with the molecular agitation in the sea, is a significant factor, yielding a slope of 6 dB/oct, comprising the noise threshold at frequencies about 50 kHz and above.

The sites where the experiments were conducted are in the vicinity of the Southern California Seacoast, with shipping noise from the Port of Long Beach (main cargo port in Southern California), and the San Diego Navy Base, and ship traffic with Mexico. According to Urick [2], shipping noise is expected below 1 kHz when it originates from distant shipping. The average wind speed in the study area during the experiments was between 6 m/s and 8 m/s [27].

Based on the samples from 10 s pause-time intervals between two consecutive pings, noise PSD was calculated in MATLAB using the Welch method of averaged periodograms [28]. The definition of Periodogram for a sequence y(n) sampled at frequency f_s is:

$$PSD(k) = \frac{\frac{1}{N}\left|\sum_{n=0}^{N-1} y(n)w(n)e^{-j\frac{2\pi}{K}kn}\right|^2}{f_s}, \qquad k = 0 \ldots K-1$$

Equation 4.1

Window function w(n) is N points long, thereby setting the duration of the averaging interval. Welch's method averages PSD of all the participating frames, calculated by Equation 4.1. A time window of 5 seconds was used here for most of the PSD calculations. The length of a frame was 1024 points (=10.24 ms for f_s=100 kHz), and each frame was windowed by the Kaiser function [29] with parameter β=2.5, with 50 % overlap. The number of samples in frequency domain (K) should be chosen to meet a desired spectral resolution; K=N=1024 was used here.

Tanner-Cortes Bank Site

The noise spectrum in Figure 4.1 has an increasing trend. Although it depends on the type of ship and sonar, self-noise usually decreases in at frequencies higher than 1 kHz [2]. The unexpected elevation of the noise spectrum may be caused by overwhelming shallow water reverberation or by another ship/sonar activity in the vicinity.

Figure 4.2a and b show that, at the shallower hydrophone, the noise spectrum has a broad maximum around 7 kHz, whereas noise at the deeper hydrophone tends to decrease with increasing frequency within the observed frequency band. It is unlikely that the 7 kHz hump was caused by the radiated noise from the ship towing the source

transducer because the noise spectrum in Figure 4.1 does not contain a local peak in that frequency range other than the three tonal components between 5 kHz and 10 kHz. Notice a similar relation between the spectra for the other two local peaks, one between 10 kHz and 15 kHz, and the other one around 28 kHz. Between 15 kHz and 25 kHz, the shallower receiver was by 5 dB (re 1 $\mu Pa^2/Hz$) noisier on average than the deeper receiver. The noise picture on this side of the track is more likely to be related to ambient noise because propeller noise was shaded by the ship.

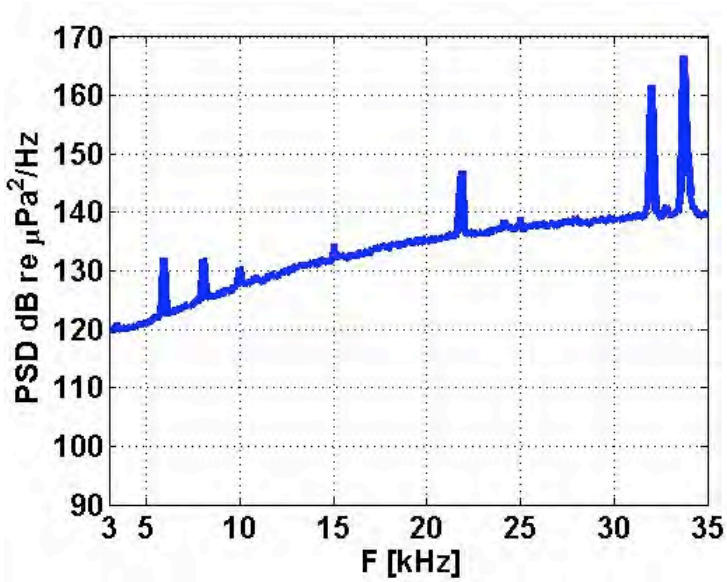

Figure 4.1 Noise PSD at the reference hydrophone (3 m away from the source), measured at Tanner–Cortes Bank (Figure 1.2a, solid line). Conversion from voltage to pressure was done with the response in Figure 1.6.

Due to the presence of strong intermittent noise (about 1.5 s repeating period) between 27 kHz and 30 kHz (Figure 1.7) at the CPA, the time window for the PSD in Figure 4.2c and d was half a second wide. The length of the Kaiser window was set to 512 points to include more frames for averaging.

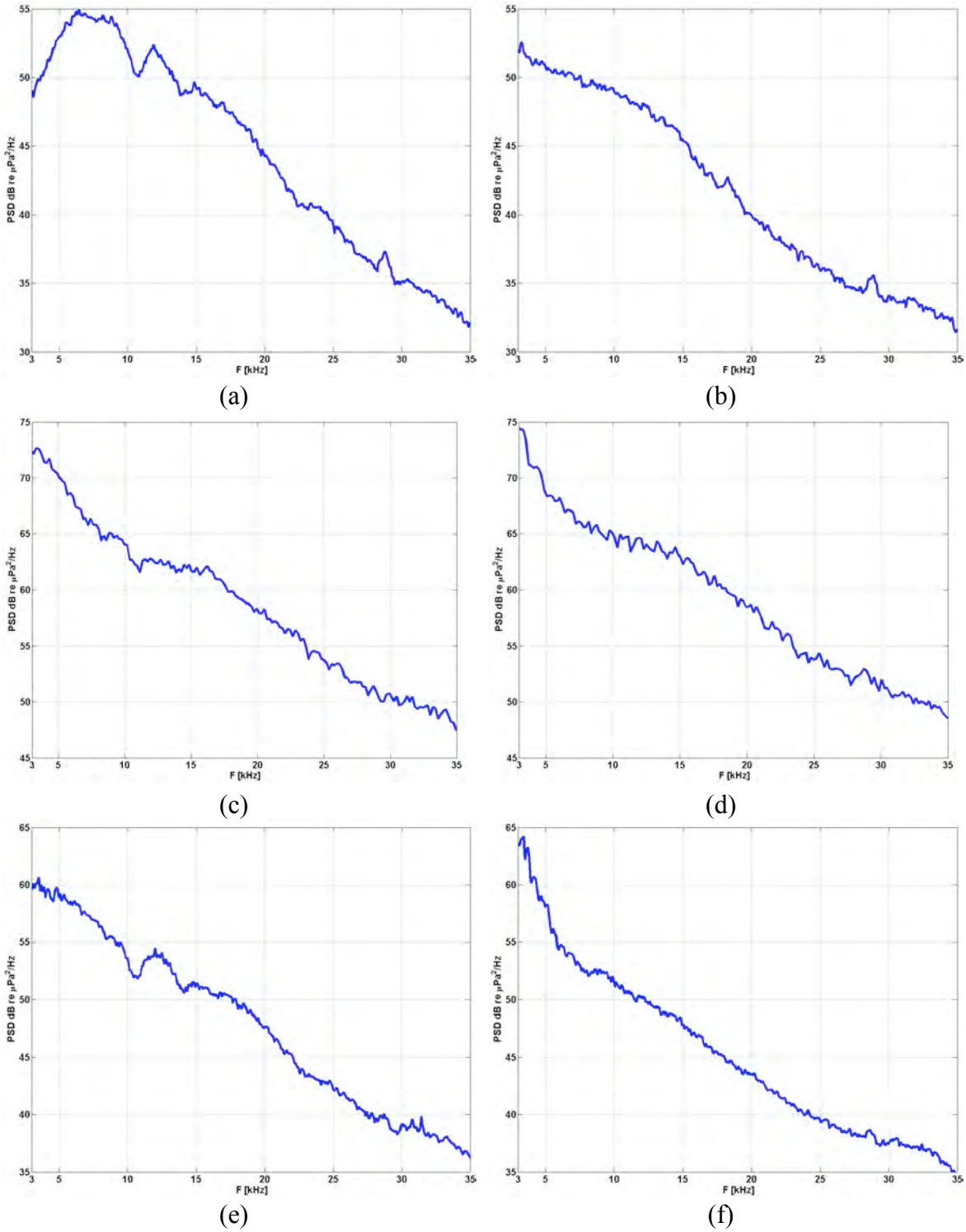

Figure 4.2 Noise PSD at Tanner-Cortes Bank (Figure 1.2a, solid line); approximate range and hydrophone depth, respectively, are: (a) -3.5 km, 27 m; (b) -3.5 km, 61 m; (c) 200 m, 27 m; (d) 200 m, 61 m; (e) 3.5 km, 27 m; (f) 3.5 km, 61 m; negative range refers to the section before CPA.

It is apparent in Figure 4.2 that the propeller noise tends to bring up the NL at frequencies below 5 kHz. The section of the track that corresponds to Figure 4.2c and d is the noisiest because the propellers of the ship towing the source transducer were facing the moored hydrophones and the distance between them was the shortest along the track. Figure 4.2e and f illustrate the NL at longer range, but the ship's propellers were still facing the hydrophones, which is why that section was several dB (re 1 $\mu Pa^2/Hz$) noisier than the section in Figure 4.2a and b, taken at the same distance from the sonobuoy.

Based on the PSD of the noise recorded at two different depths, and shown in Figure 4.2, it can be noticed that in terms of the range, on average, the corresponding NL at both depths follows the order:

$$NL(200\ m) > NL(3.5\ km) > NL(-3.5\ km)$$

Equation 4.2

Although the NL is expected to have a slope between -5 dB/oct and -6 dB/oct in this part of the spectrum, different sources of noise variability like those of biological origin, bubbles, the influence of hydrostatic pressure, or some kind of intermittent man made noise can increase the level of uncertainty in NL assumption for various depths and frequencies [2]. According to Table 4.1, the noise spectrum slope at 27 m and 61 m is somewhat shallower and steeper than -6 dB/oct, respectively.

Octave [kHz]	Depth [m]	r = -3.5 km	CPA	r = 3.5 km	Average [dB/oct]
3 - 6	27	6	-3	-1	
	61	-2	-5	-5	
5 – 10	27	-3	-5	-5	
	61	-1	-5	-7	
10 – 20	27	-5	-7	-7	
	61	-9	-6	-8	
15 – 30	27	-15	-12	-12	
	61	-12	-12	-9	
Average	27	-4.25	-6.75	-6.25	-5.75
	61	-6	-7	-7.25	-6.75

Table 4.1 Average slope (dB/oct) of the noise spectra from Figure 4.2. Negative range refers to the section before CPA.

Figure 4.3 illustrates signal-to-noise ratio (SNR) at three different frequencies. The first snapshots, at the bottoms of the figures, start 2 seconds before the detected pulse, while the subsequent snapshots are simply translated 11.6 s (10 s (transmit down time) + 1.6 s (ping duration)=11.6 s) later.

As stated earlier in this section, the background noise becomes stronger as the towing ship approaches the CPA and starts moving away from the sonobuoys, having its propellers facing the hydrophones. At 3 kHz (Figure 4.3a and b), the signal does not stand out of the background noise at either hydrophone, which is partly because of the subdued SL (Figure 1.5a). The NL at the deeper hydrophone was increased more after the CPA than the shallower hydrophone NL, but the signal was also stronger at that depth before the hydrophones were caught by the radiated noise. The downward refracting environment at this site (Chapter 3) apparently stimulated energy radiation, including background noise, towards the bottom.

The signal at the shallower hydrophone appears to be stronger at 10 kHz (Figure 4.3c and d). The SL at 10 kHz was among the strongest (Figure 1.5a), which is naturally

followed by strong boundary reflections. The apparent gain is an outcome of the strong sea-surface reflections that in this view cannot be distinguished from direct path arrivals.

Notice that, although the SL at 30 kHz was approximately the same as at 3 kHz, the signal at 30 kHz (Figure 4.3e and f) does stand out of the background noise even in the noisiest section. Thus 30 kHz can be claimed optimal frequency in this particular scenario in terms of power consumption, and bit-rate maximization and acoustic modem downsizing.

The harmonics, whose possible causes are explained in Chapter 1, in Figure 4.3e and f correspond to the fundamental frequencies of 10 kHz and 15 kHz, at which the transmit pulses were between 15 and 20 dB (re 1 $\mu Pa^2/Hz$) stronger than the 30 kHz pulse (Figure 1.5a). They represent highly correlated noise in the post-processing pulse detection, which is a subject of Chapter 5.

The broad maxima between 5 kHz and 10 kHz and between 10 kHz and 15 kHz that exist in Figure 4.2a were observed as well in the noise spectra for the corresponding section of the second track at this site (dashed line in Figure 1.2a). The broad maximum between 12 kHz and 20 kHz in the noise spectrum in Figure 4.4a is not notable in Figure 4.2e that counterparts the ship position with respect to the hydrophones at the first track of this site experiment. It did not appear as a broad maximum in the noise spectrum of the same hydrophone when the ship was closer to the hydrophones on the same side of the CPA at this track because the radiated ship noise accentuated frequencies below 12 kHz (Figure 4.2c), but the NL in that frequency band was approximately the same.

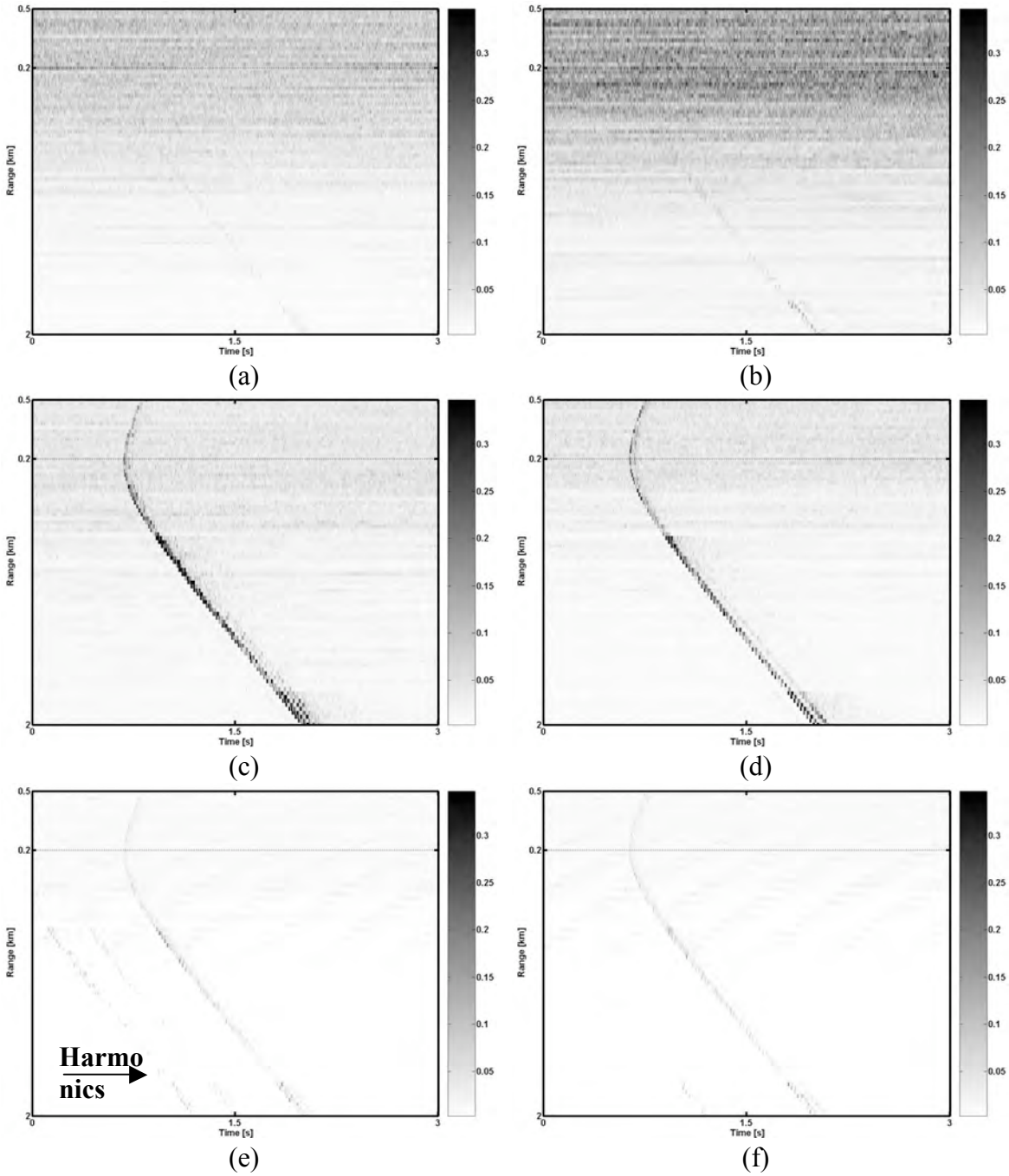

Figure 4.3 Color scaled envelopes of a set of consecutive pings from the section of the "solid line" track in Figure 1.2a that crosses the CPA (range=200 m). Source depth: 40 m before CPA, 19 m past CPA. Carrier frequency and hydrophone depth, respectively, are: (a) 3 kHz, 27 m; (b) 3 kHz, 61 m; (c) 10 kHz, 27 m; (d) 10 kHz, 61 m; (e) 30 kHz, 27 m; (f) 30 kHz, 61 m.

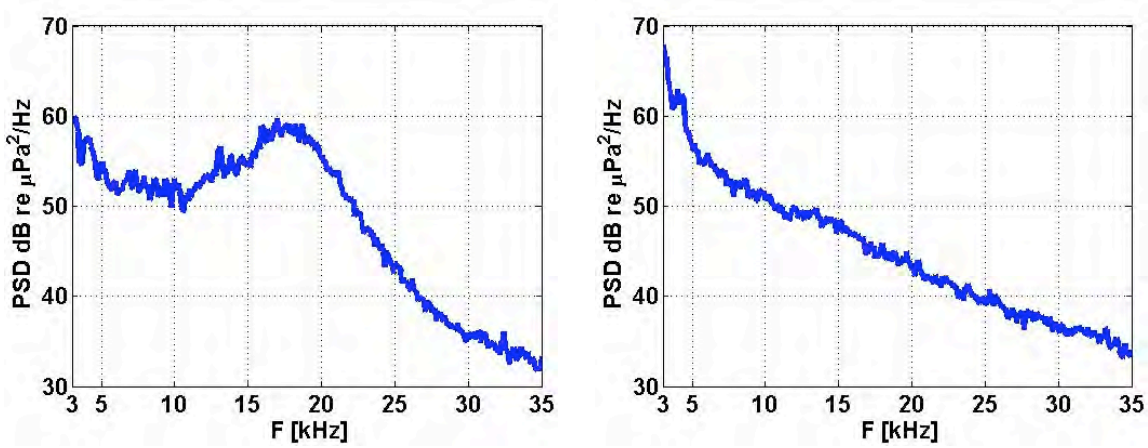

(a) (b)

Figure 4.4 Noise PSD at Tanner–Cortes Bank (Figure 1.2a, dashed line). The ship with the source transducer was moving away from the sonobuoys at a range of about r=3.5 km. Hydrophone depth: (a) 27 m (b) 61 m.

South of China Point Site

Noise PSD of the reference hydrophone at the China Point site was identical to the corresponding PSD at the Tanner-Cortes Bank site (Figure 4.1). Being closer to San Clemente Island (Figure 1.1), this site was exposed to reflections from the island's shore and focusing by a local slope of the seafloor to the shore more than the Tanner-Cortes Bank site; that could cause the corresponding noise power to be higher, on average, which can be seen by comparing Figure 4.2a and b with Figure 4.5a and b.

The same strong intermittent noise that was present between 27 kHz and 30 kHz at Tanner-Cortes Bank when the source was close to the receivers existed at CPA here so the time window for the PSD in Figure 4.5c and d was half a second wide.

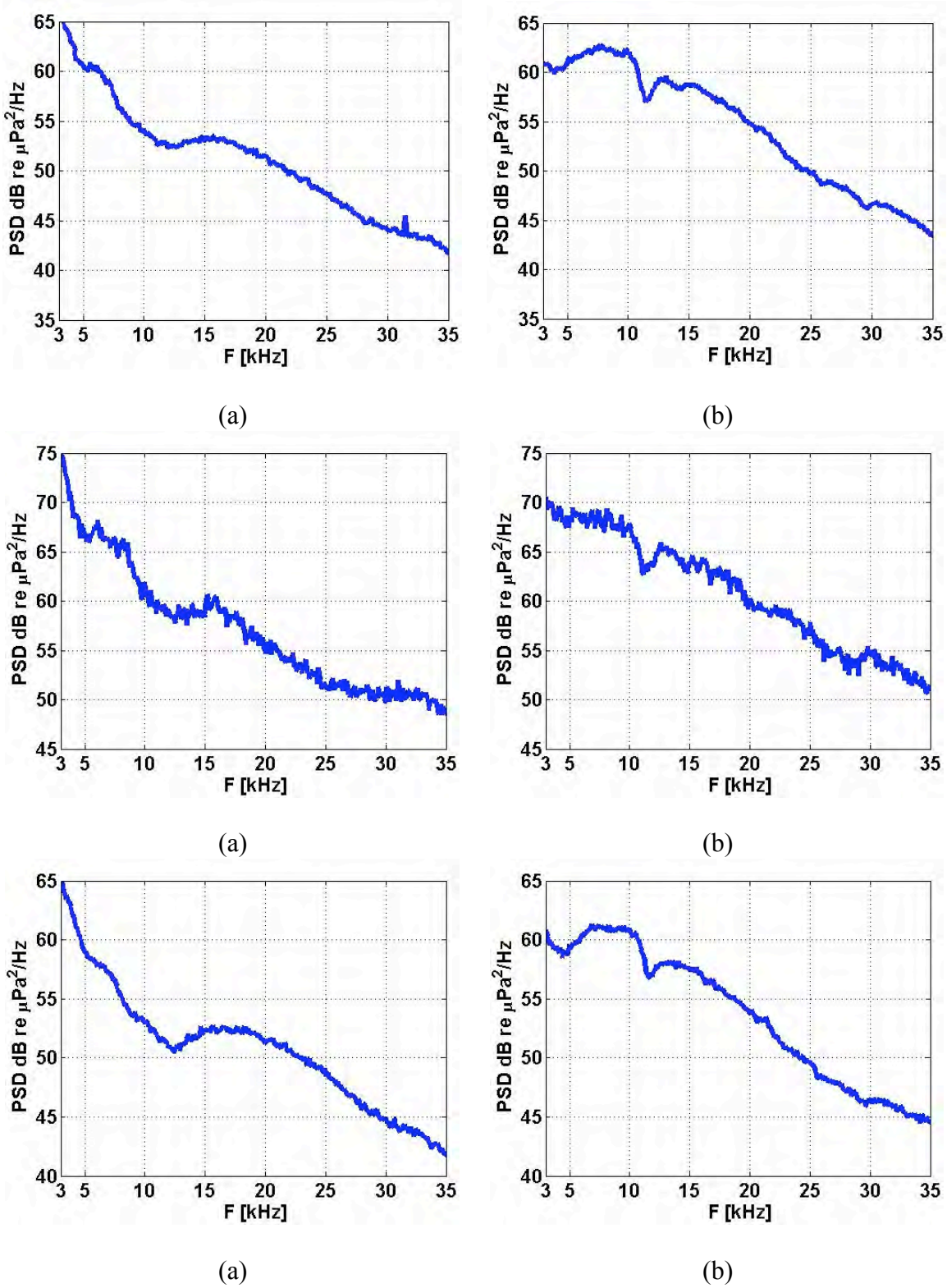

Figure 4.5 Noise PSD at China Point (Figure 1.2b, solid line); approximate range and hydrophone depth, respectively, are: (a) -3.5 km, 27 m; (b) -3.5 km, 61 m; (c) 300 m, 27 m; (d) 300 m, 61 m; (e) 3.5 km, 27 m; (f) 3.5 km, 61 m; negative range refers to the section before CPA.

Although the self noise at the reference hydrophone was not different than at the Tanner-Cortes Bank site, the radiated noise at the hydrophones differed due to the environment. A major environmental difference is that the mixed layer at this site was distinctively defined and sufficiently deep for the shallower receiver and the source to be found inside the layer (Chapter 3). Therefore the low-frequency energy that originated close to the sea surface was not channeled to deeper depths but was confined to the layer, causing higher NL at 27 m than at 61 m at frequencies below 5 kHz (Figure 4.5c and d).

Octave [kHz]	Depth [m]	r = -3.5 km	CPA	r = 3.5 km	Average [dB/oct]
3 - 6	27	-5	-9	-5	
	61	0	-2	0	
5 – 10	27	-5	-6	-7	
	61	1	-1	0	
10 – 20	27	-5	-5	-2	
	61	-8	-7	-7	
15 – 30	27	-15	-10	-7	
	61	-13	-9	-12	
Average	27	-7.5	-7.5	-5.25	-6.75
	61	-5	-4.75	-4.75	-4.83

Table 4.2 Average slope (dB/oct) of the noise spectra in Figure 4.5; negative range infers the section before CPA.

The noise spectrum in Figure 4.5e and f is very similar to the "quiet" section noise spectrum (Figure 4.5a and b), which implies that the machinery noise radiated from the ship either did not have a major impact on the background noise at ranges as long as 3.5 km, or spread more evenly around the ship when the medium featured upward and downward refraction, as opposed to the predominantly downward refracting Tanner-Cortes Bank site.

The NL was higher, around 5 dB (re 1 μPa^2/Hz) on average, at 61 m than at 27 m at frequencies above 5 kHz. It suggests that the main sources of noise in that part of the frequency band did not originate in the surface layer. In general, the slope of the noise spectrum at 27 m is steeper than at 61 m at this site (Table 4.2).

San Nicolas Basin Site

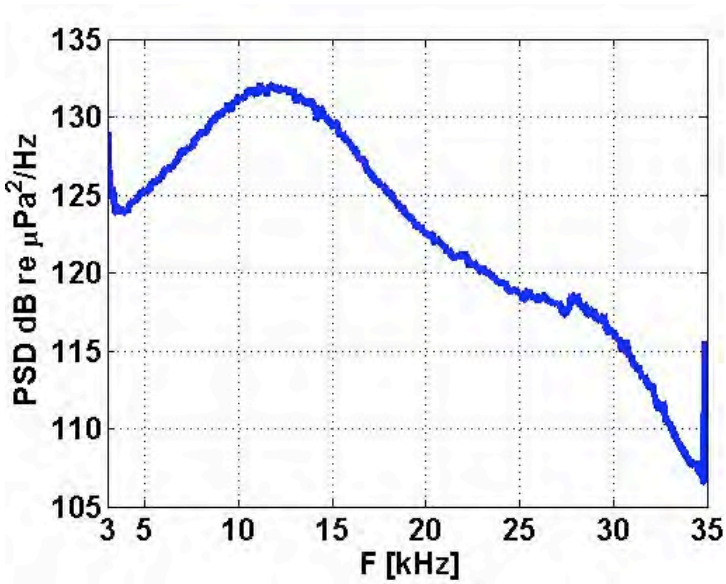

Figure 4.6 Noise PSD at the reference hydrophone (3 m away from the source), measured in San Nicolas Basin (Figure 1.2c, solid line). Conversion from voltage to pressure was done with the response from Figure 1.6.

The noise spectra in Figure 4.6 and Figure 4.1 are very different. The reference hydrophone depth changed with source depth, but the noise spectrum did not significantly change. This site has more distant boundaries than the shallow sites, so it may be that in shallow water the reference hydrophone was strongly impacted by reverberation.

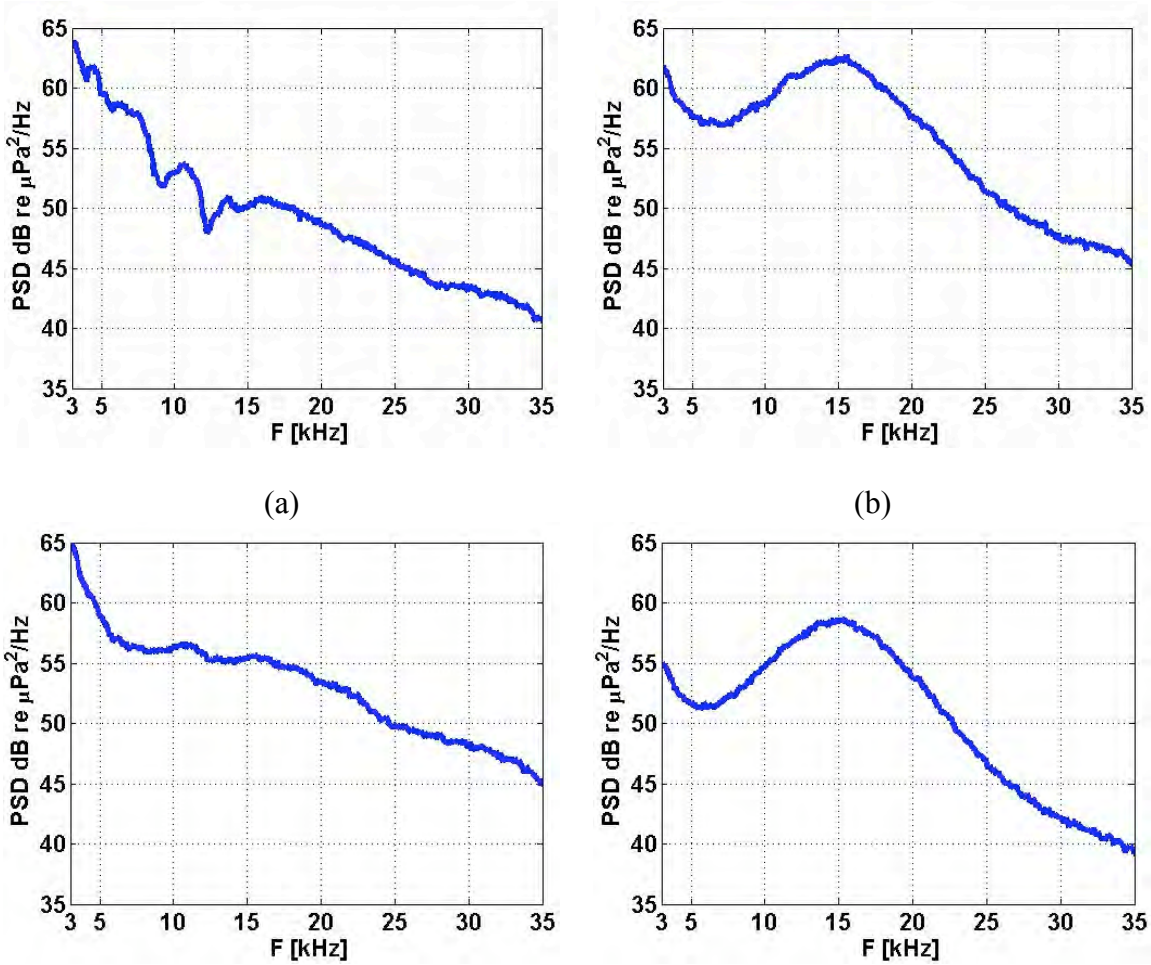

Figure 4.7 Noise PSD in San Nicolas Basin (Figure 1.2c solid line); approximate range and hydrophone depth, respectively, are: (a) 300 m, 27 m; (b) 300 m, 122 m; (e) 2 km, 27 m; (f) 2 km, 122 m.

In deep water, ambient noise is expected to be higher closer to the sea surface because of breaking waves and shipping [2] [30]. This is observed in Figure 4.7 at frequencies below 5 kHz; however NL in the deeper channel has a broad maximum at 15 kHz that is higher than its shallower counterpart. The noise spectrum at 61 m has a shape similar to that of the reference hydrophone noise spectrum, but the broad maximum is shifted in frequency from about 12 kHz at the reference hydrophone to 15 kHz at the receiving hydrophone, which could not be caused by Doppler shift (Chapter 2).

In general, the average slope of the noise spectrum at this site (Table 4.3) is somewhat shallower than at the shallow water sites (Table 4.1 and Table 4.2); nonetheless, the noise spectrum evaluated at the location south of China Point (Table 4.2) and the noise spectrum evaluated at this site have in common that the shallower receiver, which was likely to be in the mixed layer at both sites, has somewhat steeper slope than the deeper receiver at the corresponding site.

Octave [kHz]	Depth [m]	r = 300 m	r = 3.5 km	Average [dB/oct]
3 - 6	27	-5	-6	
	122	-4	-4	
5 – 10	27	-7	-4	
	122	1	4	
10 – 20	27	-4	-3	
	122	-1	-1	
15 – 30	27	-7	-7	
	122	-15	-17	
Average	27	-5.75	-5	-5.38
	122	-4.75	-4.5	-4.63

Table 4.3 Average slope (dB/oct) of the noise spectra in Figure 4.7.

Summary

The NL was elevated by the radiated noise from the ship, especially when the ship's propellers were facing the receivers. Frequencies between 3 kHz and 5 kHz were affected more than frequencies between 5 kHz and 30 kHz. In addition, frequencies lower than 5 kHz had higher NL at the receiver in the mixed layer than at the receiver below the mixed layer, whereas a deeper receiver would typically have higher NL at frequencies beyond 5 kHz. Spectra of the self-noise measured at the reference hydrophone in deep

and shallow water had increasing and decreasing slope, respectively; the difference was probably caused by excessive shallow-water reverberation. When a distinct mixed layer existed, the noise spectrum at the receiver in the mixed layer would have a steeper slope than the noise spectrum at the receiver below the mixed layer, whereas a grossly downward refracting medium would impose a steeper slope on the noise spectrum of the deeper receiver. Based on a set of sixteen PSD estimations, over 5 s and 0.5 s time windows, at 27 m, 61 m and 122 m, in shallow and deep water, the average slope of the noise spectrum was between -4.6 dB/oct and -6.8 dB/oct, which are in fairly good agreement with the common average of -5.0 dB/oct to -6.0 dB/oct [26]. Because of the negative slope of the noise spectrum, the 30 kHz pulses yielded substantially higher SNR than the 3 kHz pulses that had approximately the same SL.

CHAPTER 5

PULSE EXTRACTION

Urick [2] classifies fluctuations of sound into deterministic and stochastic, the former being the seasonal and diurnal changes in TL, moving receiver etc. while some of the causes of the latter would be thermal microstructure, internal waves, and multipath.

Figure 5.1 shows the envelopes of a sequence of six consecutive 10 kHz pulses, for both moored hydrophones at Tanner–Cortes Bank site (solid line in Figure 1.2a). With the 11.6 s interval between tones at a given frequency, and assuming an average speed of the ship around 2.5 m/s, 6 pings yield a travel path of 6×11.6×2.5=174 m. We can see that within a 174 m difference in range, the direct-path pressure magnitude fluctuates between 0 and 0.5 Pa.

A goal is to detect a pulse that went through as few boundary reflections as possible so that phase distortion is minimized. Therefore the focus is on extraction of the earliest, not necessarily the strongest arrival.

As illustrated in Figure 5.2, for a transmitted signal x(n), if the communication channel is assigned a linear model with the channel impulse response h(n), n=0..N-1 and noise n(n). The received signal is given by:

$$y(n) = \sum_{m=0}^{N-1} x(m)h(n-m) + n(n)$$

Equation 5.1

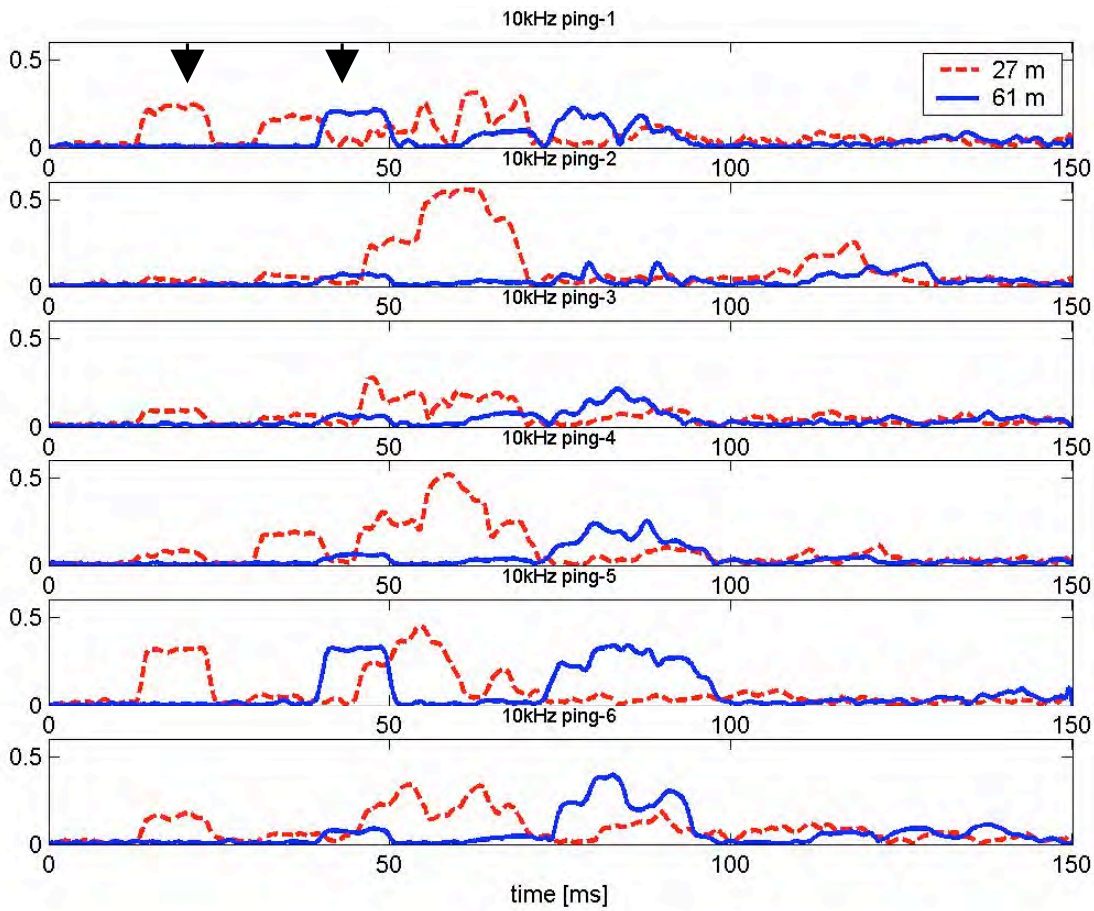

Figure 5.1 Pressure envelopes (units of Pa) of the 10 kHz pulses, including clutter, from 6 consecutive pings from measurements made at the Tanner-Cortes Bank site (range ≅ 2 km). Depths of the source and the receiving hydrophones were respectively about 40 m, 27 m, and 61 m. The arrows point to the first arrivals of the signals at the two different receiver depths.

The impulse response of the matched filter is obtained by inversion of the order of the samples of the transmitted signal [19]. Matched filtering of the signal at the output of the channel generates a correlation function m(n):

$$m(n) = \sum_{m=0}^{M-1} y(m) x_h (M - n - m)$$

Equation 5.2

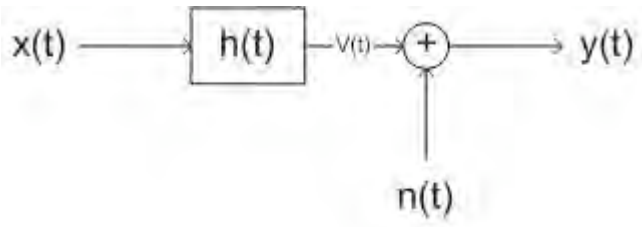

Figure 5.2 Illustration of Equation 5.1.

where x_h is a transmit signal replica, eventually updated with available parameters of the communication channel, such as Doppler shift. It is shown in Chapter 2 that the acquired spectral resolution was looser than the expected Doppler shift (Equation 2.4 and Equation 2.5); therefore, the Doppler Effect was not taken into account for the matched filter design.

Because of the additional loss at the boundaries, the reflected acoustic waves are expected to have lower magnitude than the original. On the other hand, in a time varying multipath environment a transmitted sinusoid will appear at the receiver as a narrowband random process [20], thereby allowing multipath components to exceed in energy the principal arrival. This is because the signal will travel along different paths in reaching the receiver. The net effect is to cause constructive or destructive interference, resulting in an unpredictable amplitude and phase. Furthermore, the propagation characteristics of the channel will change in time, due to its inherent non-stationarity, and because neither transmitter nor receiver is absolutely static.

Figure 5.3 shows the envelopes of the signals and background noise from the noisiest part of the “solid line” track in Figure 1.2a. Sections between 90 ms and 100 ms are the time windows of the earliest arrivals at the receivers.

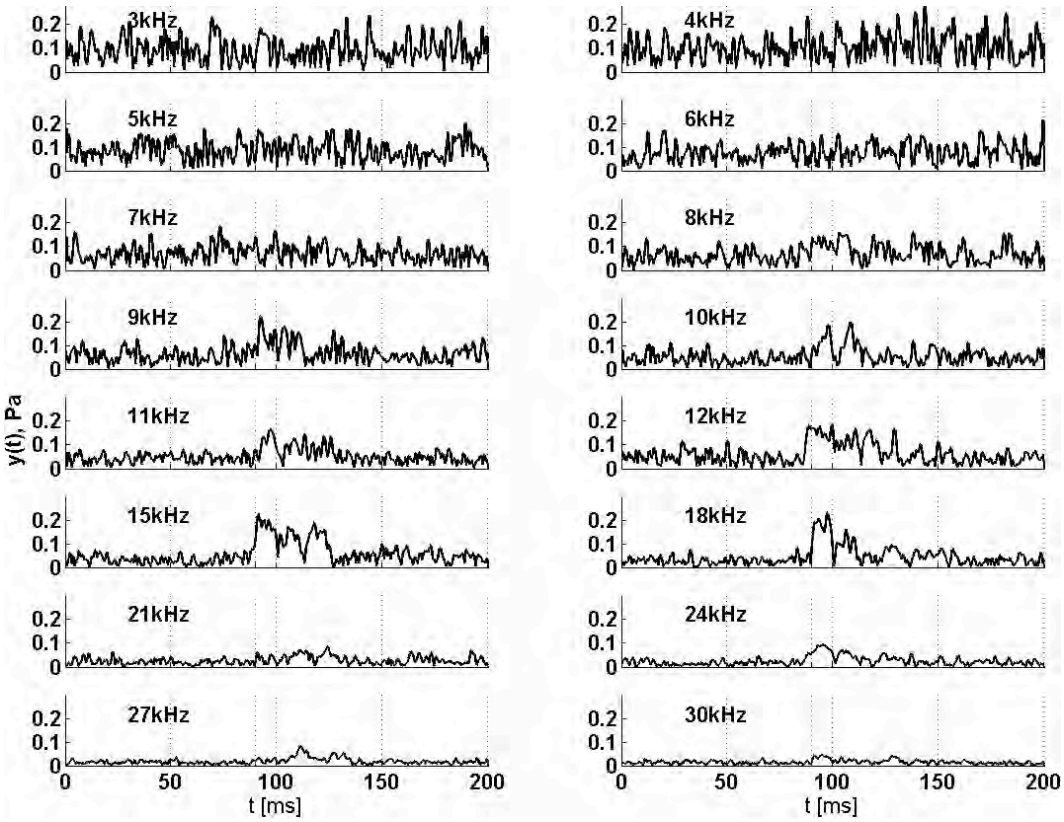

Figure 5.3 Envelopes of the signals and background noise at the transmitted frequencies. The snapshots correspond to the CPA point of "solid line" track in Figure 1.2a (range ≈ 200 m); hydrophone depth 27 m. Estimated first arrival time window: 90 ms – 100 ms.

For each transmitted CW pulse of duration τ the auto-correlation function ideally is triangularly shaped and 2τ long [21]. Since matched filter resembles an auto-correlation up to a multiplicative factor, that shape and duration is expected in the correlation function defined in Equation 5.2. In Figure 5.4 this shape can be recognized at frequencies of 8 kHz and higher. The lower frequency signals are buried in noise because of the strong ship radiated noise (Figure 4.3). When multipath arrivals are close in time to the direct path arrival, which is the case in shallow water, time separation can be shorter than the pulse length τ causing overlap between the triangular functions resulting from correlating the signal replica with the direct-path arrival and a multipath arrival. They can

be entirely separated as long as the peaks of the triangles are more than a pulse length apart.

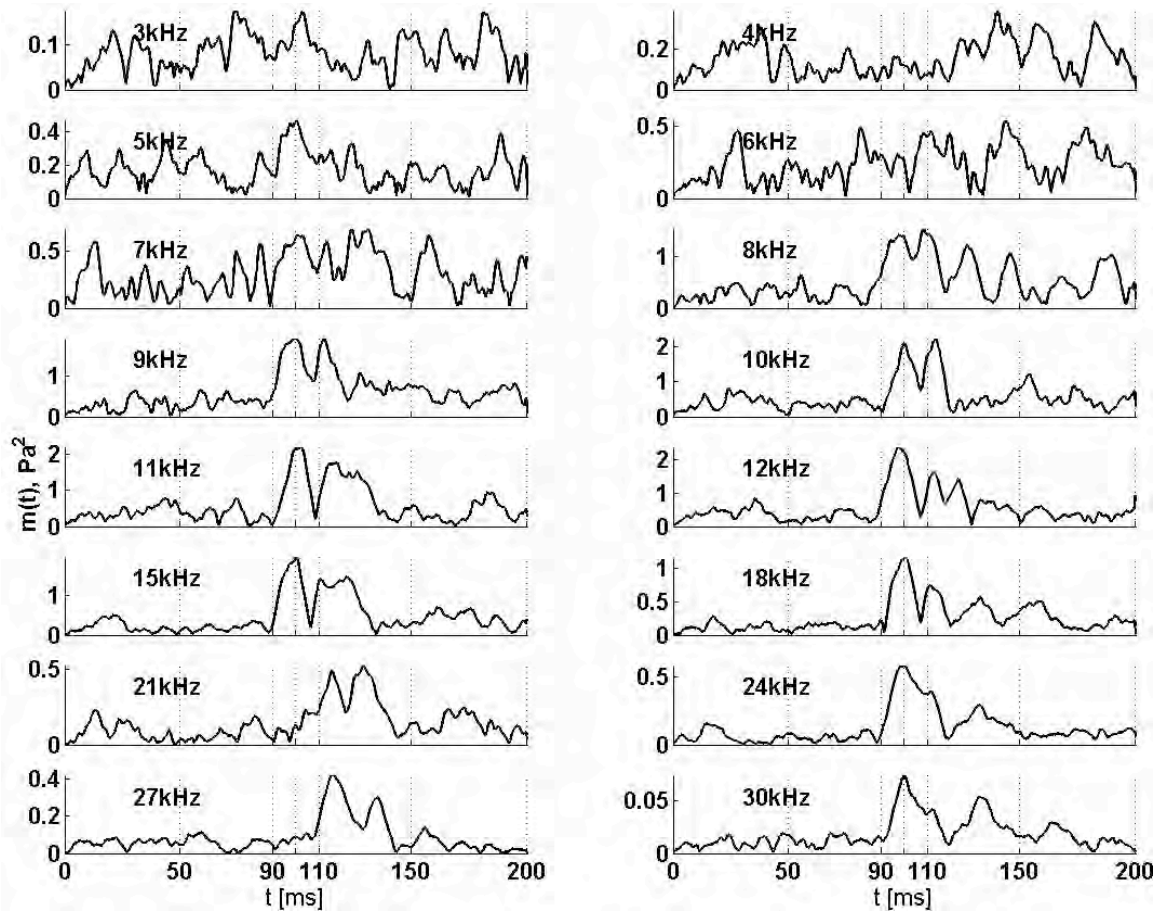

Figure 5.4 Envelopes of the correlation functions for the snapshots from Figure 5.3. The vertical scales are not unified for display purposes.

Figure 5.5 shows phase snapshots of the signals corresponding to the envelopes in Figure 5.3. Phase varies with time in a random manner for the signals below 8 kHz, because of excessive noise. At higher frequencies, where the signal level was above the NL, phase varies with time inside the pulse time window as a result of the beam intersections, as explained in Chapter 3. For instance, the window of the 21 kHz pulse

contains a phase inversion between 90 and 100 ms that indicates a surface reflection. The actual phase inversion should be distinguished from the phase wrapping, which happens when the phase is very close to 180°, because it can only be resolved between -180° and 180°.

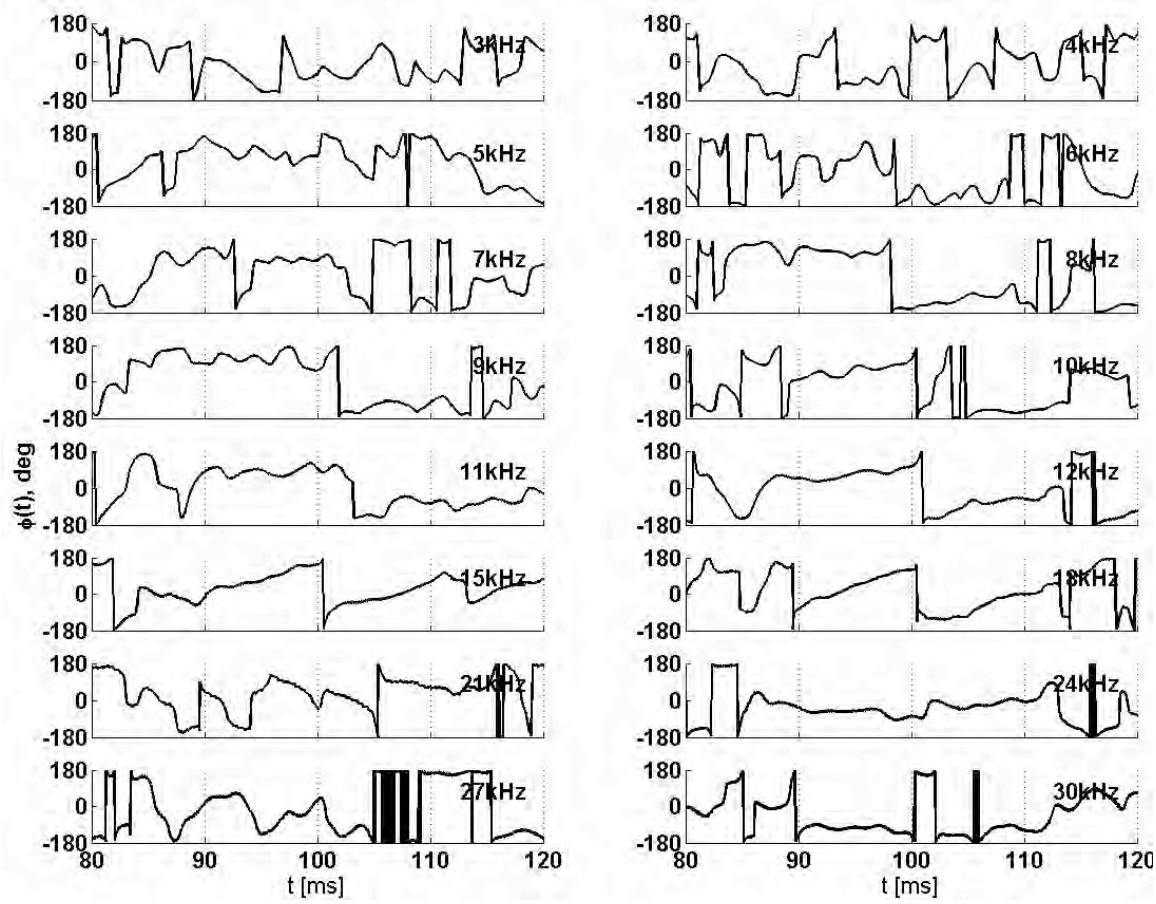

Figure 5.5 Phase snapshots of the signals corresponding to the envelopes in Figure 5.3.

If the maximum of the correlation function, defined in Equation 5.2, were used as a pointer to the expected principal arrival for the signal in Figure 5.6, it would recognize the reflection with the maximum magnitude as the most probable direct-path signal, which is incorrect in this example.

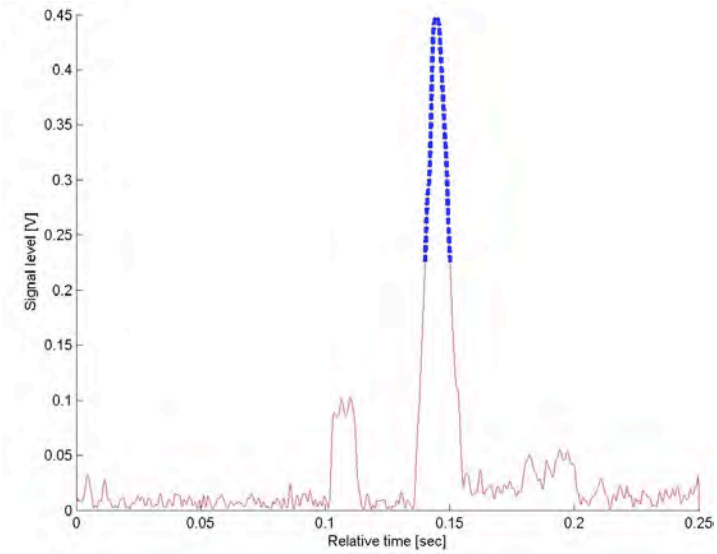

Figure 5.6 Envelope of a received signal with a strong multipath component. The direct-path arrival starts at 0.1 s and the taller peak starting at 0.13 s is due to multipath. The dashed line is the envelope of the signal detected by matched filtering.

When a transmitted sequence is a series of Continuous Wave (CW) pulses at N different frequencies, uniformly separated in time, frequency diversity is attainable. Since multipath is a relatively random phenomenon, a regular pattern would not be expected in the time difference between the direct-path arrivals and reflections at N different frequencies (Figure 5.4). In order to overcome the problem of overwhelming interference, two different algorithms were devised and implemented: one based on the sum of the rectified correlation functions of the received signals, and the other based on a least square time constraint applied to the arrival times in a sequence. Both of these methods try to introduce a processing gain by taking advantage of the frequency diversity embedded in the transmit sequence.

Summation of the Rectified Correlation Functions

Due to the complex sound propagation along a spread of beams [10], multipath arrivals were often much stronger than the direct-path arrivals. An algorithm was developed to search the correlation functions for the global maximum, and for preceding local maxima that might correspond to the direct-path arrivals. The term "correlation function" is used for the result of correlating the output data of the communication channel with a replica of the transmitted signal, which is equivalent to the output of matched filtering [19]. The rationale is that (1) detection results from one of the applied matched filters may help signal detection at other frequencies, for which the direct-path signal might have largely faded away, and/or the signal-to-noise ratio is below the DT because of the bandwidth limitations of both the source transducer and the hydrophone. Hence, by combining the correlation functions for the 16 frequencies, one could take advantage of stronger signals at some frequencies to compensate for the limitations at others. And (2), the complexity of the algorithm should decrease by combining the correlation functions into one generic sequence, and then searching one instead of N different sequences.

The algorithm starts with the broadband sequence y(m), which is digitized and recorded at the receiver, then band-pass filtered (impulse responses h_n) at each of the N transmitted frequencies:

$$x_n(m) = y(m) * h_n(m), n = 1,..N$$

Equation 5.3

Symbol '$*$' stands for convolution [21]. Next, outputs from the N filters are matched with a time-inverted replica h_M of the test signal, containing M samples, at the corresponding frequency [19]:

$$r_n(m) = x_n(m) * h_M^n(m), n = 1,...N$$

Equation 5.4

$$\text{with } h_M^n(m) = x_n(M-1-m), m = 0,...M-1$$

Equation 5.5

The resulting N correlation functions (r_n) are then delayed *(N-n)T* time units, where *T* is the transmission time difference between two consecutive CW pulses (100 ms). This operation aligns in time all the correlation functions of one transmission sequence, before rectifying and summing them into a global correlation function r_s:

$$r_s(q) = \sum_{n=1}^{N} abs(r_n(q-(N-n)T \times f_s)), q = 1,...Q$$

Equation 5.6

with sampling frequency f_s, and for a received sequence of length Q. An example of such a global correlation function is shown in Figure 5.7.

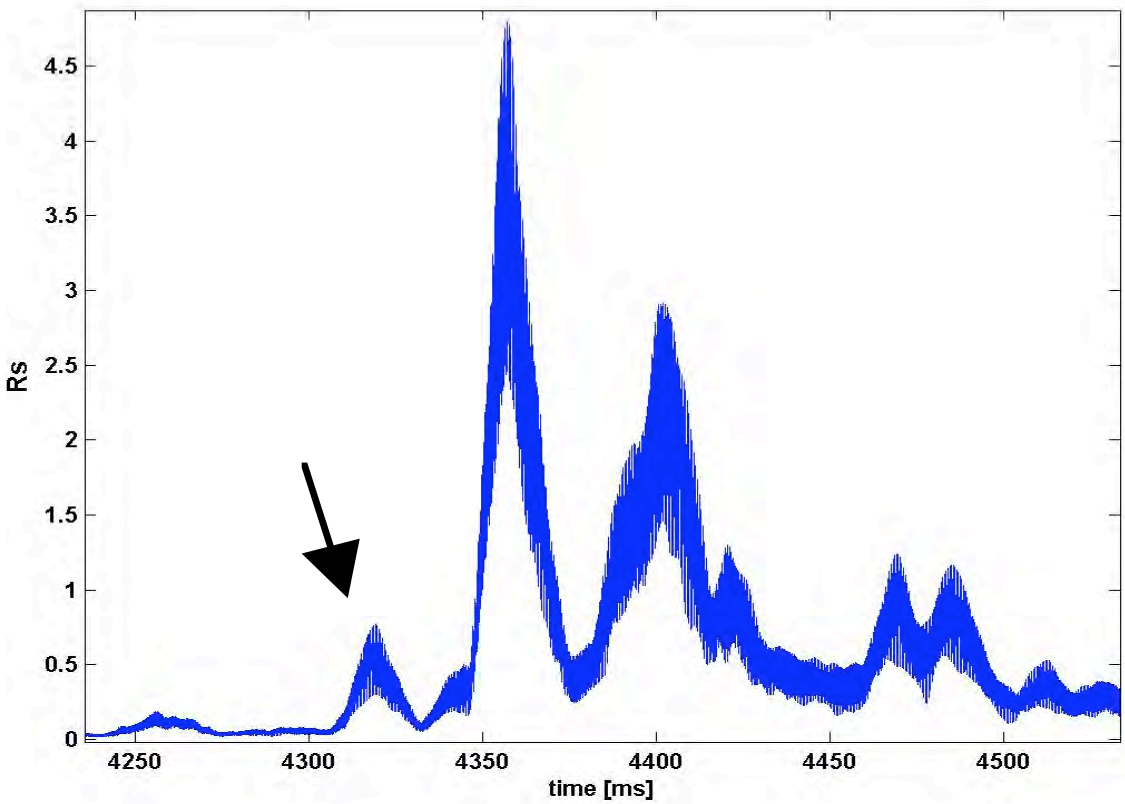

Figure 5.7 Sum of 16 rectified correlation functions received for one transmission sequence. The arrow points to the detected direct path arrival(s).

The algorithm searches the samples of the envelope of r_s, in the vicinity of the peak value, for a local maximum that might belong to the direct-path arrival. Since the envelope of the auto-correlation of a 10 ms CW pulse is a triangle spanning 20 ms, matches between segments of the sequence r_s, spanning ±10 ms around each detected local maximum, and an auto-correlation template are evaluated through a cost function (Equation 5.7). The template is generated by the same set of operations leading to r_s, but they are applied to the known transmitted signal. The template is therefore the sum of the rectified auto-correlation of each transmitted CW pulse. This function is illustrated in Figure 5.8a.

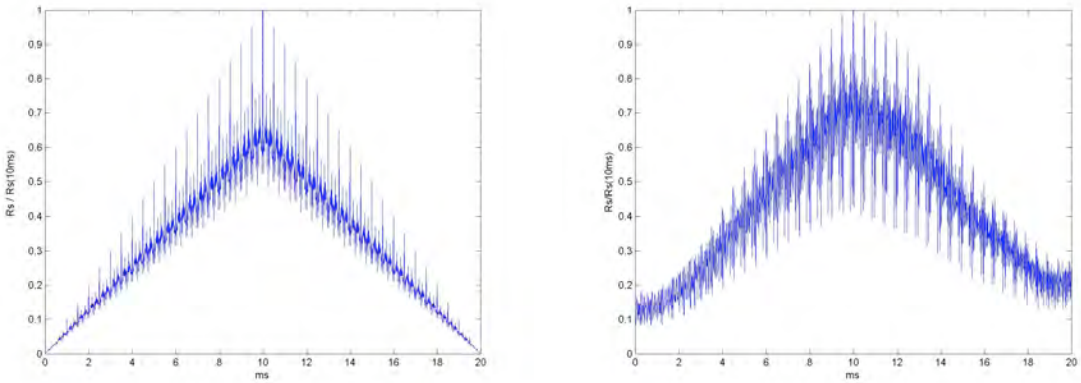

(a) (b)

Figure 5.8 Summation of the rectified correlation functions: a) the template b) a real signal sample from Figure 5.7.

If ***I*** local maxima higher than the DT are found, a cost function *c(i)* is used to select one of them:

$$c(i) = \sum_{k=-K}^{K} \left| \frac{r_s^{template}(k) - r_s^{measured}(p(i)-k)}{r_s^{template}(k)} \right| \quad i = 0, \ldots I-1$$

Equation 5.7

K is the number of samples equivalent to the duration (τ) of each CW pulse (K=integer(τ/f_S). For τ=10 ms and f_S=100 kHz, K=1000. A sample ***p*** will be selected as the end of the direct-path signal arrival, if it is the earliest of all the samples for which the cost function is below the threshold:

$$p_{dpa} = \min\left(p(i) \middle| c(i) < \text{threshold}\right)$$

Equation 5.8

For example, p_{dpa} was about 4320 ms in Figure 5.7. If none of the local maxima satisfies the above criteria (Equation 5.7, Equation 5.8), the global maximum is retained as the direct-path arrival. The time of arrival for each CW pulse is then estimated by subtracting the corresponding time shift from (Equation 5.5):

$$p_n = p_{dpa} - (N - n)T \times f_s, \; n = 1,...N$$

Equation 5.9

The time delay between the received pulses in one 'ping' varies with the ship's speed and the geometry of the problem, thereby offsetting the clocks of the correlation functions. With 1.6 seconds between the first and the last transmitted pulse, the biggest time offset, to first approximation, will be:

$$\Delta t = 1.6 \times v_s / c = 2.7\,\text{ms}$$

Equation 5.10

For this time offset, the time window (10 ms) of a detected pulse could be shifted around in order to extract the central segment of the pulse.

This algorithm was employed in pulse extraction from the shallow water data because of conveniently short time differences between arrivals.

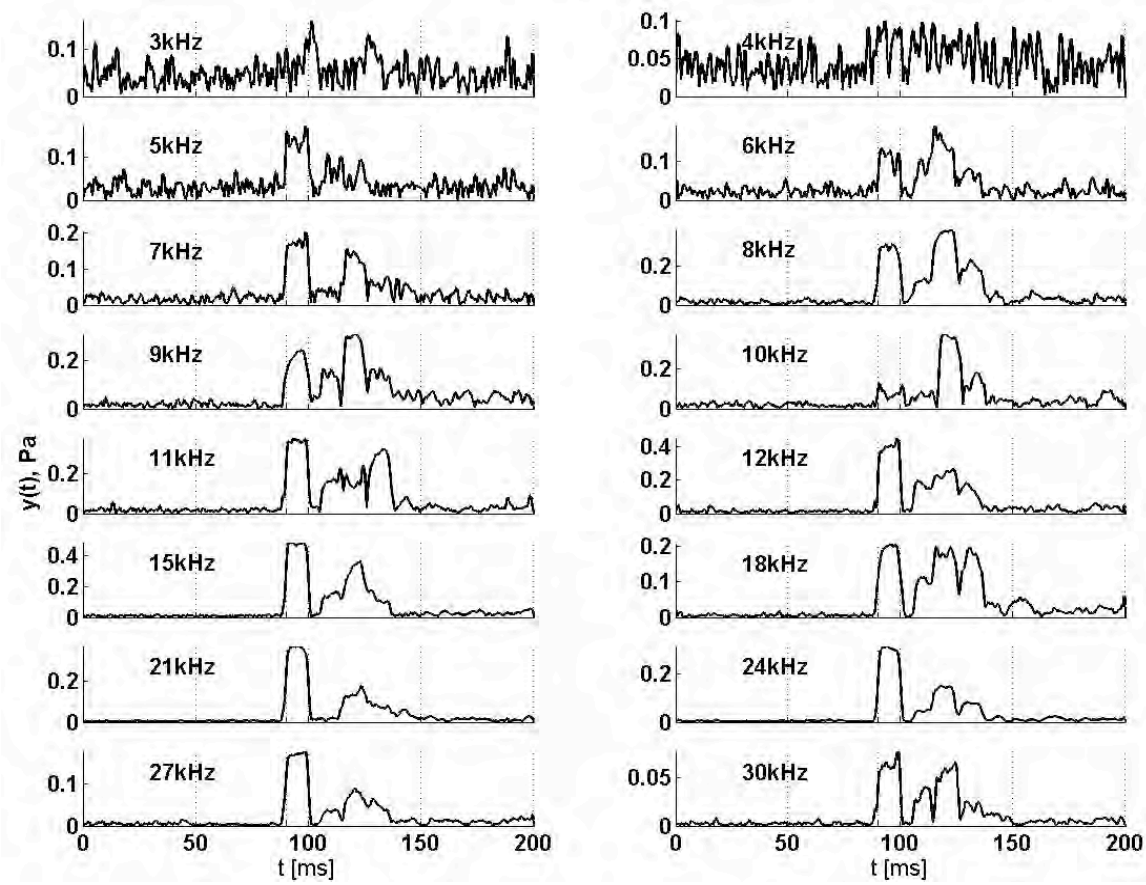

Figure 5.9 Projected pulse envelopes at the 16 frequencies (range ≈ 1 km, before CPA), measured at Cortes-Tanner Bank (Figure 1.2a solid line), for hydrophone depth of 61 m. First arrival time window: 90 ms – 100 ms; the vertical scales are not unified for display purposes.

Figure 5.9 represents an example of pulses detected using this algorithm. In terms of direct-path arrival, the signals at 6, 8, 9 and particularly 10 kHz exhibit envelope distortions that indicate interference.

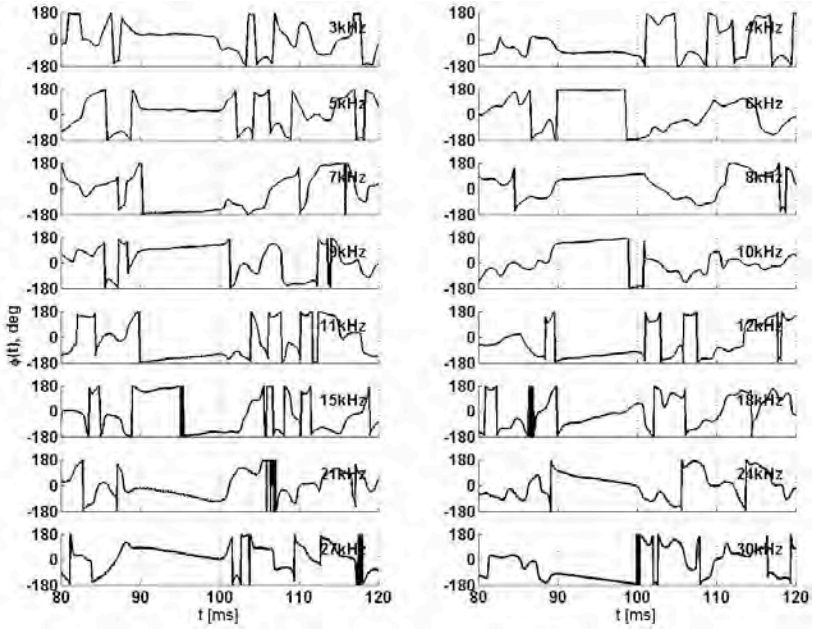

(a)

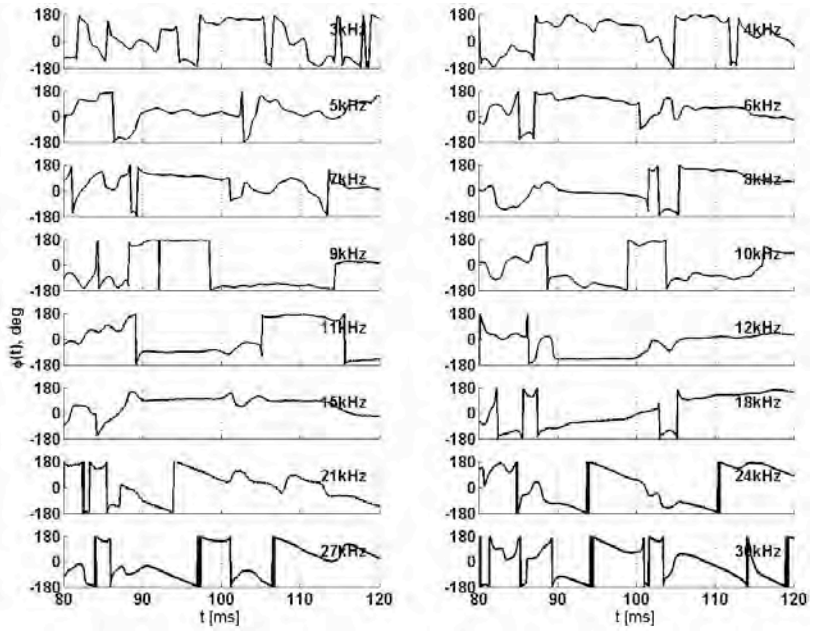

(b)

Figure 5.10 Phases that correspond to the envelope snapshots in Figure 5.9. First arrival time window: 90 ms – 100 ms; Recorded at: (a) Reference hydrophone. (b) Sonobuoy hydrophone.

The tilted phases of the reference hydrophone signals in Figure 5.10a, especially at frequencies higher than 10 kHz, might be artifacts of sparse sampling. A major difference between a signal phase at the reference hydrophone and at the receiver is that the former is distorted by propagation through water only, whereas the latter could contain interference inside the pulse interval. The nonlinear effect caused by dependence of sound speed on pressure, as explained in Chapter 1, that induces higher harmonics of the fundamental is common for both sides and it does not seem to result in significant phase distortions.

The direct-wave pulses with carrier frequencies from 3 kHz to 6 kHz in Figure 5.10b exhibit some distortion that could be noise related. The phases of the 8 kHz and 9 kHz signals do not look substantially different from the phases of the reference hydrophone signals, aside from inevitable phase shifts. The 10 kHz pulse does have somewhat distorted and shifted phase, relative to the reference hydrophone, that could be caused by strong interference.

The phases fluctuate as a result of merging of a number of rays. Excluding the inevitable phase wrapping, there are some abrupt changes in the phases that indicate surface reflection contribution. Although a phase inversion mechanism takes place at the surface reflection, the resulting phase change at the receiver does not have to be 180° because of the compensation by the other intersecting beams. Notice that the 27 kHz and 30 kHz pulses, although driven at lower intensity due to source transducer limitation (Figure 1.5a), had outstanding SNR and insignificant phase distortion in the direct-path pulse interval, whereas the much stronger 10 kHz signal intensity yielded severe fading, probably caused by volume or surface scattered interference.

Least Square Time Constraint

A method has been devised that detects each CW pulse independently, and then applies a tone-to-tone time constraint to get a more accurate estimate of the direct-path arrival times of the pulses, and to help distinguish direct arrivals from reflections. The algorithm contains the following steps applied to each received transmission sequence:

1) Band-pass filtering centered at each of the transmitted frequencies. The bandwidth of each band-pass filter should be at least as wide as the associated Doppler shift Δf (Hz), as explained in Chapter 2.

2) Match-filter each of the N outputs from step 1, and retain the time of the maximum amplitude. Under an assumption that the signal envelope is Rayleigh distributed, the Quadrature or Incoherent Matched Filter is derived as an optimal detector with respect to SNR [20]. The Rayleigh distributed envelope is a theoretical model that comes as a result of the WGN channel. Although it is shown in Chapter 4 that noise is not white Gaussian over a wide frequency band, WGN is a reasonable approximation for narrowband signals since the noise is nearly white within the pre-filtered signal bandwidth. Nonetheless, the previously described implementation of the matched filter as a convolution was found simpler to implement and more convenient for the purpose of pulse extraction.

3) Find the largest subset of the N time points from step 2 whose least-square fit to a straight line has a 100 ms gradient (time difference between the tones) with less than Δt uncertainty. The uncertainty factor should be chosen not to be smaller than the biggest pulse-to-pulse time offset.

4) Set a confidence interval around the least square fit values from step 3 for every point. Check whether the points belong to the designated interval. Every point found outside the boundaries is deemed an outlier.

5) Repeat step 2 for each outlier in step 4, restricting the filtering to later or earlier times toward the least square estimate for that tone.

6) Repeat steps 3 to 5 until all the points are within the region of confidence specified by Δt.

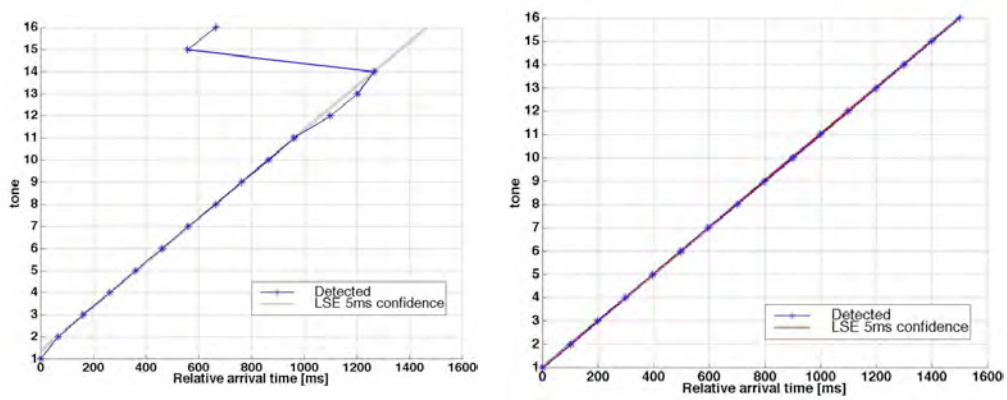

(a) **(b)**

Figure 5.11 An example of a successful signal detection completed after two iterations. The line with symbols represents the times. The parallel straight lines delimit the 5ms confidence region of the least square fit.

Figure 5.11 shows an example of the iterations of this algorithm applied to a 16 pulse transmission sequence with 100 ms pulse-to-pulse period. After the initial iteration (Figure 5.11a), 11 points of detected arrival times are in good agreement with the 100 ms tone-to-tone time difference. There is another group of two points about 100 ms apart, tones 15 and 16, which belong to the harmonics of the arrivals at 9 kHz and 10 kHz (Figure 1.7). Tones 12 and 13 are also on a line whose gradient is around 100ms. These

two points probably belong to multipath arrivals. In step 3 of the algorithm, the biggest group is chosen for the direct-path arrivals.

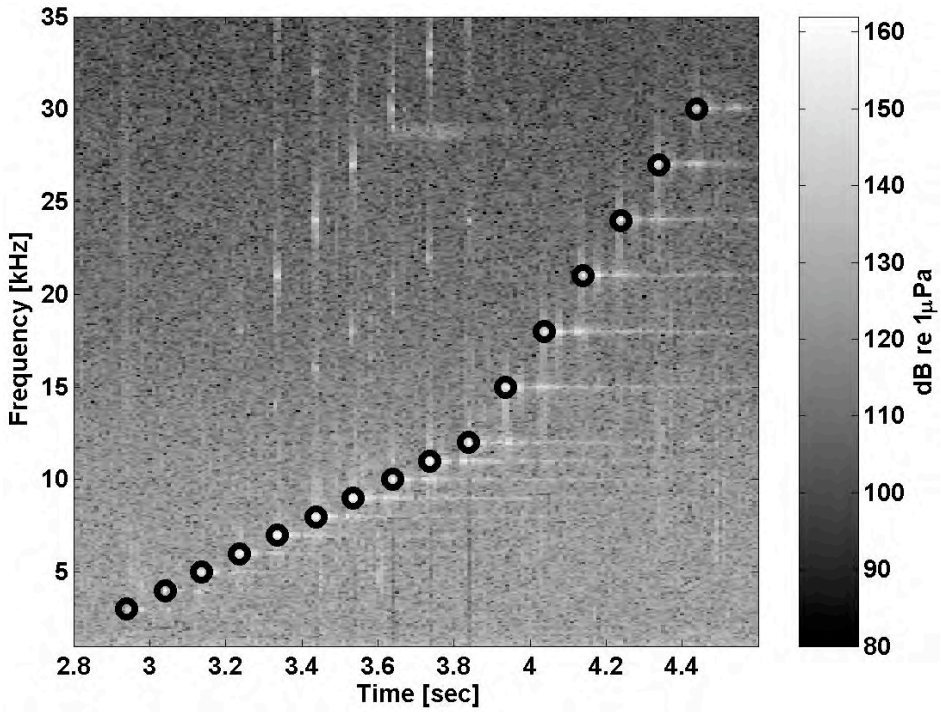

Figure 5.12 Spectrogram of the time series received at one hydrophone for one transmission sequence (range ≅ 2 km). Circles identify direct-path arrivals, and trailing signals represent multipath arrivals.

At the second iteration, step 4 proceeds forward from the current estimated arrival times for tones 15 and 16, and backward for tones 12 and 13. A solution is reached when all the pulses are detected within a 5 ms tolerance interval (Figure 5.11b). The positions of the circles in Figure 5.12 correspond to the final solution in this example. If the number of iterations exceeds 2 (a heuristically adopted threshold based on examples such as this one) the outliers are likely to be caused by completely faded direct-path arrivals so the algorithm can be stopped by correcting the outlying points with the corresponding least square fit value.

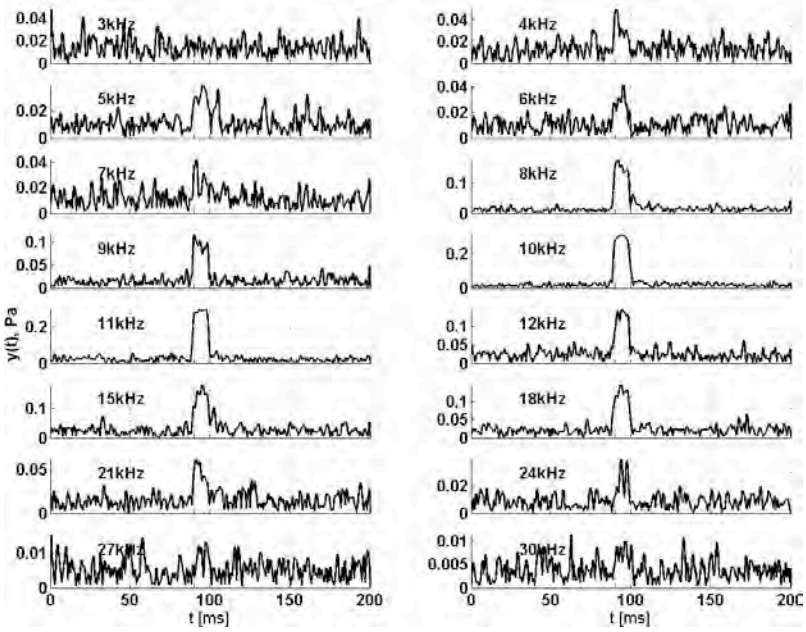

(a)

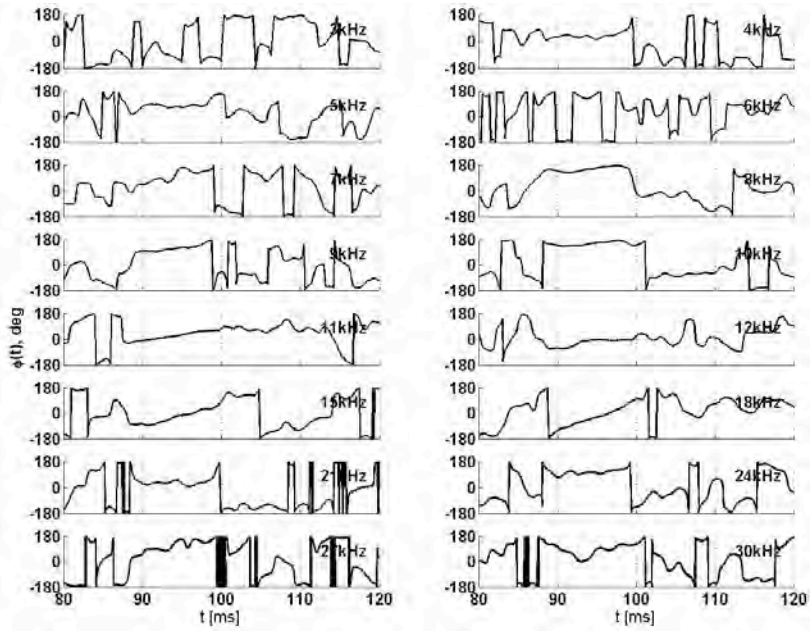

(b)

Figure 5.13 Pulses transmitted at the 16 frequencies (range ≈ 1 km), measured at the San Nicolas Basin site (Figure 1.2c solid line), for hydrophone depth of 122 m; source depth 13 m; first arrival time window: 90 ms – 100 ms. (a) Envelopes; the vertical scales are not unified for display purposes (b) Phases.

An advantage of this algorithm over the summation of the rectified correlation functions is the self-correcting time offset feature which makes it more suitable for coherent detection because pulse ends are more accurately located, hence providing less noisy phase information. It is somewhat more computationally demanding for being iterative. In the case of flat fading, such as duct leakage (Figure 3.13b) in the kHz band, this algorithm would not converge to the earliest arrival without additional iterations. Nonetheless, it was employed in pulse extraction from the deep water data because of conveniently longer time differences between the first arrival and the following arrivals (Figure 1.8 and Figure 3.13) which allowed focusing on the isolated first arrivals.

An example of pulses detected using this algorithm is shown in Figure 5.13. Notice that the 4 kHz pulse does not have a substantial SNR; however its phase seems reasonably stable. The average noise spectrum slope at 122 m in San Nicolas Basin (Table 4.3) was shallower than at any other site/depth of the experiment; hence NL was higher at frequencies beyond 15 kHz; the phases of the signals at frequencies higher than 15 kHz seem to be more sensitive to noise.

Summary

Due to various sources of sound fluctuations, a multipath arrival could have higher intensity than a direct-path arrival, which would cause the matched filter to falsely detect a multipath arrival as a direct-path arrival. Two methods were devised and applied for pulse extraction from background noise and multipath. They improved the accuracy of the evaluation of direct-path signal intensity and phase. It was shown that the direct-path arrivals of the pulses at frequencies that were at the top of the frequency band used,

27 kHz and 30 kHz, although driven at lower intensity due to a source transducer limitation, could have lower phase distortion than signals at frequencies with significantly higher SL. In high noise background, the frequencies higher than 15 kHz were more sensitive to noise.

CHAPTER 6

TRANSMISSION LOSS

In the simplest form, according to Urick [2], propagation loss can be calculated as:

$$TL[dB] = 10\log_{10}\left(\frac{I_0}{I_1}\right)$$

Equation 6.1

I_0 and I_1 stand for sound intensities 1 m away from an omni-directional projector and at the hydrophone, respectively. Equation 6.1 is very convenient for calculating TL based on measurements. As I_0 and I_1 are time average values, for a CW source the averaging time should be long enough to include all the effects of fluctuation in transmission [2]. Each shallow water environment has its own physical properties that make TL specifically complicated to estimate because of signal fading and multipath.

When a signal is transmitted into a free field by an omni-directional source, the transmitted energy spreads around along an infinite number of beams. The beams that actually arrive at the receiver belong to various groups of beams: direct and refracted, surface or bottom reflected, volume scattered or object reflected beams [2]. All the beams that do not belong to direct or refracted paths can be classified as multipath. Adequate time resolution is required for direct path and multipath to be completely separated. The time resolution of a CW pulse of duration τ is simply the effective pulse duration (τ_e)

which is defined, with respect to the 3 dB bandwidth (W) given in Equation 2.5, as $\tau_e = W^{-1} = \tau/0.88$.

In shallow water, where the boundaries are close to each other relative to the horizontal range of the measurement, surface and bottom reflections can overlap with the non reflected signal at the receiver. The algorithms described in Chapter 5 were employed in order to estimate the position of the effective pulse duration window in a data subset. The acoustic intensity of the signal extracted from that window is assumed to have the lowest boundary interference of all the arrivals detectable under a given DT.

A brief description of the actual TL calculation follows from Equation 6.1. Assuming far field conditions, which implies plane waves, at sound speed c and water density ρ, the root mean square (RMS) acoustic intensity is [16]:

$$I = \frac{p^2}{\rho c}$$

Equation 6.2

where p represents the RMS acoustic pressure of a CW signal. Although ρ and c change with depth, their influence on the ratio of the source and receiver acoustic intensities is not significant compared to the overall acoustic field attenuation process determined by spreading and absorption [16]. Therefore TL can be calculated as a function of the ratio of RMS values of the acoustic pressures p_0 and p_1 that correspond to the sound intensities defined in Equation 6.1:

$$TL[dB] = 20\log_{10}\left(\frac{p_0}{p_1}\right)$$

Equation 6.3

In order to estimate signal and noise acoustic pressure for the TL calculations, a simple RMS operation was applied over a number of samples N corresponding to the duration of one pulse:

$$p = \sqrt{\frac{1}{N}\sum_{n=1}^{N} p_n^2}$$

Equation 6.4

For a 10 ms pulse with 100 kHz sampling there are N = 1000 points per pulse. Coefficients p_n are the sample pressure magnitudes of the signal. Before these coefficients were calculated, band-pass filtering around the signal was performed, as described in Chapter 2. Since the power of a continuous wave of amplitude A is $S_0=A^2/2$, a smoothing filter could be applied after band-pass filtering to compute the signal power as half the squared envelope average. Nevertheless Equation 6.4 should provide a signal power estimation that is less sensitive to the computational limits caused by signal transience, and less computationally intensive because it does not include additional filtering.

In order to obtain a proper evaluation of the signal propagation conditions, the detected pulses should be screened with respect to the present noise masking level (NL+DT). In a theoretical or semi theoretical analysis, as provided by Ferla and Porter

[5], NL can be assumed to be constant and the DT can be determined based on the expected detection/false-alarm probability. As shown in Chapter 4 the NL was range and depth dependent during the experiments, mainly because of the impact of the radiated noise that originated from the ship that was towing the source transducer. Therefore the SPL had to be compared to the most current NL.

The DT was set to 6 dB above the average noise power computed in each frequency band over a 10 ms time window, starting 2 s prior to each transmission sequence. This time offset was necessary to avoid the ripples (Chapter 2) and higher harmonics of the preceding pulses. In choosing a proper DT under the given circumstances, a simple "rule-of-thumb" can be applied: if the total measured signal RMS pressure is p_{S+N}, then the condition for signal to stand out of the noise masking level ($p_{SS}>p_{NN}$) can be, approximately, expressed as:

$$p_{S+N} > 2p_{NN}$$

Equation 6.5

where p_{S+N} and p_{NN} represent the RMS value of the signal-plus-noise acoustic pressure, and noise only pressure, respectively. Finally, the DT that the output values are screened by is:

$$20\log_{10}\left(\frac{p_{S+N}}{p_{NN}}\right) > DT = 6dB$$

Equation 6.6

At each ping, the direct-path TL between the source transducer and the two vertically displaced hydrophones was first estimated by taking the ratio of their respective received sound intensities for I_0 and $I_{1,2}$ in Equation 6.1, with correction of $20\log_{10}(3)$ because the reference hydrophone was 3 m away from the source transducer. Unfortunately, some sections of the final TL curves were inconsistent at the higher frequencies (18 – 30 kHz) because the reference hydrophone signals were corrupted in this part of the frequency band. According to an observation noted in the logs, a probable reason was cross-talk at or near frequency modulation (FM) frequencies of the radio link used in transmission of the signals from the sonobuoys to the ship. It was observed in the post-event analysis that in some cases the 18 kHz pulse saturated the reference hydrophone by exceeding its dynamic range, which led to a highly unstable, nonlinear mode that the system could not recover from until the ends of the corresponding pings. Moreover, the measured SL values at the other frequencies were more than 10 dB higher than the expected SL values shown in Figure 1.5a, possibly gained by the excess self-noise (Figure 4.1). The SL values noted in the logs during the data collection gave better average estimates of the transmitted power on each ping.

All the TL results are compared to a theoretical model that includes spherical/cylindrical spreading and absorption which is modeled based on work of François and Garrison [31-32]. As the theoretical model was used for only rough comparison to the results, depth information was not included in the absorption calculation because of diminishing factors (10^{-4} and below) of the first and especially higher orders of the depth variable in the model. The temperature was set to 14 °C, which approximates the average temperature of the upper 40-50 m layer of the water column

based on the CTD measurements. Comparison of range-dependent contributions of cylindrical and spherical spreading and absorption at the relevant frequencies is provided in Appendix A.

According to Urick [2], a model provided by Marsh and Shulkin [3] can be used for rough prediction of TL. The model defines three equations for different ranges with respect to H, skip distance originally referenced in kyd, which after conversion to km becomes:

$$H = 0.9\left[\frac{0.3}{8}(D + L)\right]^{1/2} \text{(km)}$$

Equation 6.7

D stands for water depth and L for mixed layer depth, both in meters. The equations represent the gradual transition from spherical spreading at short ranges to cylindrical spreading at long ranges. They also include the effect of boundary interactions that becomes more influential with longer ranges due to multiple reflections [30]. Ranges (R [km]) shorter than the skip distance (H) are considered short ranges, for which TL is given by:

$$TL = 20\log R + \alpha R + 60 - k_L, \text{ dB}$$

Equation 6.8

Coefficient k_L, the near field anomaly, represents the mean contribution to the field of the multiple bottom and surface reflections, and it is a function of bottom and

surface loss. As it is dependent on surface and bottom intensity-reflection coefficients, k_L varies with sea state and bottom type. The parameter α is the absorption coefficient (in dB/km). Although the reference unit of R was not specified by the authors, it appears that kyd was assumed, which is consistent with the reference unit of H before conversion to km. In addition, the additive factor of 60 dB is a result of the conversion from yd to kyd, or m to km ($20\log_{10}10^3=60$).

Ranges between H and 8H are considered intermediate ranges, for which TL is given by:

$$TL = 15\log R + \alpha R + \alpha_T\left(R/H - 1\right) + 5\log H + 59.8 - k_L,\ \text{dB}$$

Equation 6.9

The loss coefficient α_T is measured in dB/bounce, where a bounce is a cycle of bottom and surface reflection. A table of values for k_L and α_T is provided in [3] for frequencies between 0.1 and 10 kHz. The factor of 59.8 dB is nothing but a rounded value of the result of summation of the 60 dB factor, previously explained, with the factor of kyd to km conversion (1 kyd=0.9 km). Ranges bigger than 8H are considered long ranges, for which TL is given by:

$$TL = 10\log R + \alpha R + \alpha_T\left(R/H - 1\right) + 10\log H + 64 - k_L,\ \text{dB}$$

Equation 6.10

As stated in Chapter 4, the average wind speed in the study area during the experiments was between 6 m/s and 8 m/s [27]. That wind speed range is equivalent to

sea state 3. Table 6.1 contain some of the parameters that are used later in this chapter for the purposes of comparing TL estimated by the foregoing semi empirical equations with the experimental results. The parameters were only provided for each octave starting from 0.1 kHz up to 10 kHz. Therefore only the three frequencies shown in Table 6.1 correspond to frequencies used in the experiment.

F (kHz)	Sand		Mud	
	k_L (dB)	α_T (dB/bounce)	k_L (dB)	α_T (dB/bounce)
4	3.2	3.9	2.8	5.8
8	2.6	4.7	2.2	6.9
10	2.4	5.0	2.0	7.5

Table 6.1 Near-field anomaly k_L (dB), and shallow water attenuation α_T (dB/bounce); data from Marsh and Shulkin [3]; sea state=3 [27].

In a number of figures that follow, a negative range is adopted for the sections of the experimental routes along which the towed source transducer was moving toward the moored hydrophones, whereas a positive range is used for the sections where it was moving away from them.

Since the expression for the skip distance as well as the TL formulas and the corresponding coefficients, are semi empirically derived based on a large set of measurements in 0.1 kHz to 10.0 kHz frequency band, the validity of the skip distance is constrained accordingly. The authors of the model did not specify a maximum water depth. The specifications in the referenced literature were found not to exceed 46 m [33].

Tanner-Cortes Bank Site

The maximum ranges at which direct-path arrivals are anticipated to exist, based on the analysis in Chapter 3 devoted to the site between Tanner Bank and Cortes Bank, are summarized in Table 6.2. The sound channeling in the mixed layer of the 6 AM SSP predicts generally longer direct-path ranges than the noon conditions. Besides the theoretically non-limited direct-path distances, some of the values in the table correspond to the local minimum SSP layers like the one highlighted with a dashed beam in Figure 3.2; therefore, the ray tracing in Figure 3.7 shows that the channeling caused by the 6 PM SSP (Figure 3.1) increases the chance of having a direct-path arrival at longer ranges than with the noon SSP, but not as much as the 6 AM SSP.

Source depth [m]	Receiver depth [m]	6 AM	Noon	6 PM
40	27	5 km	2.2 km	3.9 km*
	61	8 km*	2.8 km	4.7 km*
19	27	nl	1.6 km	nr
	61	3.5 km	2.1 km	nr

Table 6.2 Direct-path distances at the hydrophone depths, based on Figure 3.2 and Figure 3.3. nl = not limited. nr = not relevant; * ⇒ singularity.

Figure 6.1 illustrates Equation 6.8 to Equation 6.10 for the noon conditions. According to Table 6.3, the skip distance would vary less than a tenth of a kilometer if opted for different time of day, hence the corresponding curves would not differ significantly from these. The near field anomaly does not exceed 3.2 dB at the

corresponding frequencies (Table 6.1) and does not take a significant part in the short-range TL. The bouncing loss coefficient α_T (Table 6.1) does not have a noticeable effect at ranges shorter than about one and a half to twice the skip distance. Thus one and a half to twice the values listed in Table 6.3 can be, approximately, interpreted as the direct-path distances for the corresponding SSPs. Since the emphasis of this thesis is direct-path TL, further analysis of the bottom interaction effect is excluded.

SSP	Water depth [m]	Mixed layer depth [m]	Skip distance [km]
6 AM	113	27	2
Noon	116	7	1.92
6 PM	115	10	1.94

Table 6.3 The skip distances computed with Equation 6.7 that correspond to the SSPs in Figure 3.1.

The decrease in the source transducer depth indicated in Table 1.2 happened at the CPA point. It means that the source was towed at a deeper depth toward the receivers than it was when moving away from the receivers.

If the noon SSP from Figure 3.1 were employed in ray tracing, a non-reflected path in a downward refracting environment would exist at longer ranges in deeper depths. Excluding the 30 kHz case, experimental TL curves at negative ranges in Figure 6.2, which correspond to a 40 m source depth, seem to start exceeding spherical spreading plus absorption losses, between 3 km and 4 km.

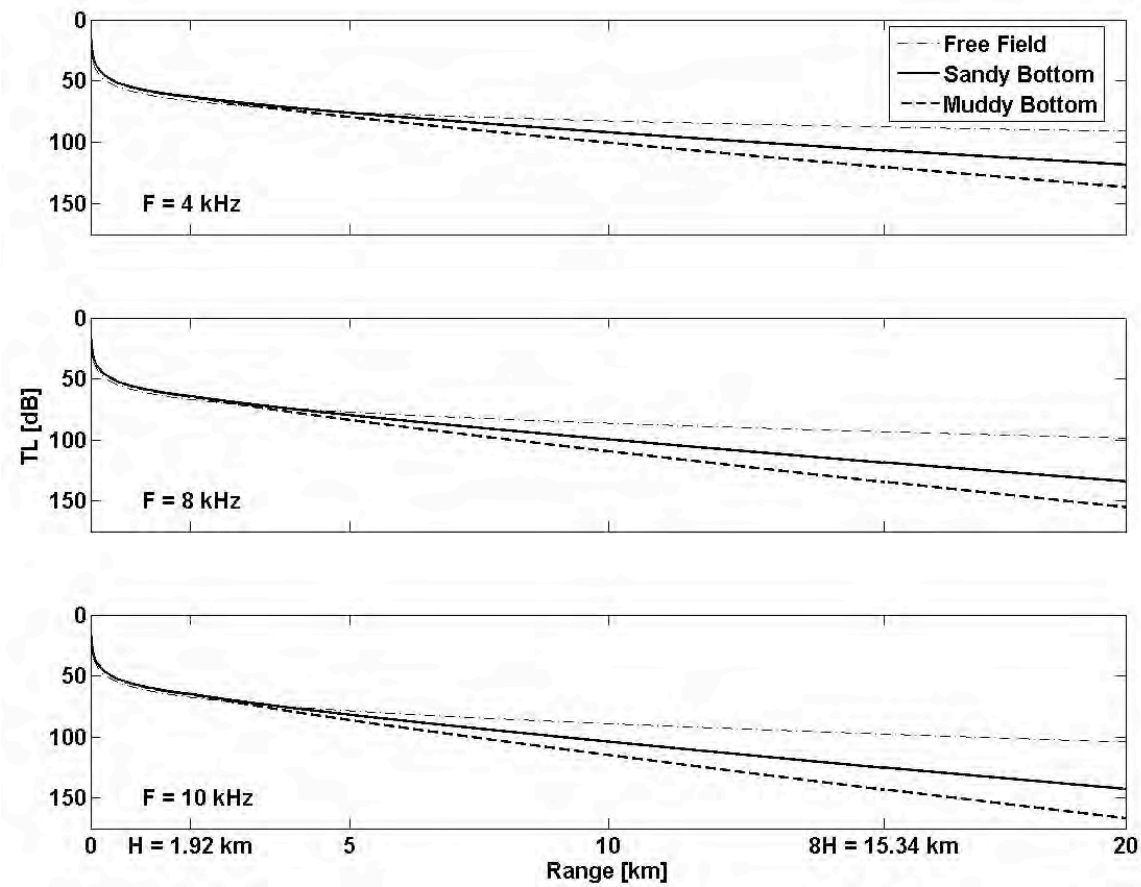

Figure 6.1 TL estimation for the Tanner-Cortes Bank based on the semi empirical equations (Equation 6.7 to Equation 6.10); data from Marsh and Shulkin [3]. The free-field curve includes spherical spreading plus absorption in water; data from François and Garrison [31] [32].

In the case of a 19 m source transducer depth (positive ranges), the overall trend remains downward refraction (Figure 3.3); however the limiting ranges are shorter (Table 6.2) because ray windowing [5] is more selective when the source is shallower and below the mixed-layer.

At 15 kHz, Figure 6.3 shows that, at "negative" ranges, the experimental TL values are scattered around a mean that exceeds the free-field model, starting around −3.5 km. The mean varies in range, and is around 5 dB lower than the free-field model, between −3.5 km and the CPA. For the corresponding source/receiver depth, the apparent

gain cannot be ascribed to surface or bottom ducting; therefore it is either caused by ray focusing, as described in Chapter 3, or is a noise related issue. Around −3.5 km range, the experimental TL curve features steep transition toward values beyond the theoretical model.

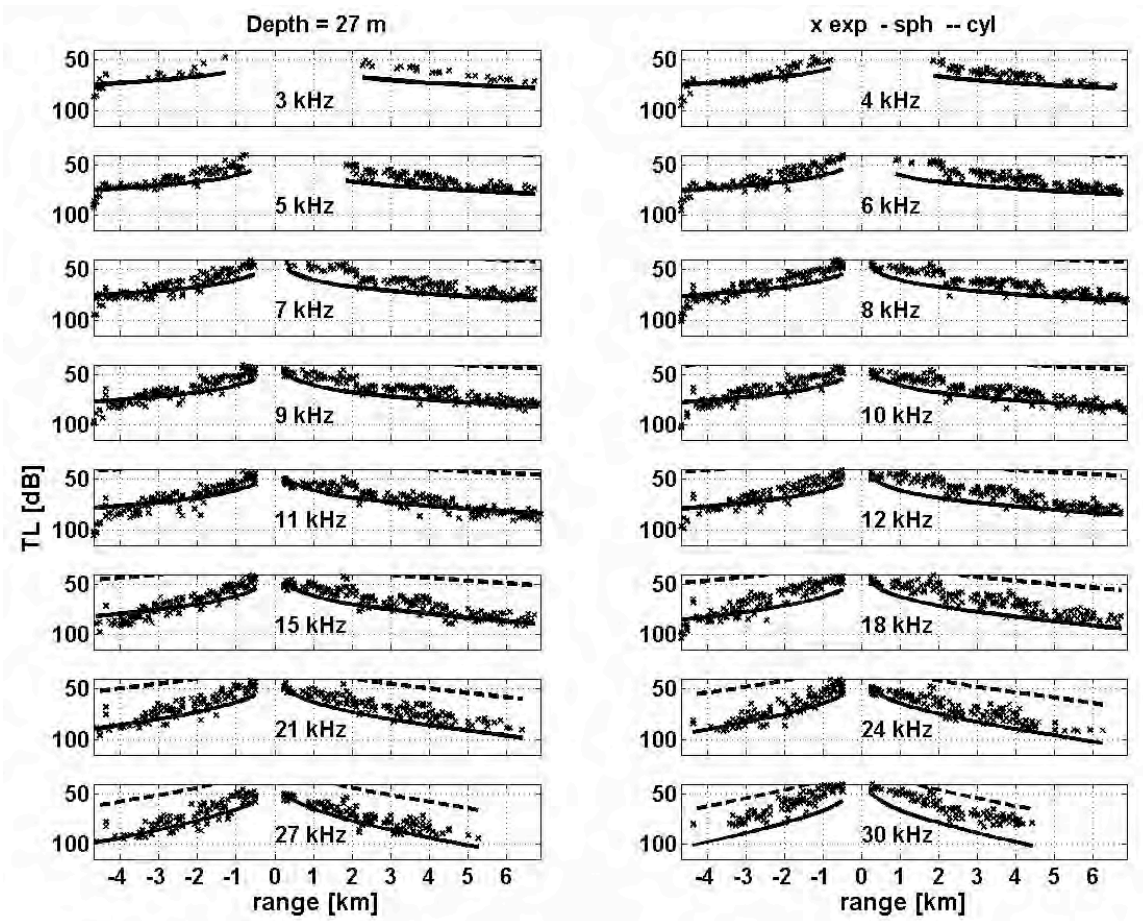

Figure 6.2 TL vs. range at the 16 frequencies; location from Figure 1.2a (along the solid line), for hydrophone depth of 27 m. Source depth was 40 m and 19 m for negative and positive ranges, respectively; *exp* = experimental; *sph* = spherical spreading plus absorption in water; *cyl* = cylindrical spreading plus absorption in water; absorption data from François and Garrison [31-32].

The experimental TL curves in Figure 6.2 do not exceed the free-field theoretical curves for ranges longer than 4 km, which means that 19 m might have been inside the

mixed layer, having direct-path beams projected into the local-minimum SSP layer (Figure 3.3), hence implying that transition from the 6 AM SSP to the noon SSP might have not been finished by the end of the track. The narrower the layer is, the closer direct path is to a straight line, which is a spherical spreading equivalent in terms of TL [2].

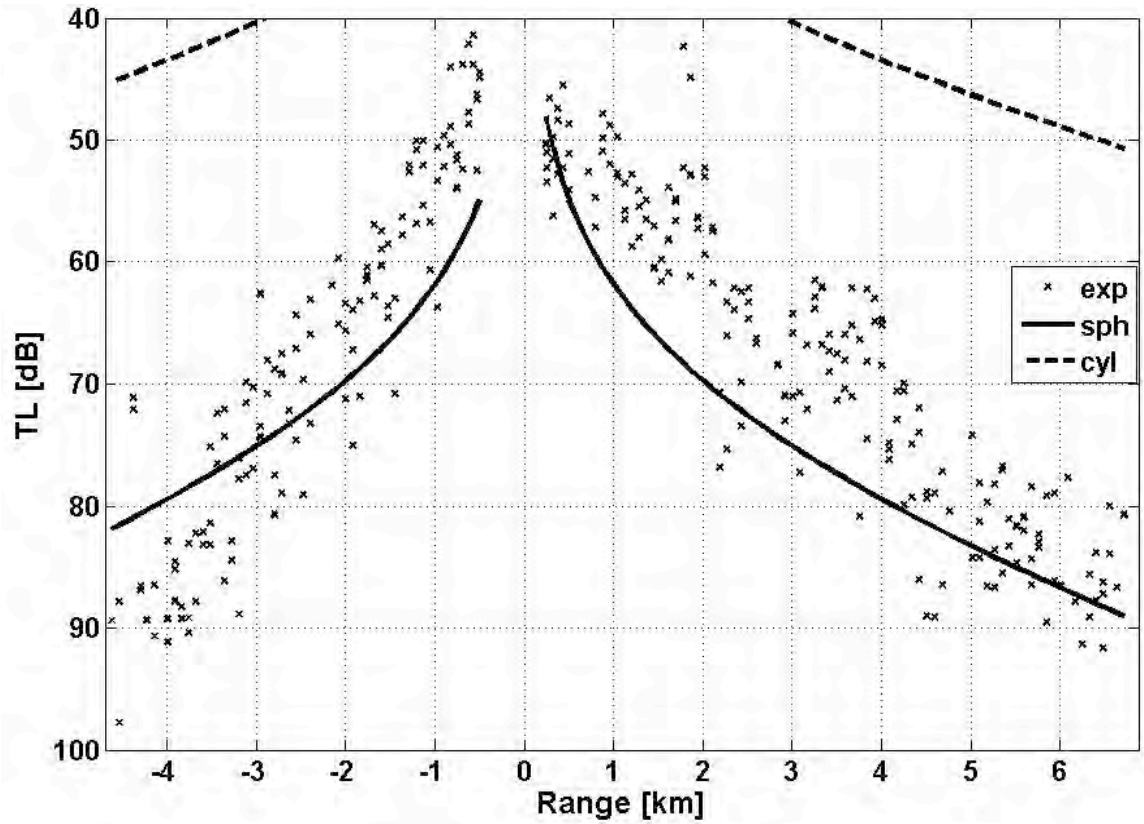

Figure 6.3 Blow-up of the TL vs. range at 15 kHz plot in Figure 6.3; hydrophone depth of 27 m; source depth was 40 m and 19 m for negative and positive ranges, respectively; *exp* = experimental; *sph* = spherical spreading plus absorption in water; *cyl* = cylindrical spreading plus absorption in water; absorption data from François and Garrison [31-32].

Experimental direct-path distance, recognized as range where a measured TL curve starts exceeding the spherical-spreading-plus-absorption curve, varies with

frequency; nonetheless, a loose average will be taken here as an approximate value for each frequency used.

The experimental TL curves in Figure 6.4 do not exceed the corresponding free-field (spherical-spreading-plus-absorption) models at ranges longer than the noon values in Table 6.2, which implies the existence of direct-path arrivals at extended ranges. The persisting scarcity in the 3 kHz experimental TL points may be due to masking noise.

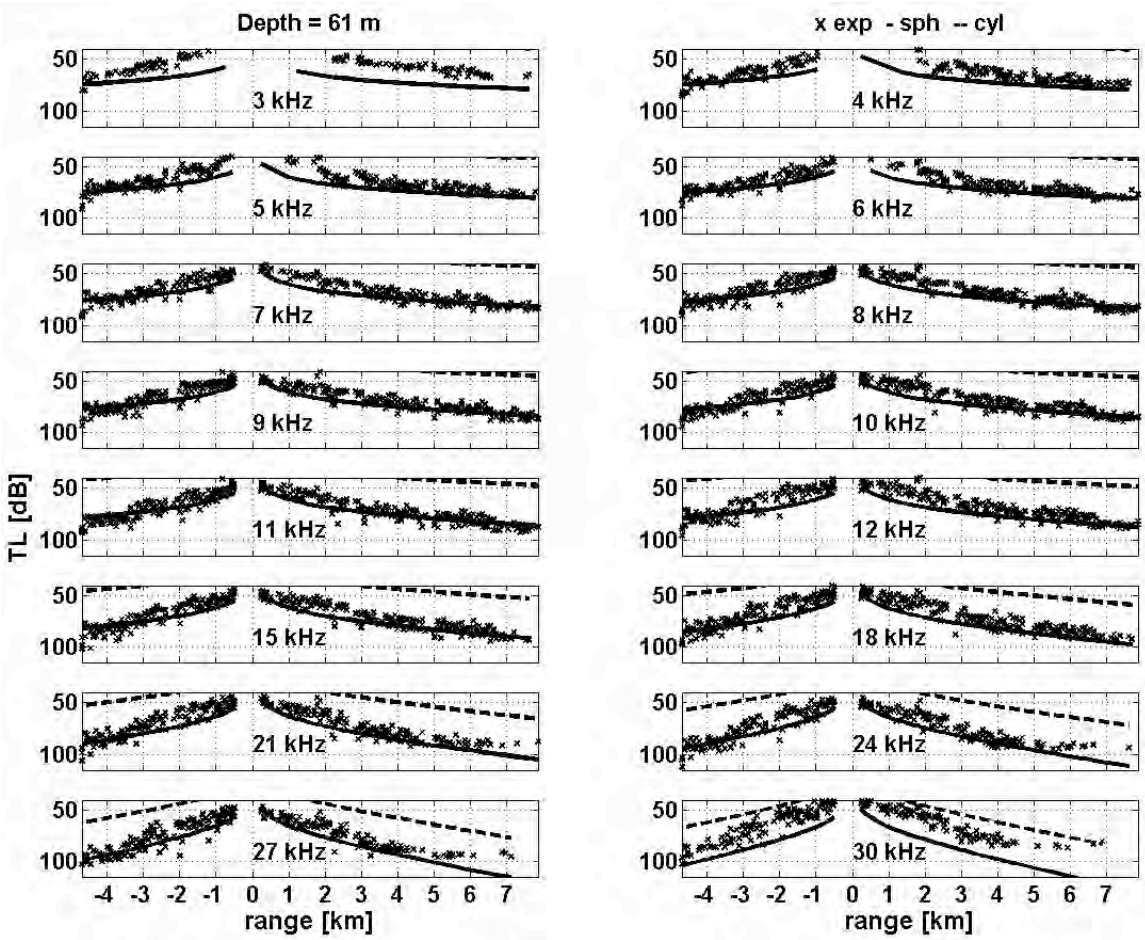

Figure 6.4 TL vs. range at the 16 frequencies; location from Figure 1.2a (along the solid line); hydrophone depth 61 m. Source depth was 40 m and 19 m for negative and positive ranges, respectively; *exp* = experimental; *sph* = spherical spreading plus absorption in water; *cyl* = cylindrical spreading plus absorption in water; absorption data from François and Garrison [31-32].

The experimental curves show, on average, around 10 dB lower TL than spherical spreading plus absorption between −2 km and the CPA and as long as about +4.5 km in Figure 6.2, and in the first three kilometers on both sides of the CPA in Figure 6.4. If measurement uncertainty is excluded as a possible reason of the mismatches, then it can be explained as a consequence of focusing of sound energy into narrow channels, as described in Chapter 3. The highly concentrated beams in the lower sub-layer of the mixed layer (Figure 3.2a), corresponding to the positive-range section in Figure 6.2, create a strong sound field around the depth of the shallower hydrophone. The corresponding part of the experimental curve in Figure 6.4 is a few decibels higher accordingly. This interpretation of the experimental results should include a disclaimer: the positive-range beginning is noisier, especially at frequencies below 7 kHz, because the ship's propellers were facing the hydrophone; if added to the SPL of the signal, excess noise manifests itself as a gain, yielding a false impression of lower TL. The near field anomaly k_L, which is not included in the plots, could contribute to this mismatch. According to Table 6.1 the effect should keep decreasing with increasing frequency; a logical extension of the near field anomaly at frequencies beyond 10 kHz would contain values lower than 2.4 dB. Finally, notice that the experimental TL values at 30 kHz are not consistent with the values at other frequencies, which may be a consequence of an inaccurate transducer calibration at the "edges" of the TVR spectrum of the source transducer (Figure 1.5a) coupled with low SNR.

As shown in Figure 6.5, when the source was below the mixed layer (negative ranges) TL at the receiver below the mixed layer was mostly lower than at the in-the-layer receiver before -3 km in range. As the ship continued to approach the hydrophones

and passed the CPA, the TL through the two communication channels became approximately the same, until the range of around 3 km; between 3 km and 5 km the communication channel with the shallower hydrophone had better transmission. In fact, when the source was 40 m deep (Figure 3.2b), there was a bottom duct, which might have positively affected the deeper hydrophone at mid/long ranges, in spatial periods of approximately 2 km, which is a period of a bottom bounce.

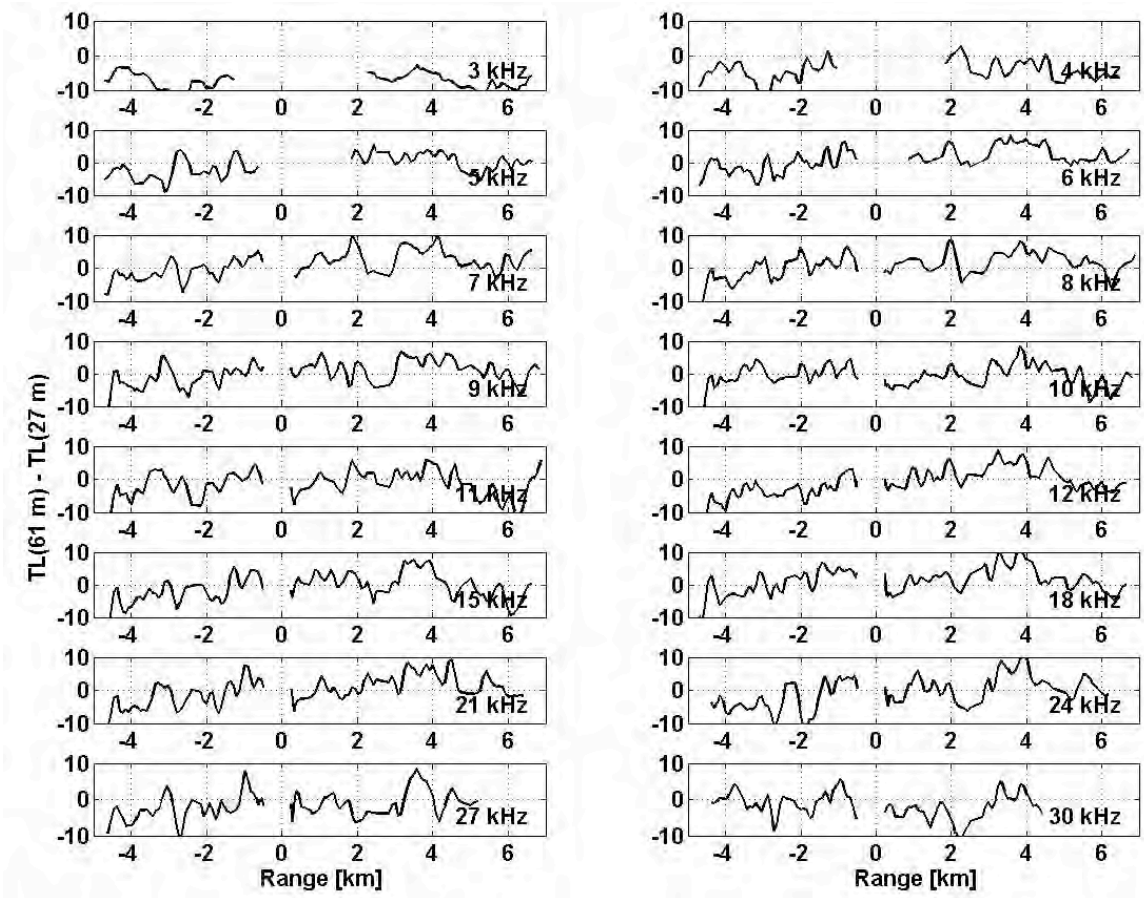

Figure 6.5 Difference in the measured TL at 61 m and 27 m at the 16 frequencies; location from Figure 1.2a (along the solid line). The differences in TL higher than 10 dB are not presented. Source depth was 40 m and 19 m for negative and positive ranges, respectively.

When the source was 19 m deep (positive ranges), the sound trapping shown in Figure 3.2a would be expected to favor the shallower hydrophone. Past 5 km transmission was slightly better at the deeper hydrophone, especially at some frequencies, e.g. 10 kHz and 11 kHz. Therefore 19 m might have not been in the mixed layer at that point, which implies noon-SSP-like conditions. Under the noon conditions, the alternating transmission superiority at mid/long ranges between the two channels could be again ascribed to the bottom bouncing. Every time a bundle of beams bounces off the bottom the ray windowing and ray tube effect favor the receiver that is closer to the depth of the source (Figure 3.3).

The TL differences higher than 10 dB are not shown in Figure 6.5 and subsequent figures of this kind; it is sufficient to provide a rough estimate of more optimal receiver depth with respect to TL.

The sections with SNR < 6 dB at short ranges (below 2 km) and low frequencies (below 8 kHz) in all of the contour plots in this section are a consequence of the excess noise, as described in Chapter 4. The white regions at longer ranges at the lowest and the highest frequencies exist due to the source power limitations in those frequency bands (Figure 1.5a).

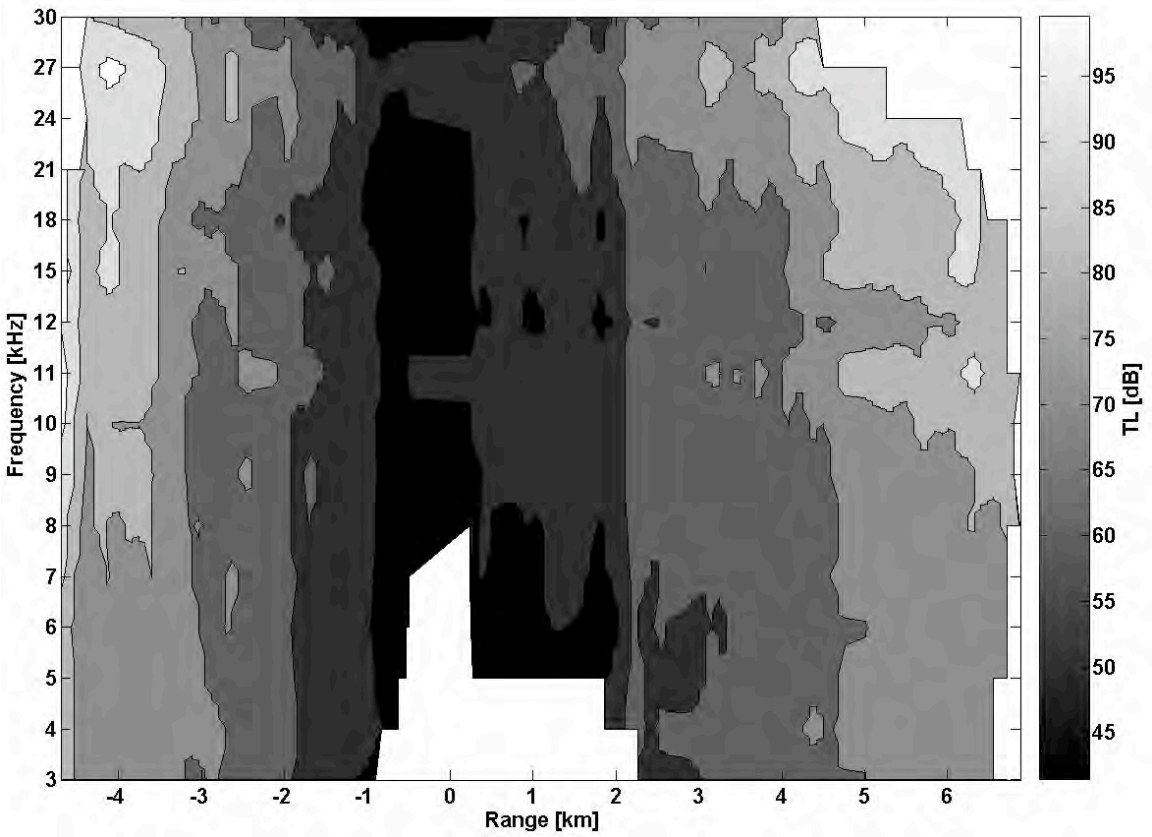

Figure 6.6 Contours of TL vs. range and frequency, measured at Cortes-Tanner Bank (Figure 1.2a along the solid line), for hydrophone depths of 27 m. The white regions correspond to SNR < 6 dB. Source depth was 40 m and 19 m for negative and positive ranges, respectively.

According to Figure 6.6 it could be said that for the provided technology and in the given environment, TL does not significantly change between 3 kHz and 8 kHz, and between 12 kHz and 18 kHz, inside the first 2.5 km. This is not unexpected because spreading loss is much higher than absorption at lower frequencies and short ranges (Appendix A).

In Figure 6.7, TL does not significantly change between 6 kHz and 11 kHz, and between 12 kHz and 21 kHz, before 3 km. Lower TL at 30 kHz than at 21 kHz – 27 kHz

between 4 km and 6 km is not expected, and it could be caused by lower accuracy of the TVR calibration at the ends of the operational frequency band (Figure 1.5a).

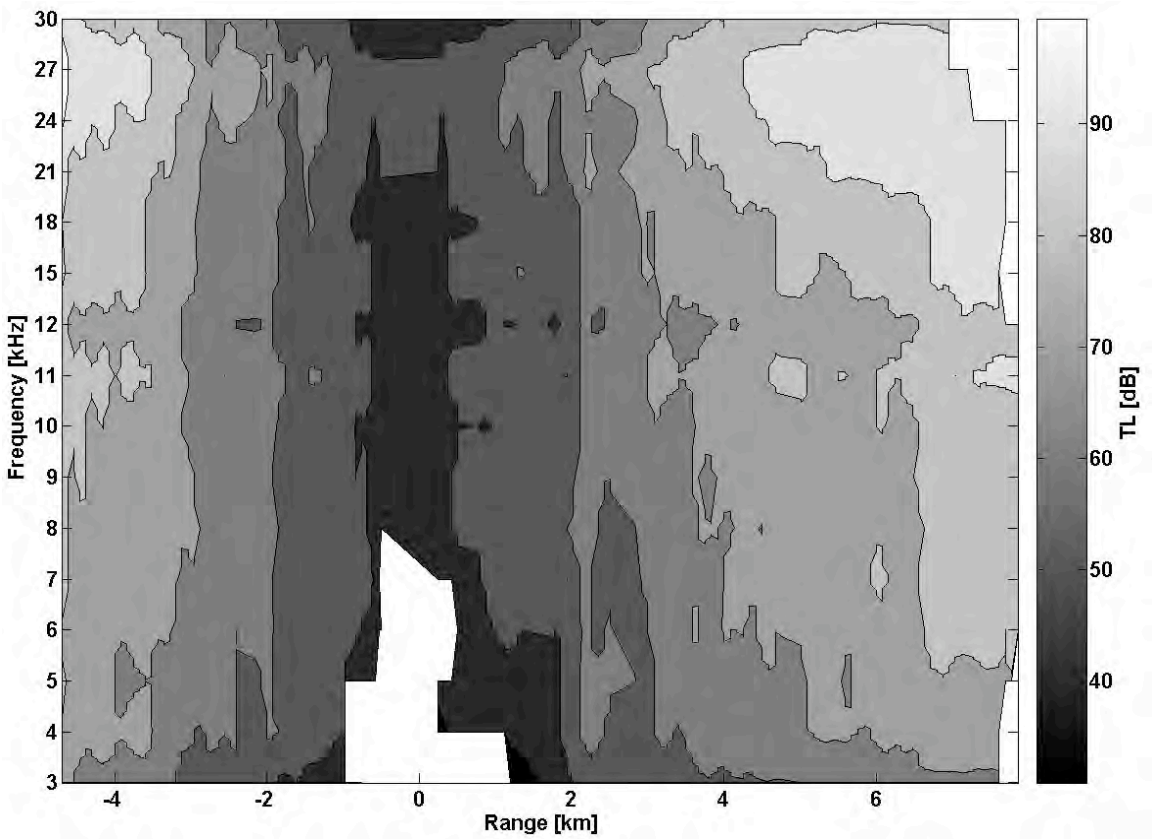

Figure 6.7 Contours of TL vs. range and frequency, measured at Cortes-Tanner Bank (Figure 1.2a along the solid line), for hydrophone depths of 61 m. The white regions correspond to SNR < 6 dB. Source depth was 40 m and 19 m for negative and positive ranges, respectively.

The second track at Tanner/Cortes Bank (dashed line in Figure 1.2a) was run during afternoon hours (Table 1.1). Therefore a proper choice of the SSP would be between the noon SSP and the 6 PM SSP (Figure 3.1).

The sections of the experimental TL in Figure 6.8 that correspond to the phase when the ship was approaching the hydrophones are scattered around a mean that is,

within 5 dB, equal to the free-field, spherical-spreading-plus-absorption model. Although the source depth was kept constant during the increasing distance phase, there is a noticeable inconsistency on the positive-range sides of the measured TL curves at various frequencies. At frequencies between 12 kHz and 21 kHz the experimental curves show lower TL than the free-field model.

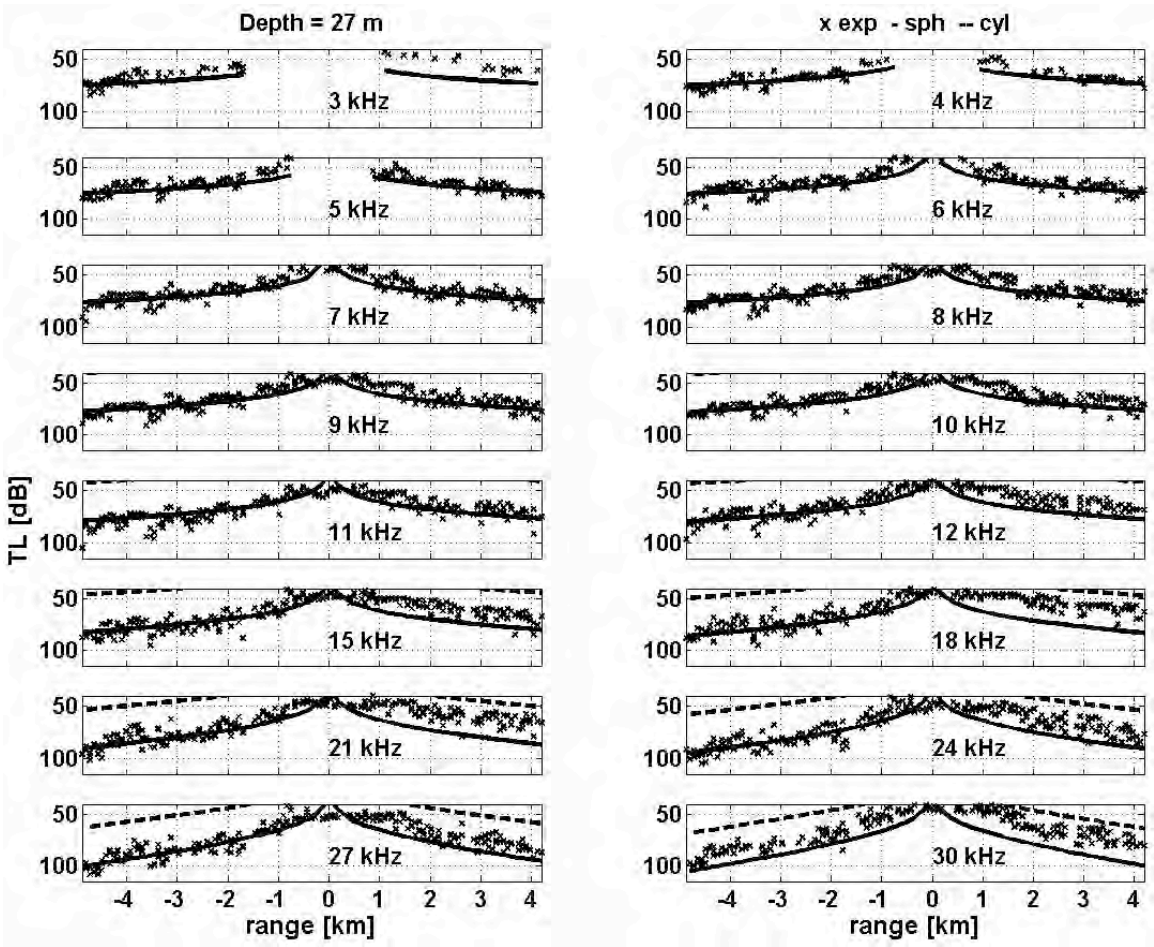

Figure 6.8 TL vs. range at the 16 frequencies; location from Figure 1.2a (along the dashed line); hydrophone depth 27 m. Source depth was 40 m; *exp* = experimental; *sph* = spherical spreading plus absorption in water; *cyl* = cylindrical spreading plus absorption in water; absorption data from François and Garrison [31-32].

The right-hand halves of the experimental curves in Figure 6.9, at frequencies between 9 kHz and 15 kHz, are scattered around a mean equal to, within 10 dB, the free-field model.

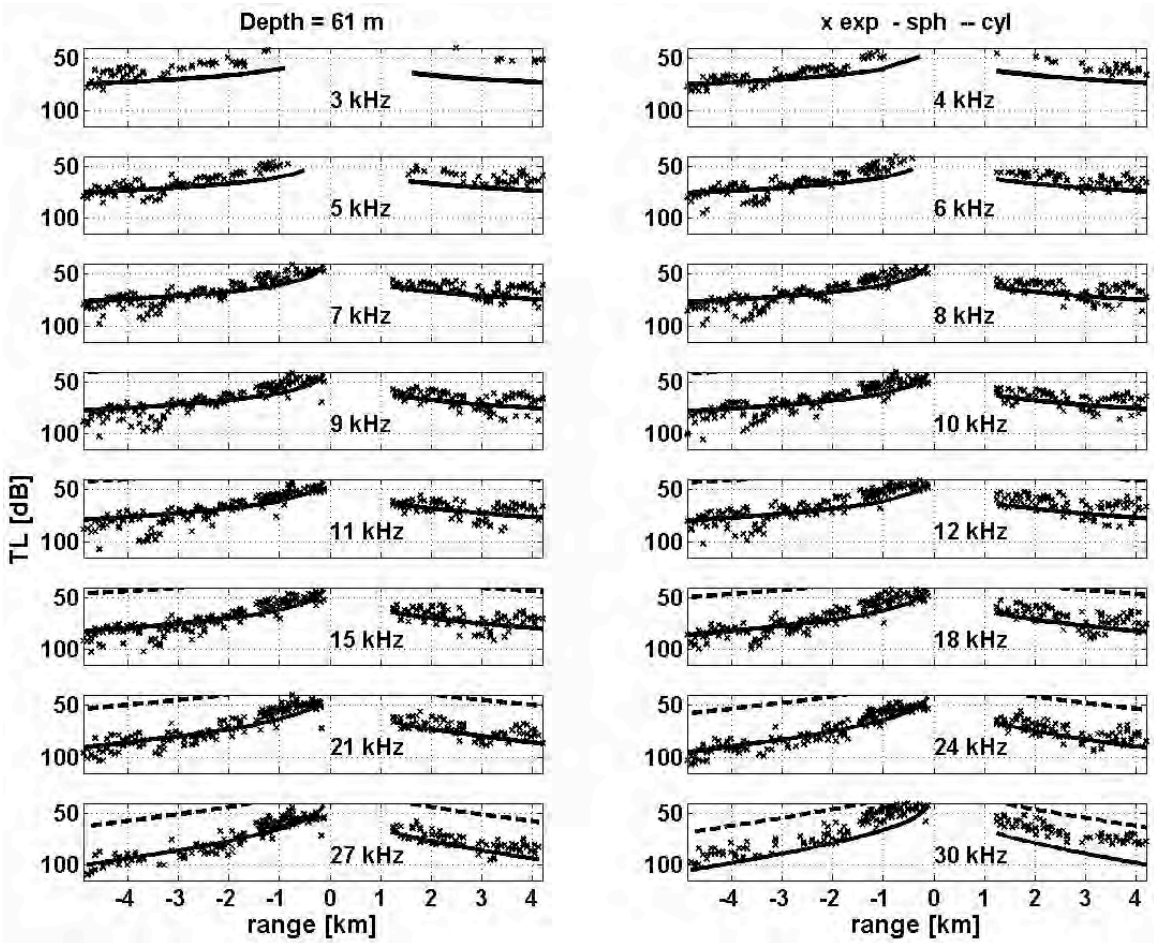

Figure 6.9 TL vs. range at the 16 frequencies; location from Figure 1.2a (along the dashed line); hydrophone depth 61 m. Source depth was 40 m; *exp* = experimental; *sph* = spherical spreading plus absorption in water; *cyl* = cylindrical spreading plus absorption in water; absorption data from François and Garrison [31-32].

The background NL at the shallower receiver, shown in Figure 4.4a, was about 10 dB higher in that frequency band than the background NL at the same receiver, in the calmer section of the experimental track when the ship's propellers were not facing the

hydrophones, whereas the NL at deeper hydrophone was not significantly different. The excess NL could add to the SPL of the pulses, thus creating a false impression of better transmission in the shallower channel.

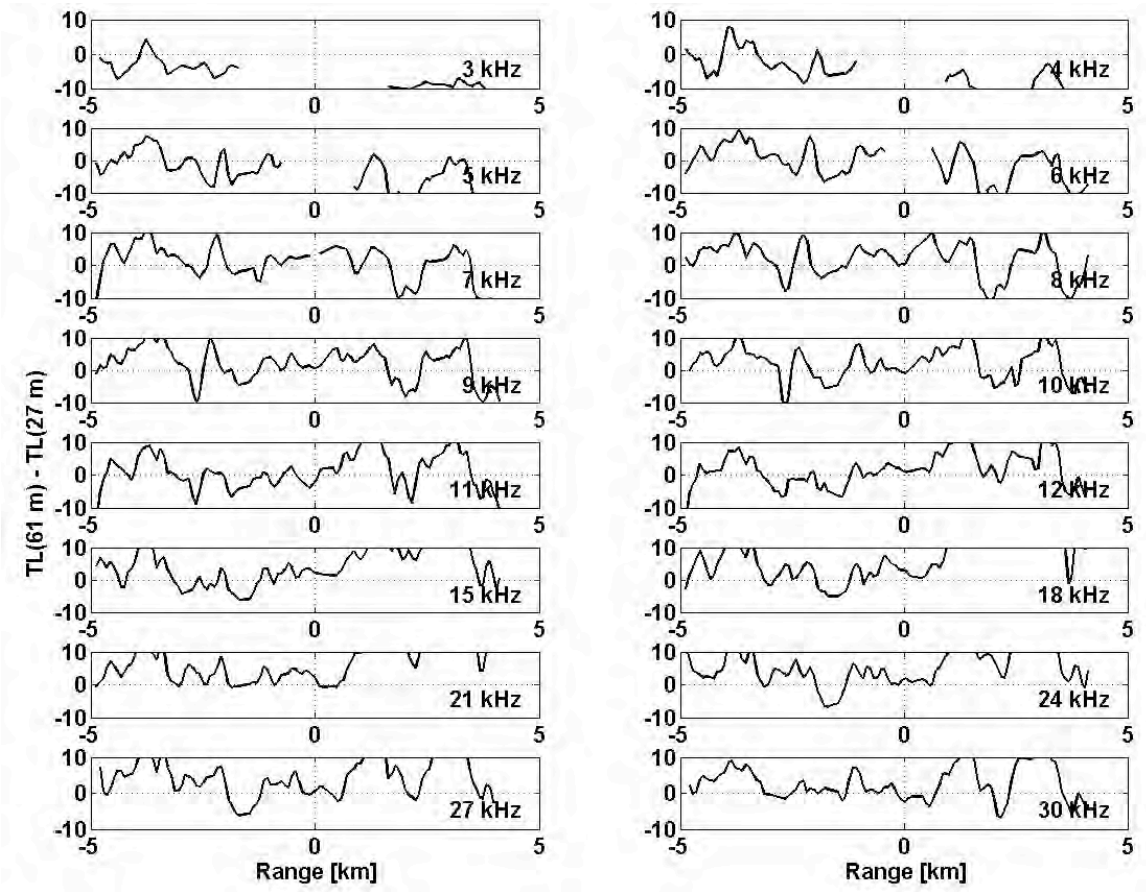

Figure 6.10 Difference in the measured TL at 61 m and 27 m at the 16 frequencies; location from Figure 1.2a (along the dashed line). Differences higher than 10 dB are not presented.

The left side of the experimental TL curves in Figure 6.10 indicates lower TL before approximately -3 km at the shallower hydrophone, despite the bottom-duct effect (Figure 3.3). Therefore, the ray tracing in Figure 3.7, characterized by shedding of the

bundles of beams into the upper layers of the water column, appears to be a better model for this part of the experiment. Hence, the actual SSP is probably closer to the 6 PM SSP.

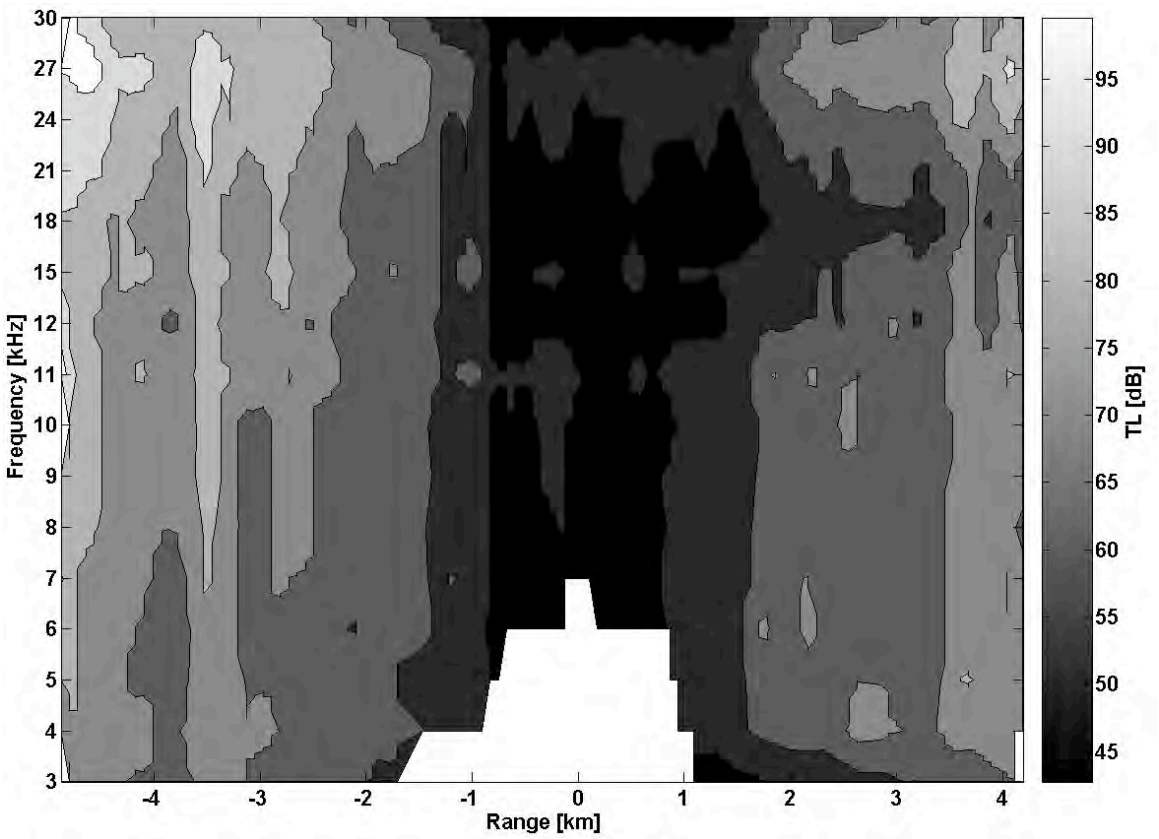

Figure 6.11 Contours of TL vs. range and frequency, location from Figure 1.2a (along the dashed line), for hydrophone depths of 27 m.

In Figure 6.11, TL does not significantly change between 6 kHz and 10 kHz, before 2.5 km. The effect of the excess NL manifests itself through the protrusion of the low TL section beyond +2 km ranges in the 12 kHz – 21 kHz band on the right side of the CPA.

The vertical layers in Figure 6.12 that represent regions of uniform TL across frequencies are narrower than the shallower counterparts in Figure 6.11, possibly as a

consequence of the bottom bouncing of the ray-bundles (Figure 3.7) that has shorter spatial period on deeper depths.

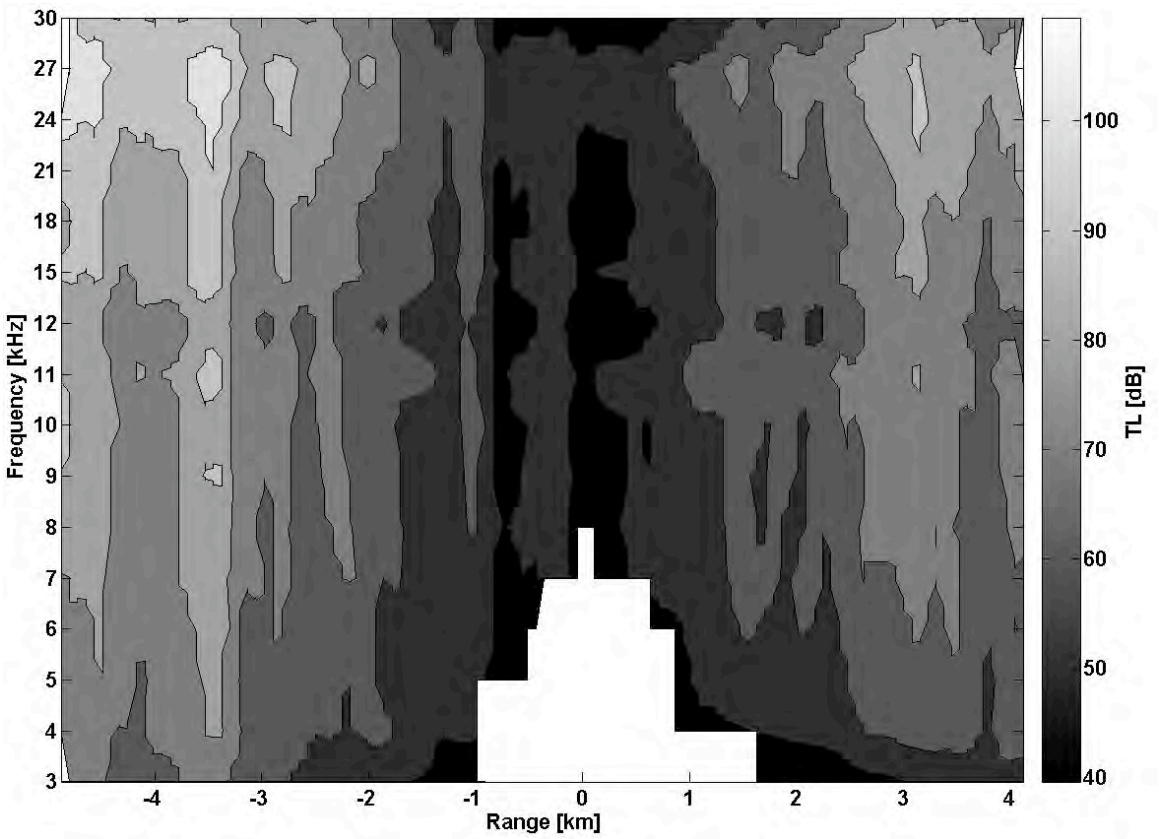

Figure 6.12 Contours of TL vs. range and frequency, measured at Cortes-Tanner Bank (Figure 1.2a along the dashed line), for hydrophone depths of 61 m.

The foregoing discussion should be annotated with a few remarks. As shown in Figure 1.2a, the first track went across the channel formed by the two banks (solid line) and the other one along the channel (dashed line), which is evident in Figure 1.1. Topography was different in each case. The overall depth ranged between 80 m and 120 m in both cases, which could change the reverberation level but not the direct-path arrivals at the receivers. In that regard, bathymetric data did not indicate significant

differences in the bottom profiles along the tracks. The SSPs were measured in the vicinity of the intersection point.

The analysis conducted in Chapter 3 showed that the time resolution used in the experiment may have not been sufficient for the separation of a direct-path arrival and a surface reflection at a 27 m deep receiver depth at short ranges. At the first intersection of the two highlighted beams in Figure 3.4b, the corresponding horizontal range is roughly 1 km, and the travel time difference Δt is approximately 1 ms. Adequate time resolution would require a CW pulse around 1 ms long. For a 30 kHz pulse, 1 ms in duration would include 30 cycles, but for a 3 kHz pulse only 3 cycles, which may be too few for a reliable detection and the average acoustic intensity calculation. Shortening the pulse would cause poorer matched-filter detection performance, especially at lower frequencies ,because more cycles bring in more of the signal pattern and more accumulated energy for the matched-filter detector. In terms of the frequency spectrum of a pulse, another disadvantage of a shorter pulse is that it would have lower spectral resolution [21].

The ADCP measurements performed during the experiment showed a pattern that matched the regional semi-diurnal tidal cycle, with maximum depth of the current jet around 80 m. Because the tracks were run perpendicularly to each other (Figure 1.2a), they had orthogonal positions with respect to the current jet. Since the experiments were not designed to accurately examine the influence of the currents on propagation, further analysis on that topic is excluded. It is however important to understand that sub-surface currents can bring significant changes to the SSP, especially the surface layer section, and thereby change the propagation conditions. Based on a static link in the same area, Romond [34] showed that signals that come from rays that spend significant time in the

current jet suffer much more fluctuation. The same author also pointed out the overwhelming effect of internal waves on underwater sound propagation.

South of China Point Site

The maximum ranges at which direct-path arrivals are expected, based on the analysis in Chapter 3 devoted to the site south of China Point, are summarized in Table 6.4. When the source depth is 18 m, the corresponding direct-path range values at 61 m depth contradict the theorem stated in Chapter 3, in the section about the site in San Nicolas Basin, that a deeper mixed layer should result in a shorter maximum direct-path range when the source is in the mixed layer and the receiver is below, as illustrated in Figure 3.12. This apparent contradiction is an artifact of a very narrow layer with almost constant sound speed at 61 m depth that causes sound channeling, as explained in Chapter 3.

Source depth [m]	Receiver depth [m]	Noon	6 PM
60	27	2.8 km	2.5 km
	61	nl	nl
35	27	3 km	2.5 km
	61	2.2 km	3.5 km
18	27	4.2 km	2.5 km
	61	3.8 km	3.5 km

Table 6.4 Direct-path distances at the hydrophone depths, roughly estimated based on the analysis in Chapter 3 . nl = not limited.

The biggest difference between the direct-path distances in Table 6.4 and Table 6.5 that correspond to the same SSP is for 18 m source depth, noon SSP, and 27 m receiver depth, and it equals approximately 2 km. Since it was shown (Figure 6.1) that the evident transition from the short ranges (Equation 6.8) to intermediate ranges (Equation 6.9) takes place around one and a half to twice the skip-distance, defined in Equation 6.7, the rough semi-empirical estimates in Table 6.5 seem to be a reasonable match to the ray-tracing based estimates at this site.

SSP	Water depth [m]	Mixed layer depth [m]	Skip distance [km]
Noon	99	55	2.16
6 PM	89	30	1.9

Table 6.5 The skip distances computed with Equation 6.7 that correspond to the SSPs in Figure 3.8.

The site south of the San Clemente Island's China Point had a well defined mixed layer ranging between 30 m and 55 m in depth. During the experiment, the source transducer depth was changed from around 60 m to approximately 35 m very close to the CPA (Table 1.2), which means that along the "negative" ranges in Figure 6.13 and Figure 6.14 the source transducer was below the mixed layer. The beams that get into the mixed layer turn upward and bounce off the surface, introducing surface scattering loss at certain ranges.

In Figure 6.13 the measured TL at the frequencies from 8 kHz to 24 kHz exceed the theoretical curves, starting somewhere between −3 km and −2 km, which favors existence of a non-direct path beyond that range. The experimentally determined direct-

path distances are in good agreement with the corresponding values in Table 6.4 for either SSP.

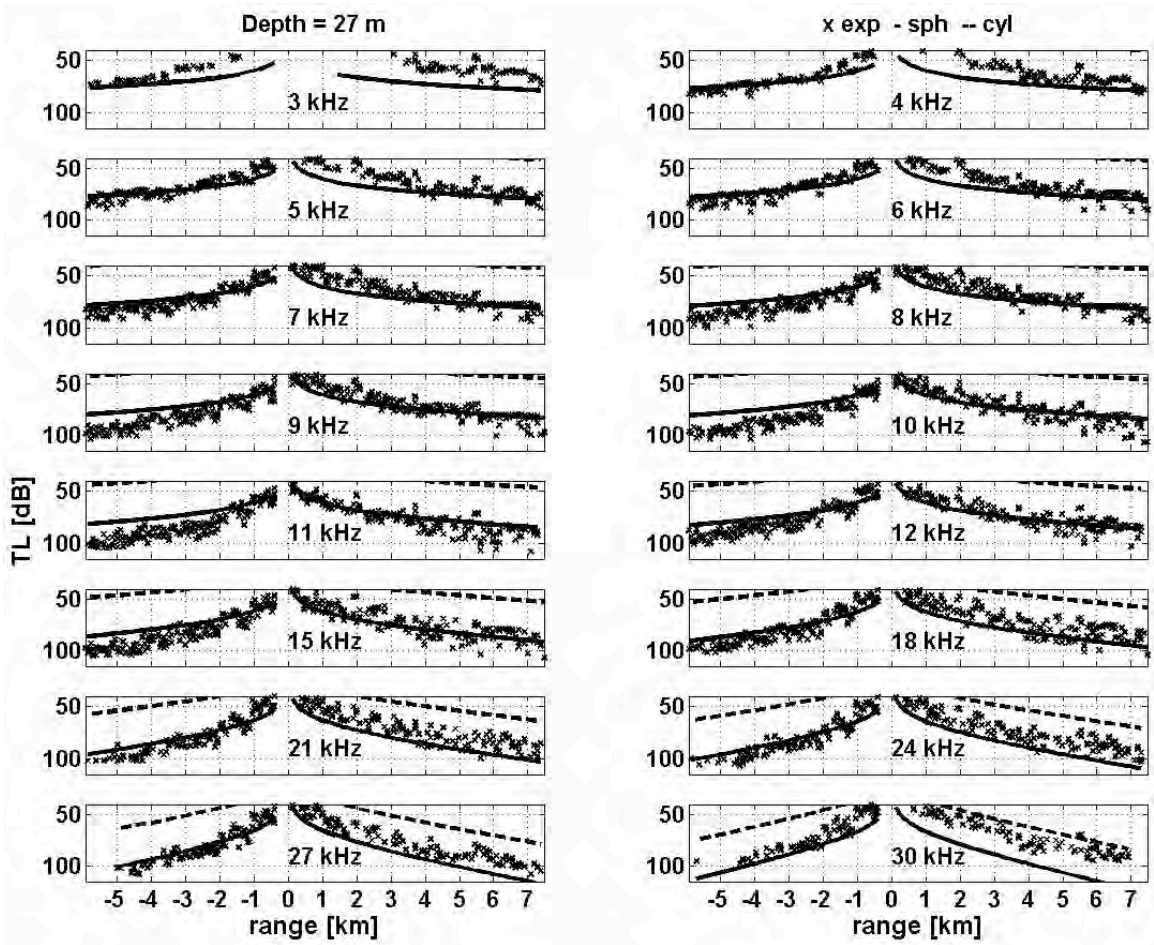

Figure 6.13 TL vs. range at the 16 frequencies; location from Figure 1.2b (along the solid line); hydrophone depth 27 m. Source depth was about 60 m and 35 m for (-) and (+) ranges, respectively; *exp* = experimental; *sph* = spherical spreading plus absorption in water; *cyl* = cylindrical spreading plus absorption in water; absorption data from François and Garrison [31-32].

Direct-path ranges, recognized by the experimental TL values that did not exceed the theoretical curves, at the deeper receiver (Figure 6.14) are approximately 4 km long, when the source was 60 m deep, and are in solid agreement with direct-path distances

estimated as one and a half to twice the skip distances from Table 6.5, as opposed to the shallower receiver counterparts. Thus, for the source below the mixed layer, the ray-tracing based estimation of the direct-path distance was closer to the experimentally determined value when the receiver was in the mixed layer, whereas Marsh and Shulkin's model [3] gave a better match for the receiver below the mixed layer.

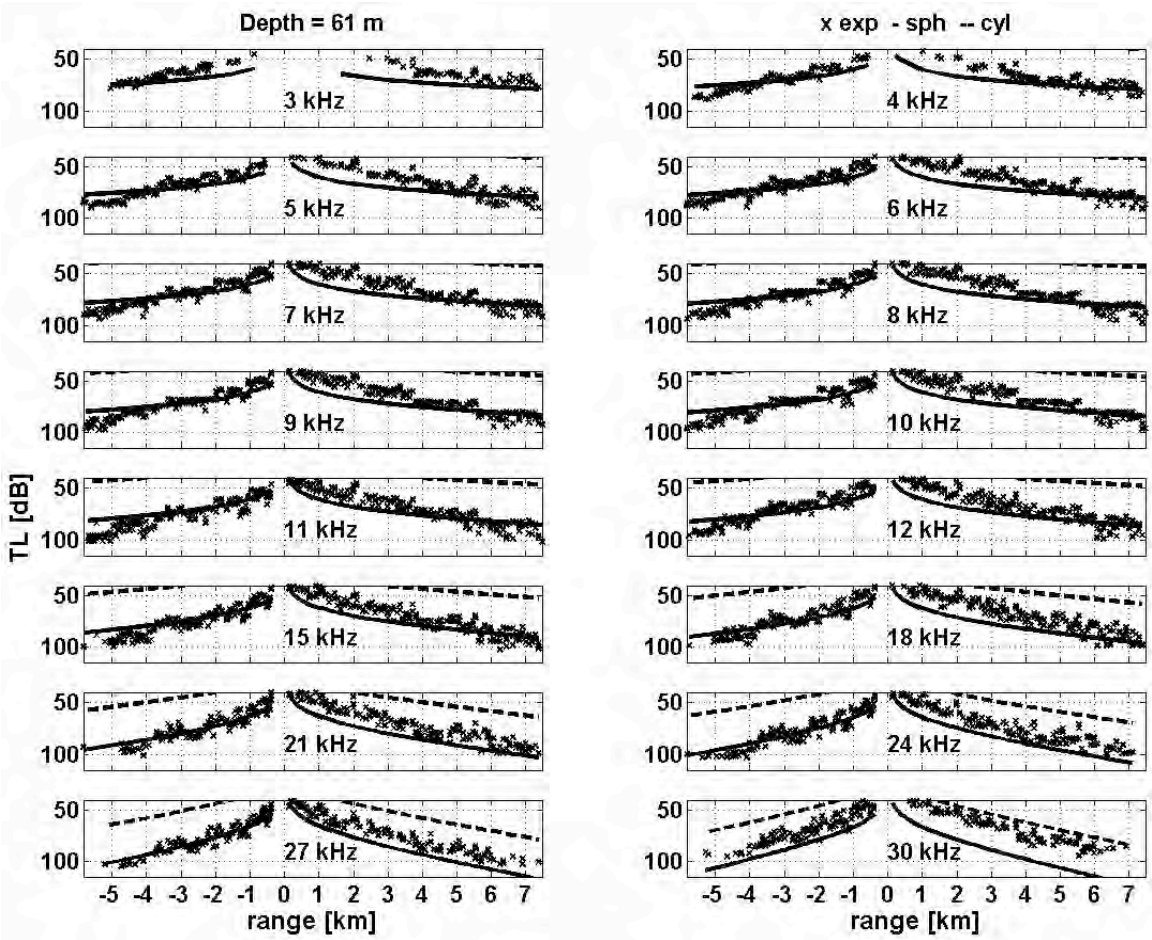

Figure 6.14 TL vs. range at the 16 frequencies; location from Figure 1.2b (along the solid line); hydrophone depth 61 m. Source depth was about 60 m and 35 m for (-) and (+) ranges, respectively; *exp* = experimental; *sph* = spherical spreading plus absorption in water; *cyl* = cylindrical spreading plus absorption in water; absorption data from François and Garrison [31-32].

Notice that the experimental values on the positive-range side of the experimental plots in Figure 6.13 are more dispersed than the values in Figure 6.14, especially at ranges beyond the 2 km zone. That implies more fluctuating sound, possibly due to surface scattering, at the shallower receiver when the source was closer to the sea surface than to the sea bottom.

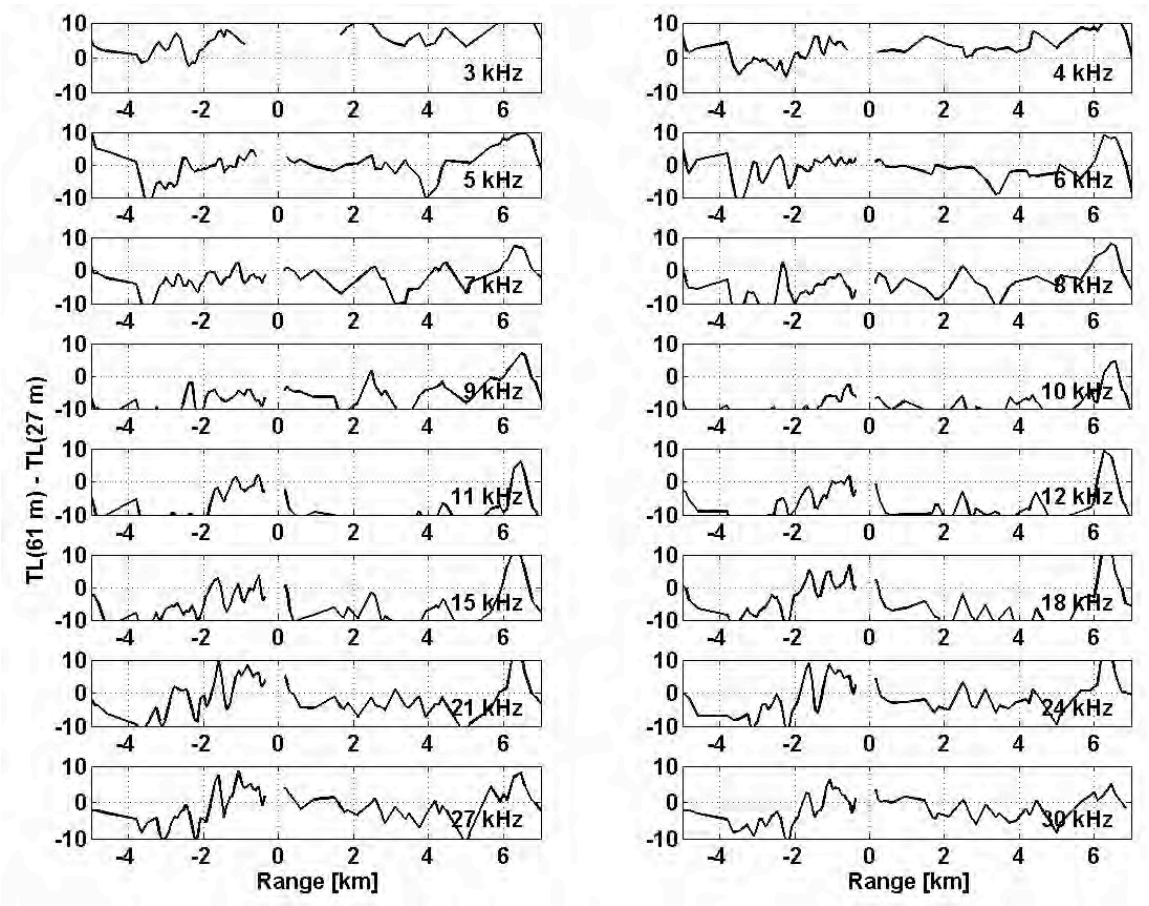

Figure 6.15 Difference in the measured TL at 61 m and 27 m at the 16 frequencies; location from Figure 1.2b (along the solid line). The values higher than 10 dB are not presented. Source depth was about 60 m and 35 m for (-) and (+) ranges, respectively.

In light of the discussion in Chapter 4, and taking into account the effect of the NL on the measurement accuracy, the unexpectedly lower short-range TL at the deeper

receiver on the right side of the experimental curves (Figure 6.14) is again partly caused by the higher NL at the deeper receiver.

The TL differences higher than 10 dB are not shown in Figure 6.15 and the other figures of this kind because it is sufficient to provide a rough estimate of a more optimal receiver depth with respect to TL.

According to Figure 6.15, the deeper channel had better transmission along the track except for the section between −2 km and the CPA. Along this section all the frequencies, except for 9 kHz and 10 kHz, were comparable in terms of TL, implying a direct-path arrival zone at both receivers.

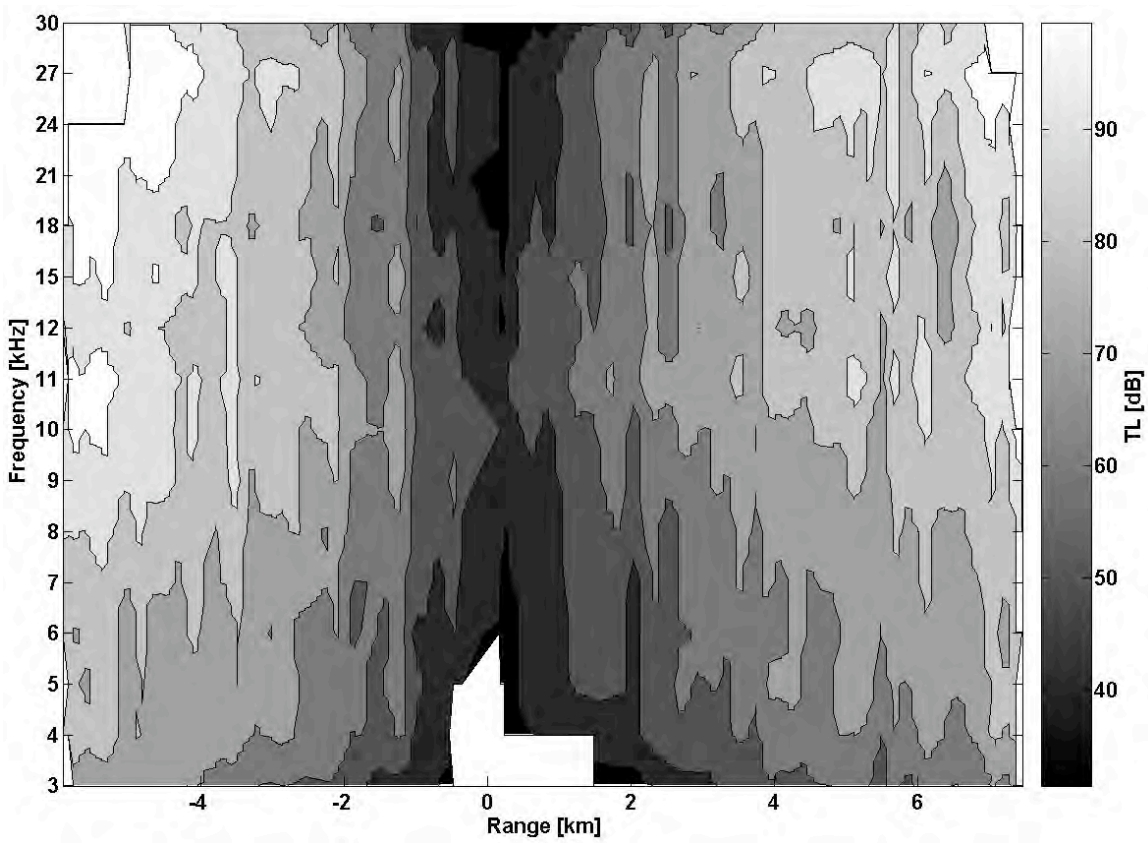

Figure 6.16 Contours of TL vs. range and frequency, location from Figure 1.2b (along the solid line); hydrophone depth 27 m. Source depth was about 60 m and 35 m for (-) and (+) ranges, respectively.

Frequencies below 6 kHz in Figure 6.16 exhibit lower TL at notably longer ranges than higher frequencies, whereas Figure 6.17 demonstrates more uniform distribution of TL in frequency for the given ranges. This may have been caused by the ray windowing and trapping of sound in the mixed layer; however, there was no evidence of the lower frequencies considered having better transmission throughout the experiment.

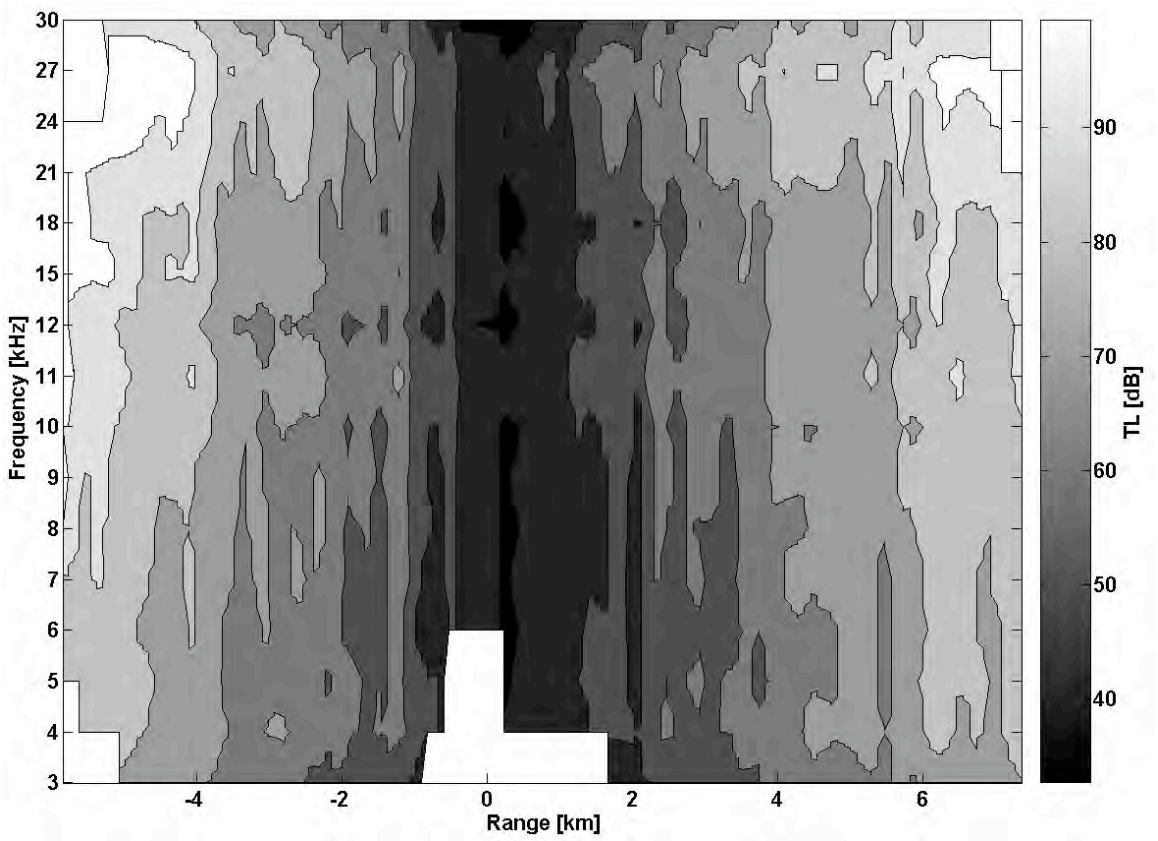

Figure 6.17 Contours of TL vs. range and frequency, location from Figure 1.2b (along the solid line); hydrophone depth 61 m. Source depth was about 60 m and 35 m for (-) and (+) ranges, respectively.

The second track at this site had the source transducer in the mixed layer all along. The direct-path distances on the left sides of the experimental curves in Figure 6.18, recognized as the ending points of the section where the measured TL curve does

not exceed spherical spreading plus absorption, are closer to the estimate in Table 6.4 that corresponds to the noon SSP, which implies similar mixed layer structure.

By comparing Figure 6.18 and Figure 6.13 it can be concluded that transmission in the shallower channel was better when the source transducer was in the mixed layer. If the conclusion is based on the less noisy left halves of the experimental curves, it can certainly be ascribed to ray windowing, for direct-path ranges, and ducting in the surface layer, for longer ranges.

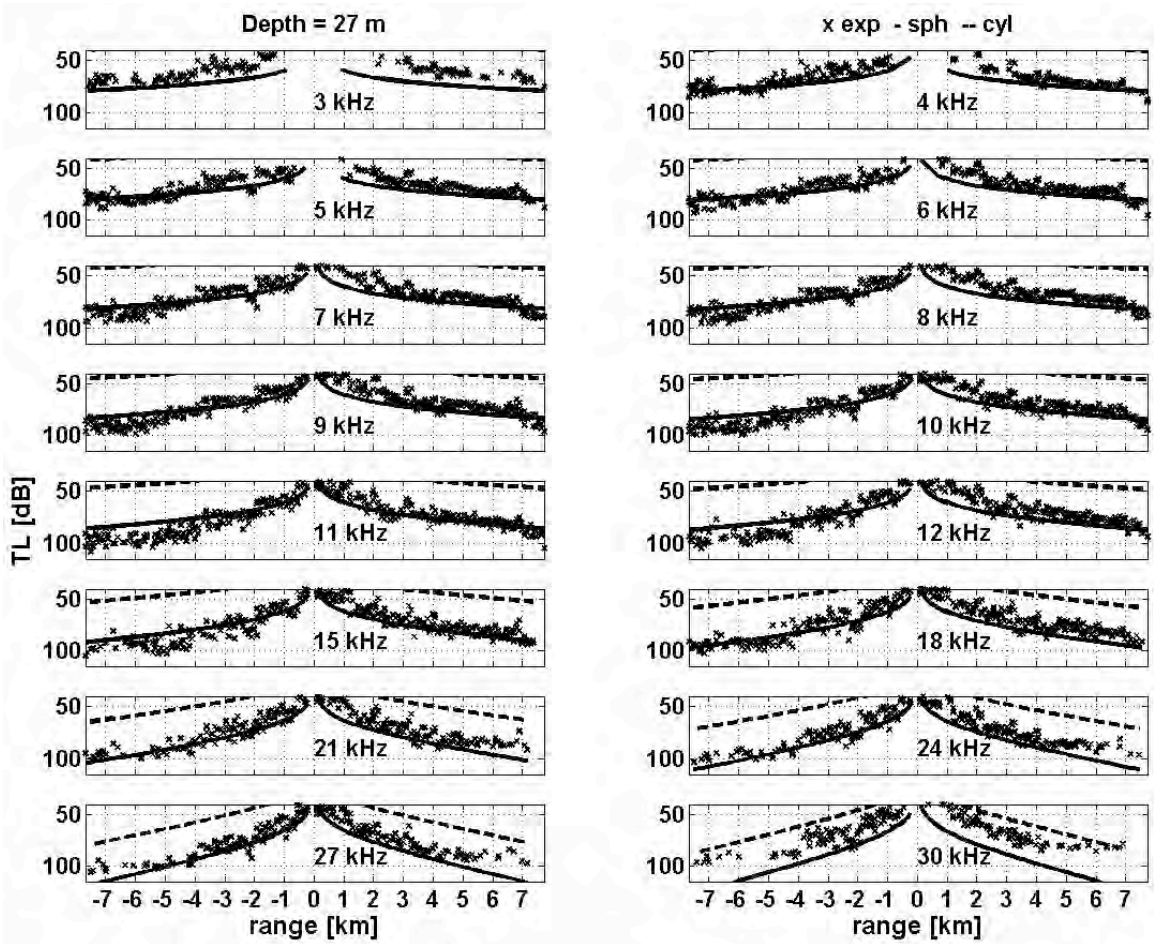

Figure 6.18 TL vs. range at the 16 frequencies; location from Figure 1.2b (along the dashed line); hydrophone depth 27 m. Source depth ≈ 18 m; *exp* = experimental; *sph* = spherical spreading plus absorption in water; *cyl* = cylindrical spreading plus absorption in water; absorption data from François and Garrison [31-32].

Figure 6.19 shows measured TL curves that do not exceed the spherical-spreading-plus-absorption model at the left sides of the experimental curves longer than in the shallower receiver case (Figure 6.18), which implies an SSP that resembles the 6 PM SSP (Table 6.4), when the mixed layer was shallower.

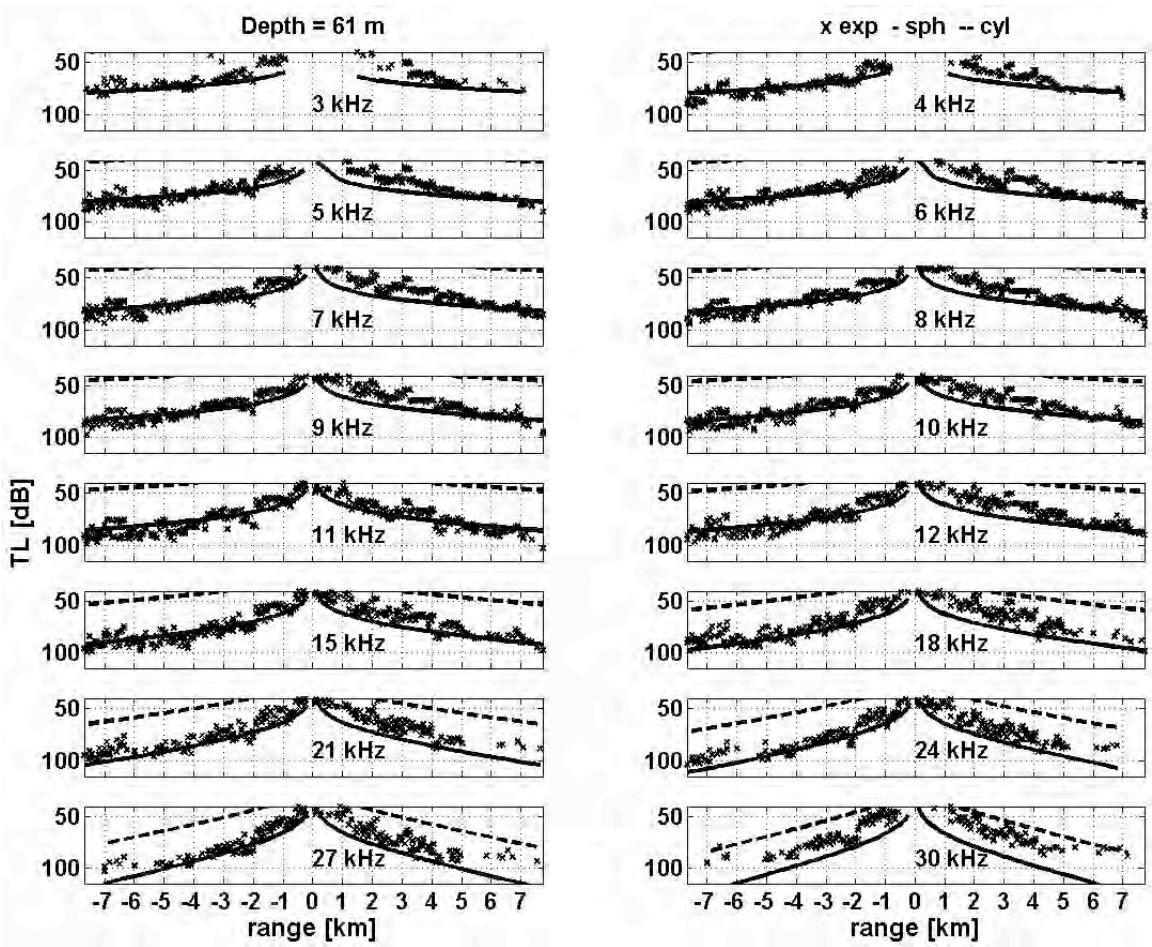

Figure 6.19 TL vs. range at the 16 frequencies; location from Figure 1.2b (along the dashed line); hydrophone depth 61 m. Source depth ≈ 18 m; *exp* = experimental; *sph* = spherical spreading plus absorption in water; *cyl* = cylindrical spreading plus absorption in water; absorption data from François and Garrison [31-32].

Figure 6.20 exhibits better transmission in the deeper channel than in the shallower channel between -7 km and -5 km, although the surface ducting should favor

the shallower receiver. In addition to the extended direct-path transmission at the deeper receiver depth, the contradiction might be caused by interference from the sea surface at the shallower receiver. The rest of the left side of the track is marked by approximately equal transmission.

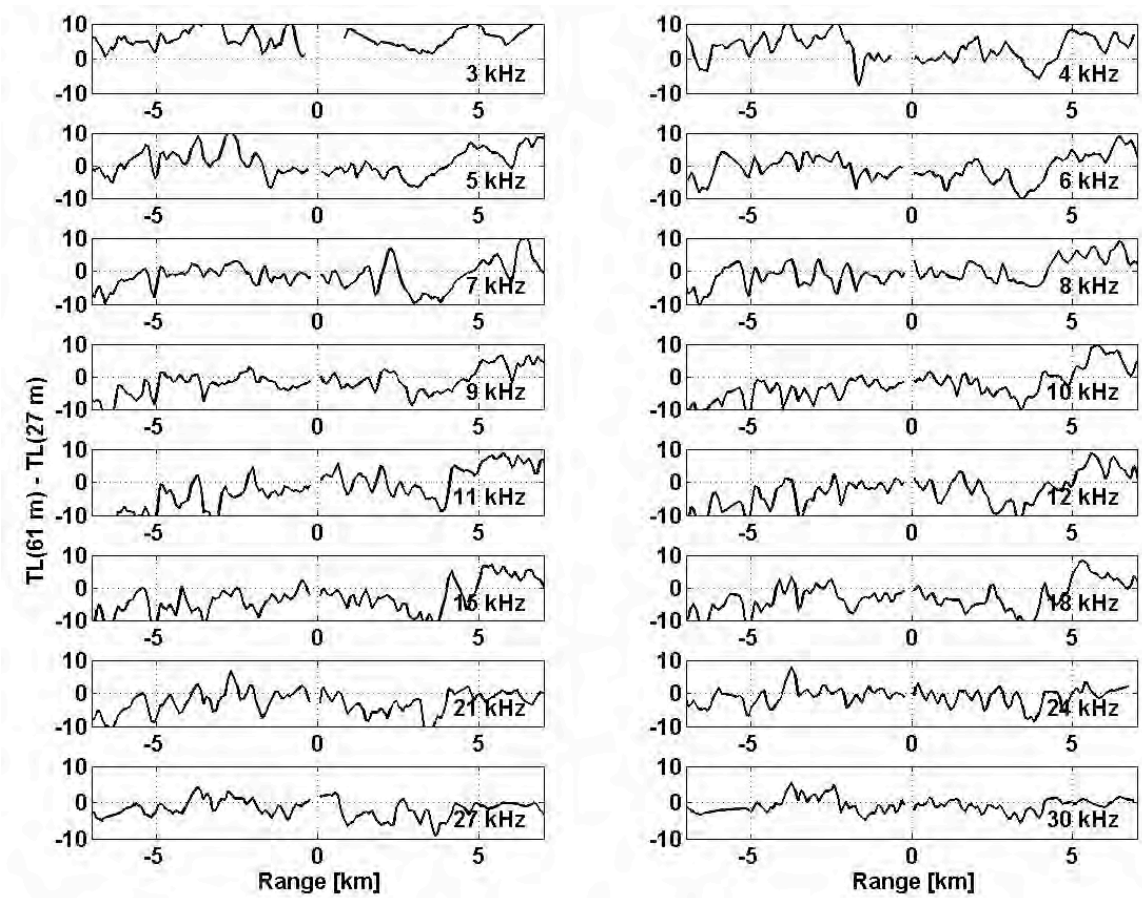

Figure 6.20 Difference in the measured TL at 61 m and 27 m at the 16 frequencies; location from Figure 1.2b (along the dashed line). The values higher than 10 dB are not presented. Source depth ≈ 18 m.

Figure 6.21 shows once again, at short/mid ranges, smoothly varying TL as a function of frequency inside frequency bands of a few kHz. For instance, at ranges as long as almost 2 km, 18 kHz and 9 kHz CW pulses have TL comparable to 11 kHz and 7

kHz CW pulses, respectively. It is an important clue for a sonar designer, with regard to advantages of higher frequencies, such as lower NL, as shown in Chapter 4.

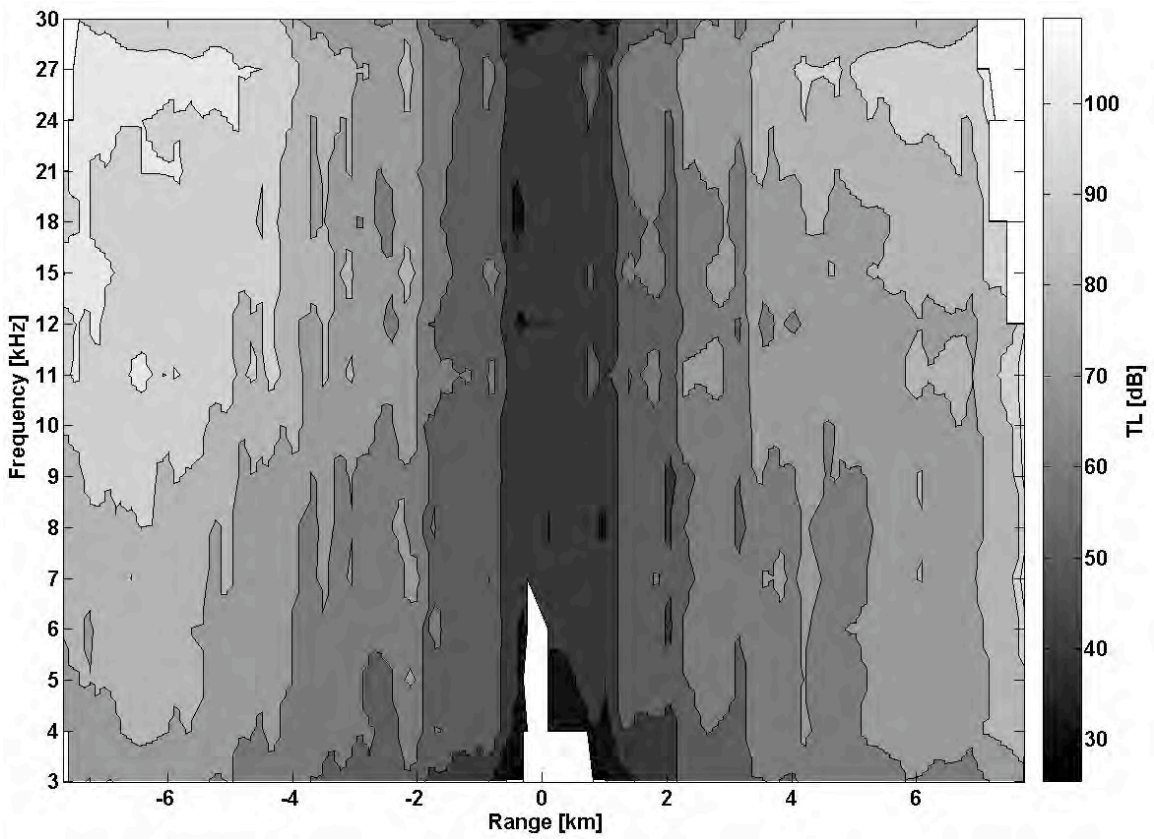

Figure 6.21 Contours of TL vs. range and frequency, location from Figure 1.2b (along the dashed line); hydrophone depth 27 m. Source depth ≈ 18 m.

The negative-range section in Figure 6.22 looks more consistent than its counter part in Figure 6.21, possibly because surface scatter is looser and direct-path distance is extended. It shows uniform TL between 4 kHz and 10 kHz at ranges shorter than 2 km, and between 11 kHz and 21 kHz, at ranges shorter than 1.5 km. Between −5 km and −4 km, and between −3.5 km and −2 km, there are zones of uniform TL in the frequency band between 5 kHz and 9 kHz.

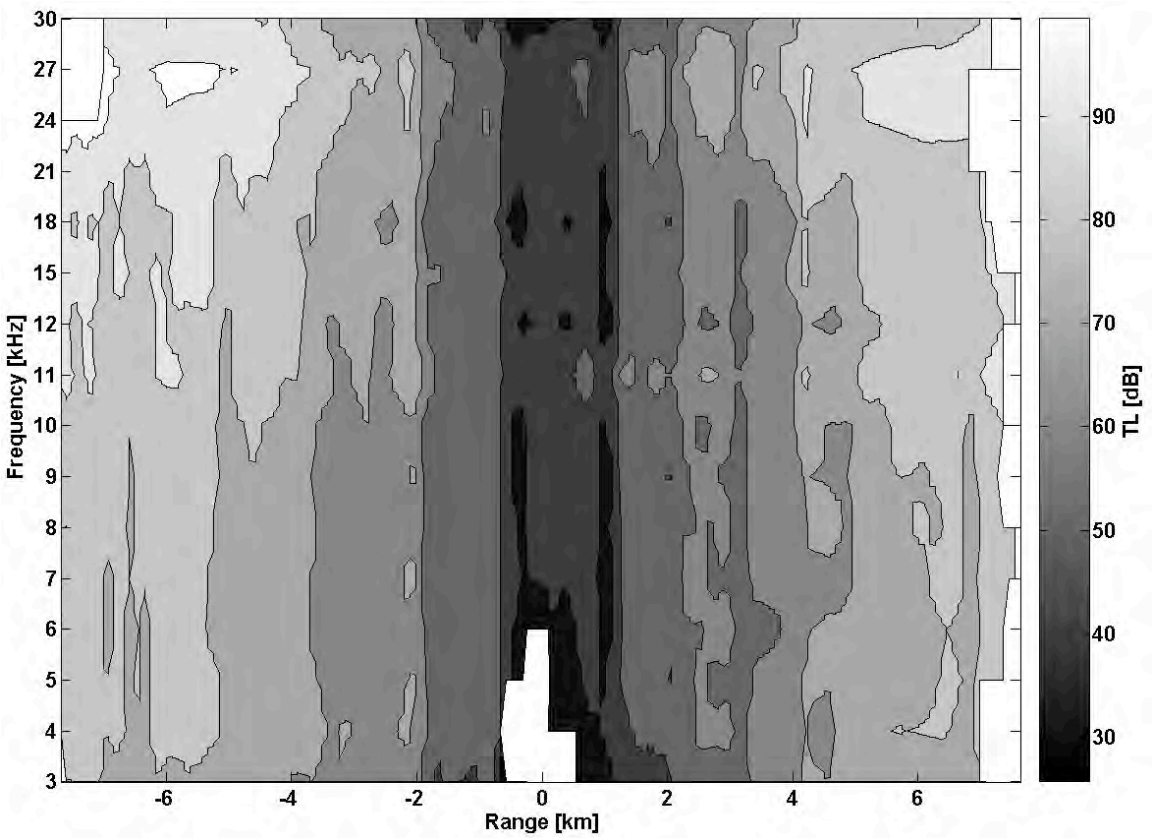

Figure 6.22 Contours of TL vs. range and frequency, location from Figure 1.2b (along the dashed line); hydrophone depth 61 m. Source depth ≈ 18 m.

San Nicolas Basin Site

In spite of being in deep water, a source transducer and hydrophones placed conveniently shallow cannot be considered to be under free-field conditions, especially at longer ranges, because sound propagation is affected by the sea surface reflections, ducting of sound in the mixed layer, and ray windowing that imposes limiting direct-path arrival range and shadow zones.

Source depth [m]	Receiver depth [m]	Noon	6 PM
13	27	4 km	2 km
	122	2.8 km	3.1km
83	27	2.5 km	2.3 km
	122	3 km	3.3 km

Table 6.6 Direct-path distances at the hydrophone depths, roughly estimated in Chapter 3.

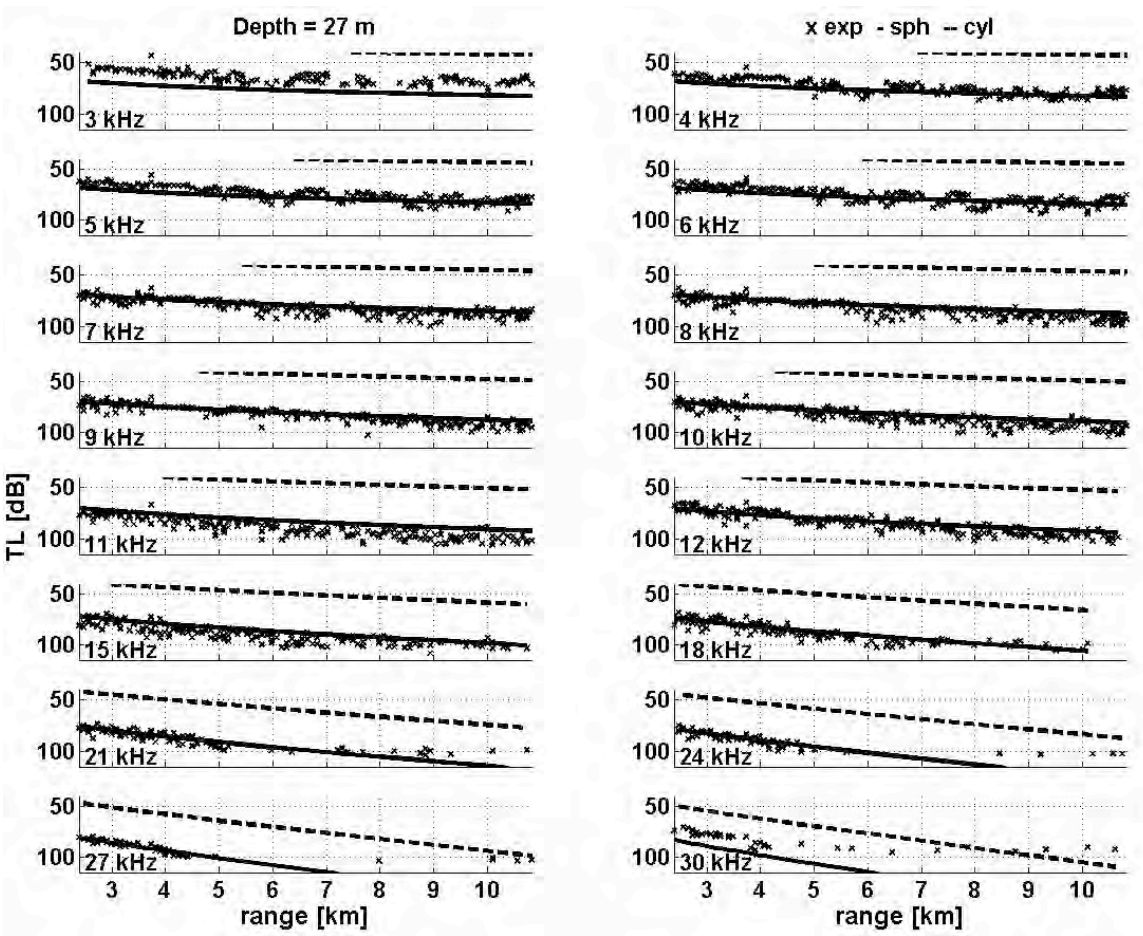

Figure 6.23 TL vs. range at the 16 frequencies; location from Figure 1.2c (along the solid line); hydrophone depth 27 m. Source ≈ 13 m; *exp* = experimental; *sph* = spherical spreading plus absorption in water; *cyl* = cylindrical spreading plus absorption in water; absorption data from François and Garrison [31-32].

The source transducer was kept at the depth of 13 m all along the first track (Figure 1.2c solid line). According to Figure 3.10 it was in the mixed layer with either the noon or the 6 PM SSP. The shallow hydrophone would be in the layer with the noon SSP, and below the layer with the 6 PM SSP. According to Table 6.6, the noon SSP would permit longer direct-path ranges. In Figure 6.23, the experimental TL curves do not exceed spherical spreading plus absorption at ranges longer than 4 km, implying that the noon SSP is a better match than the 6 PM SSP.

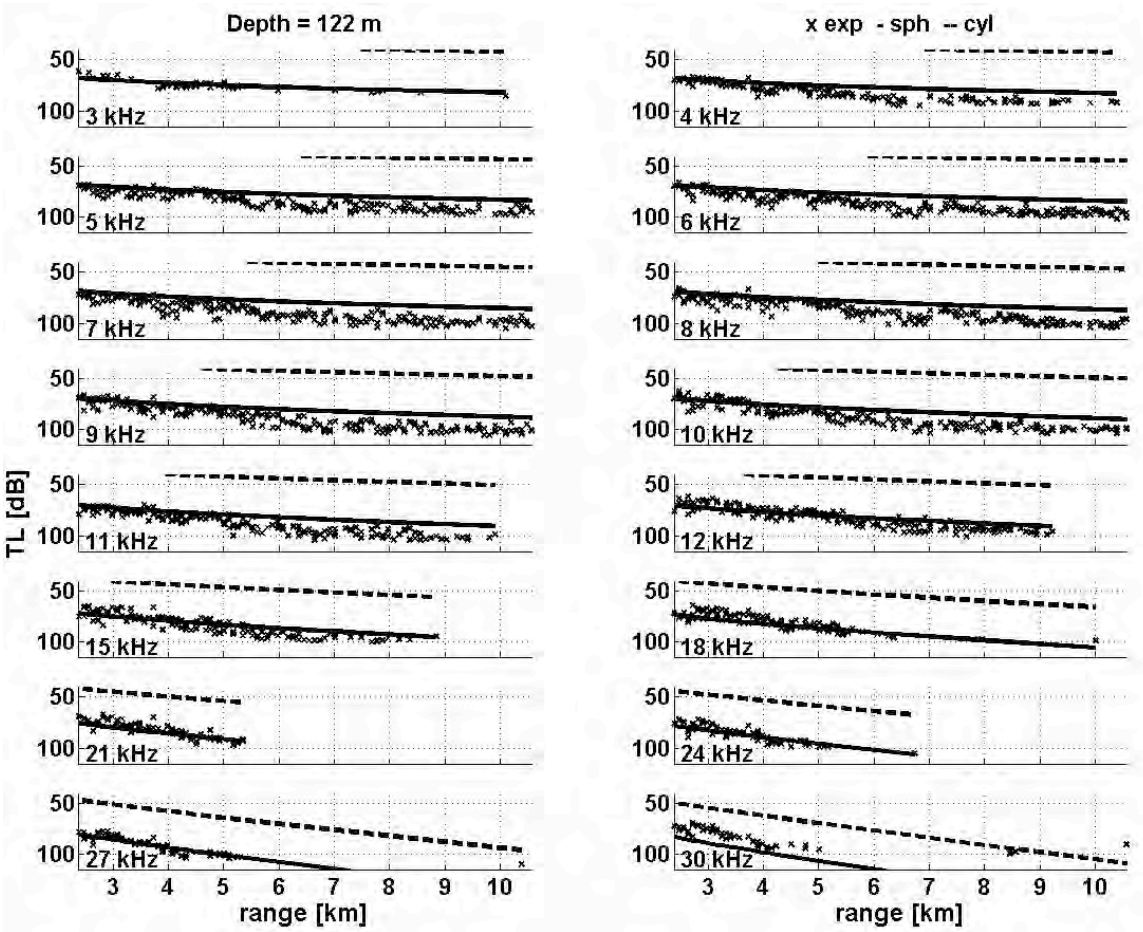

Figure 6.24 TL vs. range at the 16 frequencies; location from Figure 1.2c (along the solid line); hydrophone depth 122 m. Source ≈ 13 m; *exp* = experimental; *sph* = spherical spreading plus absorption in water; *cyl* = cylindrical spreading plus absorption in water; absorption data from François and Garrison [31-32].

The direct-path distance appears to be approximately 5 km in Figure 6.24. The anticipated value for either SSP in Table 6.6 is around 3 km, which may be a consequence of range uncertainty due to the freely drifting sonobuoys, as stated in Chapter 1.

Figure 6.25 implies better transmission at the shallower receiver than at the deeper receiver, past the direct path distance. The gain decreases with increasing frequency because additional absorption counteracts the ducting gain.

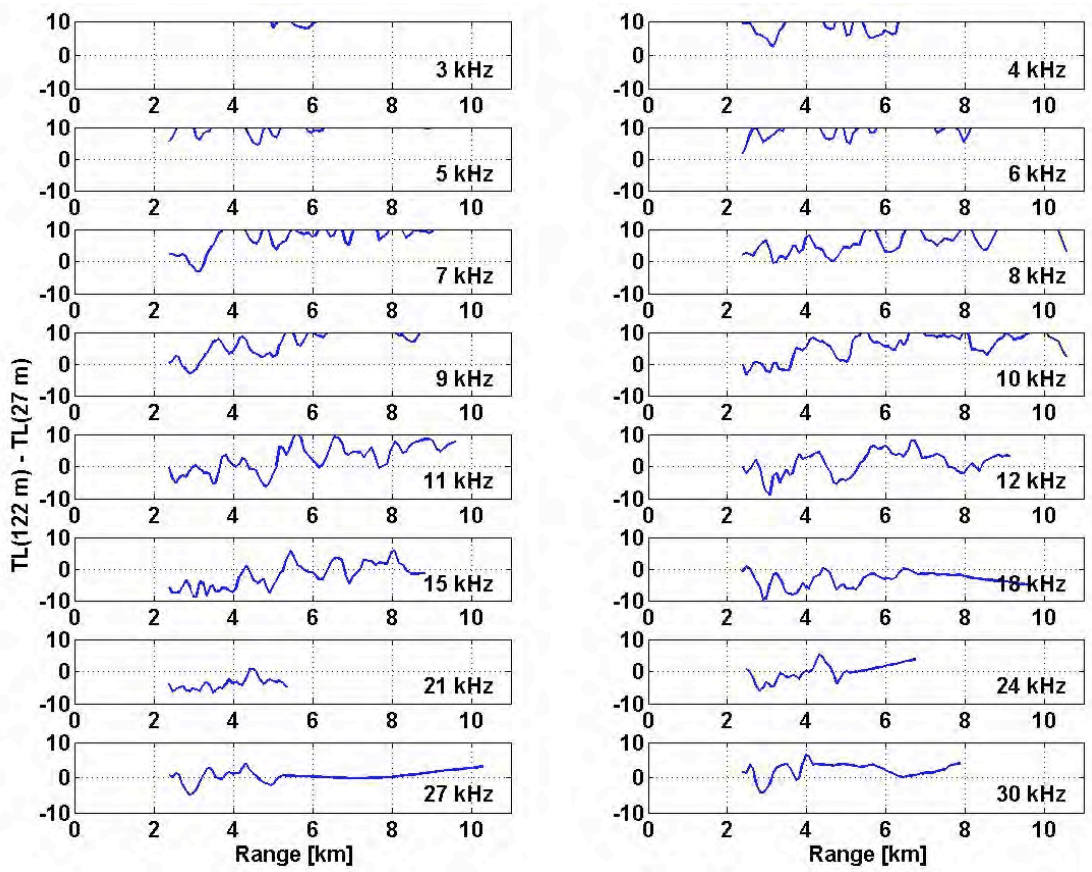

Figure 6.25 Difference in the measured TL at 122 m and 27 m at the 16 frequencies; location from Figure 1.2c (along the solid line). Source ≈ 13 m.

The TL plots in Figure 6.26 and Figure 6.27 are not very consistent. Nonetheless, the expected increasing trend of TL with increase in both range and frequency is noticeable. A lack of smoothness might be due to radiated noise, nonlinear effects such as dependence of sound speed on the pressure amplitude of the sound wave, volume or surface scattering, or a combination of these factors.

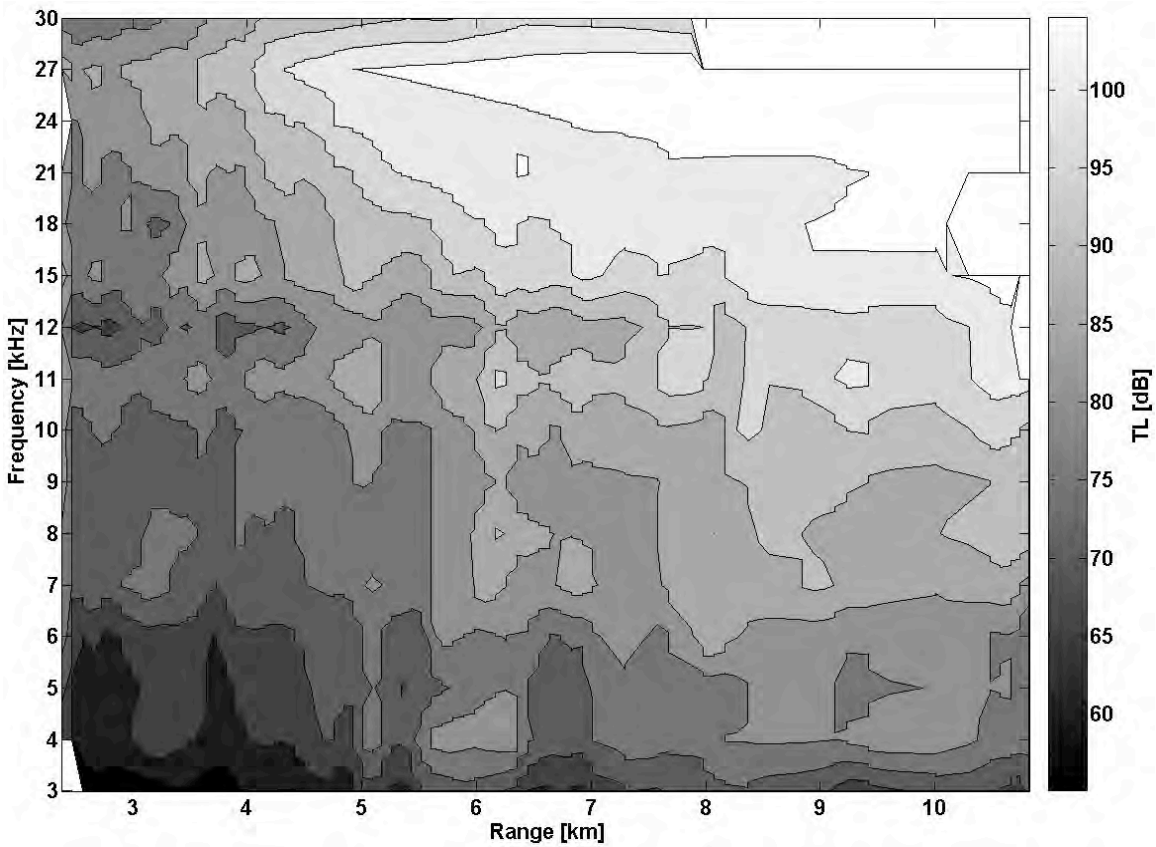

Figure 6.26 Contours of TL vs. range and frequency, location from Figure 1.2c (along the solid line); hydrophone depth 27 m. Source ≈ 13 m.

At the time when the source depth was changed on the second track at this site (Table 1.2), the horizontal range was approximately 1 km, which means that for most of

the time along the dashed line in Figure 1.2c, the source transducer was deployed at 83 m. Before that, the source transducer was most likely in the mixed layer (Figure 3.10).

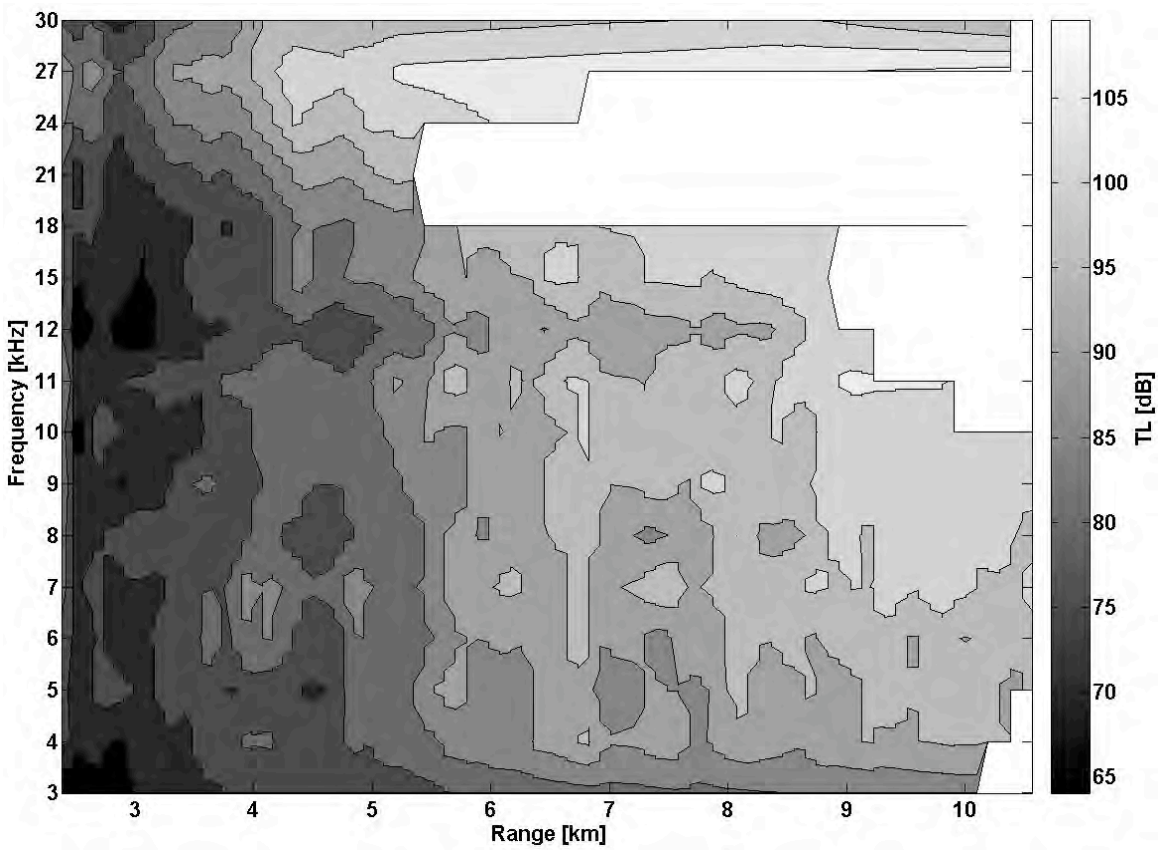

Figure 6.27 Contours of TL vs. range and frequency, location from Figure 1.2c (along the solid line); hydrophone depth 122 m. Source ≈ 13 m.

The direct-path distances in Figure 6.28, recognized as the range where the experimental TL curves exceed theoretical TL curves, appear to be close to 2 km; therefore, both SSPs in Table 6.6, for a source that is 83 m deep, give an estimate that is within half a kilometer of the observed experimental value. The first 1 km at frequencies between 10 kHz and 27 kHz appears to have TL that exceeds the theoretical model, although the range belongs to the direct-path zone. Even in the case of the noon SSP,

with the mixed layer shallower than 27 m, it should not be in the shadow zone at that range. A possible cause of this inconsistency may be vertical motion of the source during the gradual descent to 83 m.

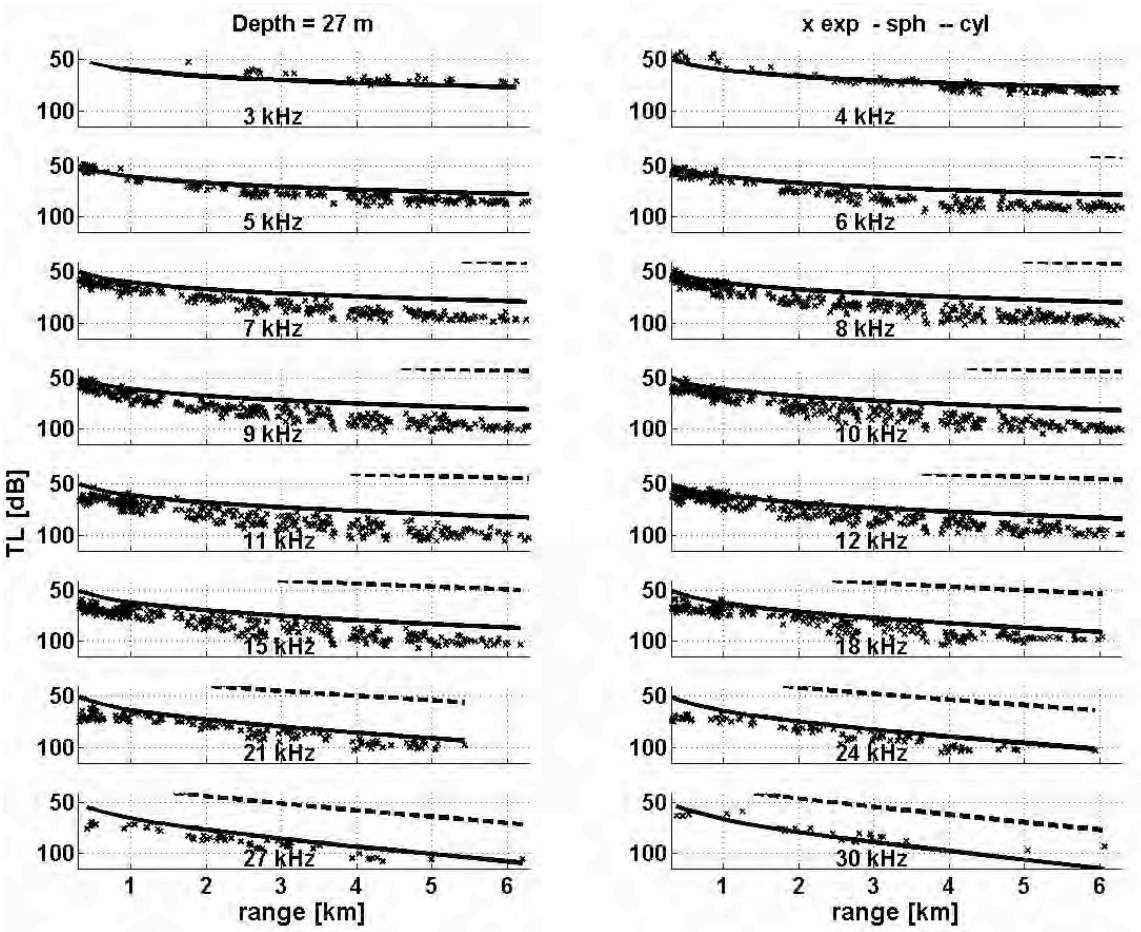

Figure 6.28 TL vs. range at the 16 frequencies; location from Figure 1.2c (along the dashed line); hydrophone depth 27 m. Source depth was about 13 m and 83 m before and after 1 km, respectively; *exp* = experimental; *sph* = spherical spreading plus absorption in water; *cyl* = cylindrical spreading plus absorption in water; absorption data from François and Garrison [31-32].

TL curves in the 4 kHz – 12 kHz plots in Figure 6.29 exceed spherical spreading plus absorption, starting between 2 km and 3 km, which give a reasonable match for both corresponding estimates of the direct-path distance from Table 6.6. The first 1 km

appears to have better transmission than the theoretical model. Background noise was much higher at the deeper hydrophone on this track, which could affect the transmission.

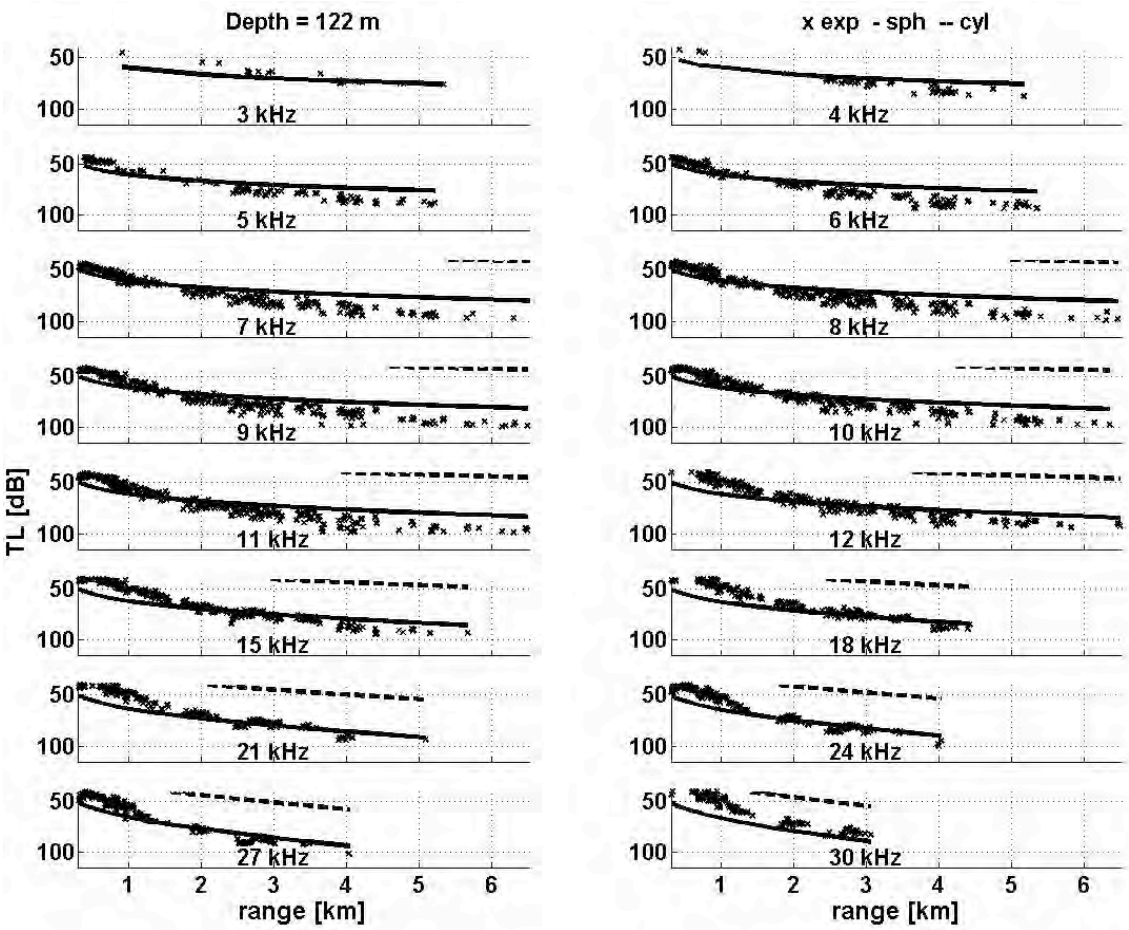

Figure 6.29 TL vs. range at the 16 frequencies; location from Figure 1.2c (along the dashed line); hydrophone depth 122 m. Source depth was about 13 m and 83 m before and after 1 km, respectively; *exp* = experimental; *sph* = spherical spreading plus absorption in water; *cyl* = cylindrical spreading plus absorption in water; absorption data from François and Garrison [31-32].

According to Figure 6.30, the deeper channel had better transmission than the shallower channel, although at 7 kHz and 8 kHz it changes past the 5 km zone. A disadvantage of the shallower receiver in this case, especially if it was in the mixed layer, is downward refraction that initiates the ray windowing mechanism (Figure 3.15).

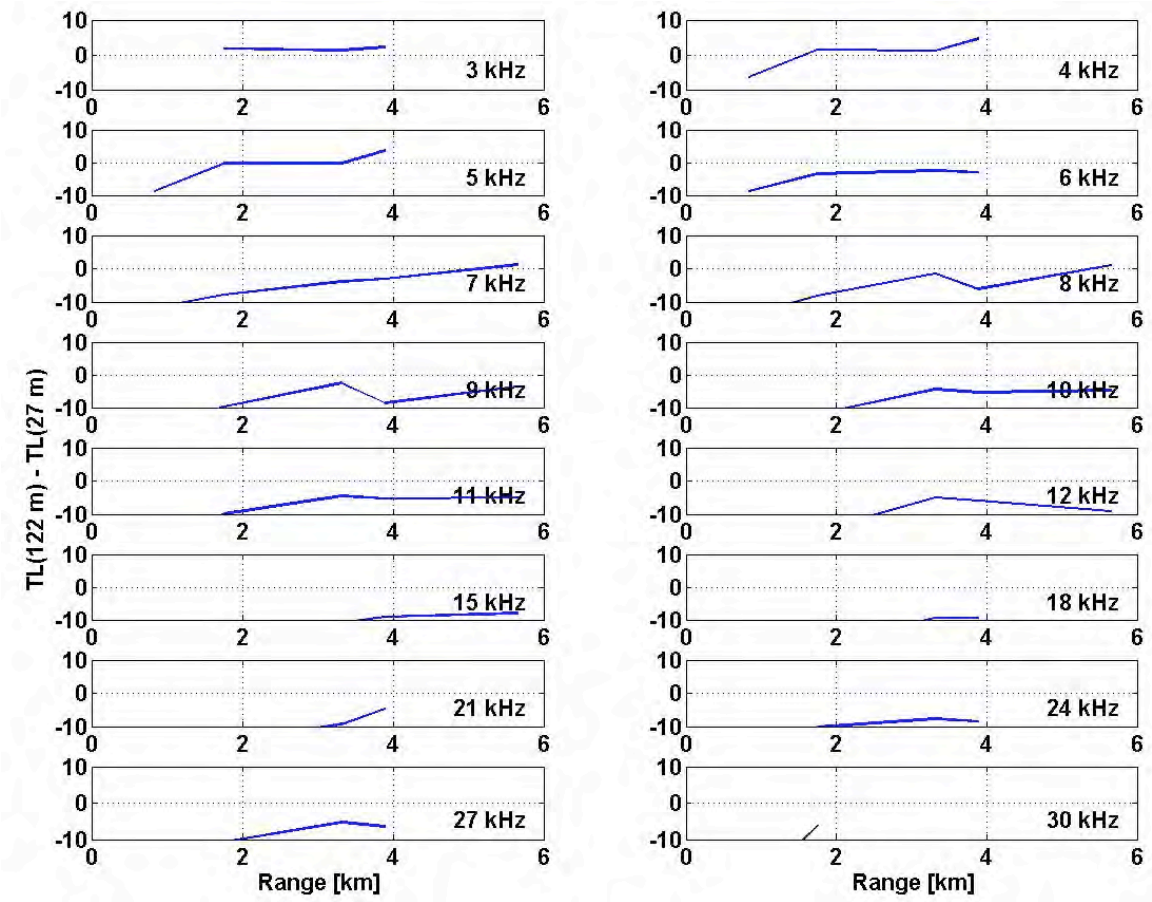

Figure 6.30 Difference in the measured TL at 122 m and 27 m at the 16 frequencies; location from Figure 1.2c (along the dashed line). Source depth was about 13 m and 83 m before and after 1 km, respectively.

The range-frequency function of the experimental TL shown in Figure 6.31 is less inconsistent in frequency than the one that corresponds to the other track at this site, probably because of lessened surface scatter due to the deeper source. Several zones are clearly defined and it appears that the first 3.5 km, has no significant impact of absorption in the 8 kHz to 11 kHz frequency band, as well as the first 1.1 km in the 15 kHz to 24 kHz frequency band.

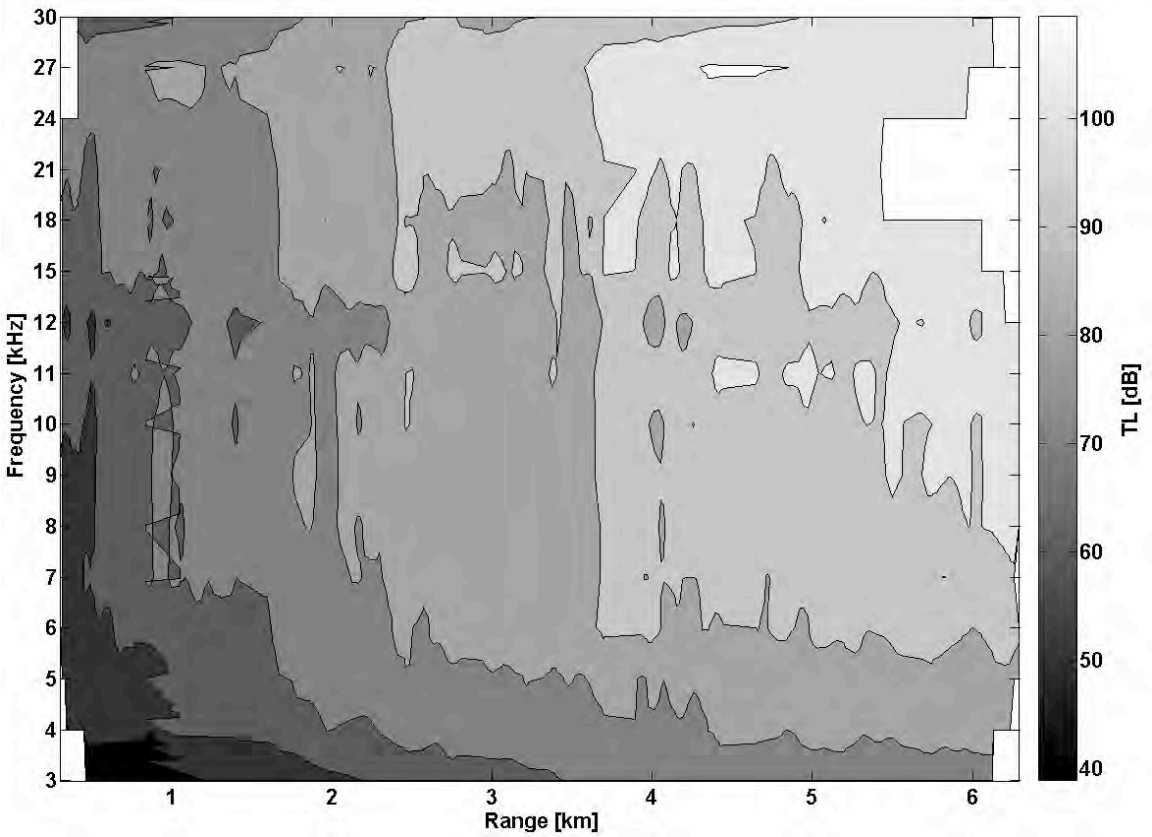

Figure 6.31 Contours of TL vs. range and frequency, location from Figure 1.2c (along the dashed line); hydrophone depth 27 m. Source depth was about 13 m and 83 m before and after 1 km, respectively.

As shown in Figure 4.7, the noise spectrum at the receiver at 61 m depth had a broad maximum around 15 kHz. The experimental TL at that receiver, as shown in Figure 6.32, features protrusion of lower TL zones, at frequencies between 12 kHz and 18 kHz, onto longer ranges than frequencies outside that band. This relation between the noise spectrum and TL existed at the shallower receiver on the second track at Tanner-Cortes Bank site, as shown in Figure 4.4a and Figure 6.11; therefore the unexpectedly low TL between 12 kHz and 18 kHz in Figure 6.32 is likely to be caused by the excess noise. Aside from that, a few hundred meter long zones of frequency-uniform TL, in the frequency band between 7 kHz and 9 kHz, can be recognized at ranges between 1.2 km

and 1.7 km; same applies in frequency band between 5 kHz and 9 kHz, at ranges between 2 km and 2.5 km, and between 3 km and 3.5 km.

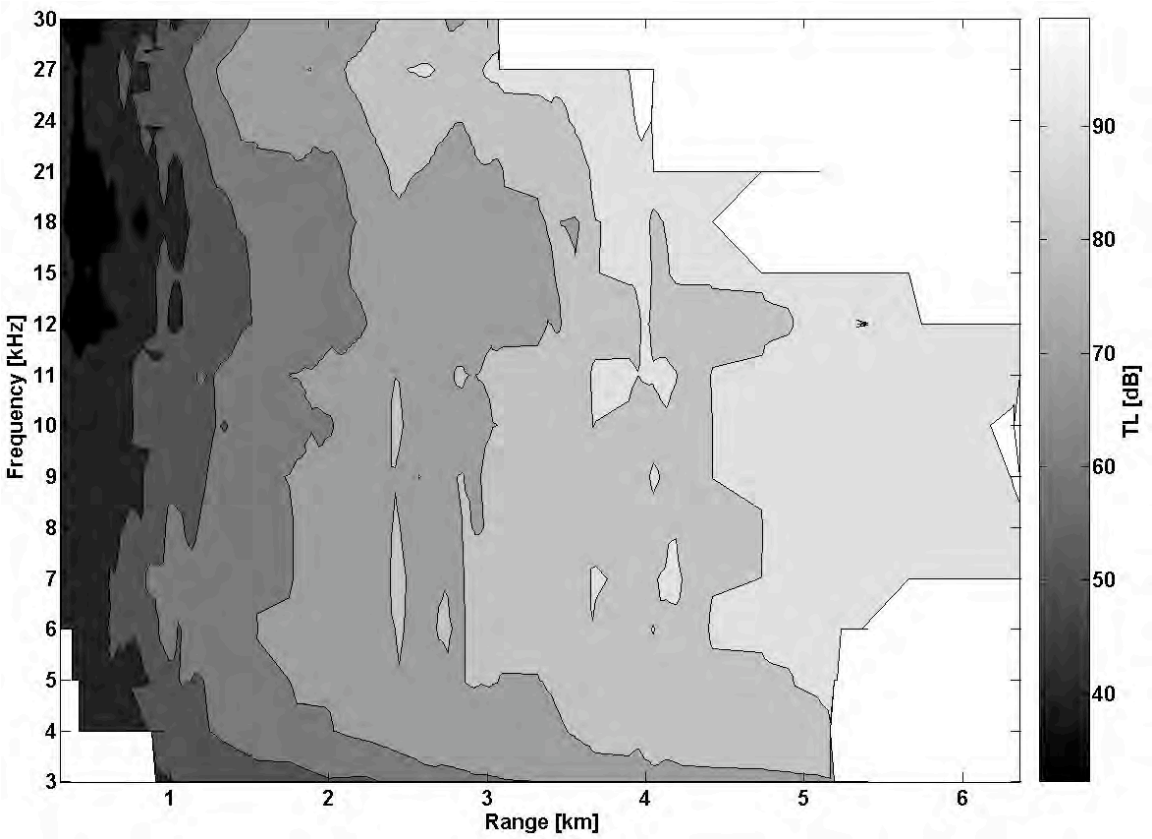

Figure 6.32 Contours of TL vs. range and frequency, location from Figure 1.2c (along the dashed line); hydrophone depth 122 m. Source depth was about 13 m and 83 m before and after 1 km, respectively.

CHAPTER 7

SUMMARY

Direct-path distances were estimated, using ray theory, as the maximum ranges at which direct-path arrivals can be expected, given a source/receiver depth. With a fairly intuitive approach, direct-path distances were experimentally determined as the ranges where the measured TL curves started exceeding the theoretical models of spherical spreading plus absorption.

At the Tanner/Cortes Bank site the experimental direct-path distances were, on average, 4 km long. It matched the prediction by the model of Marsh and Shulkin [3] within half a kilometer. During late morning hours, when the SSP was simply downward refracting without a distinct mixed layer, the hydrophone at 61 m depth had better transmission at long ranges than the shallower hydrophone. At 27 m depth, TL was uniform, up to 2.5 km, in the 3 kHz – 8 kHz frequency band; at 61 m depth, TL was uniform, up to 3 km, in the 6 kHz – 11 kHz, and in the 12 kHz – 21 kHz, frequency band. A layered afternoon medium caused sound channeling that increased direct-path distances, as anticipated by the ray-tracing simulations. That effect counteracted ray windowing to a certain extent, making the shallower receiver have better transmission than the deeper receiver, despite the source below the shallower-receiver depth. In frequency, spreading loss dominated, up to 2.5 km, in the 6 kHz – 10 kHz band, at 27 m depth. Shorter zones of uniform TL in frequency were observed at 61 m depth than at 27

m depth, possibly because of shorter spatial periodicity of the bottom-bounced rays in the bottom duct.

At the site south of San Clemente Island's China Point, when the source was 60 m deep (below the mixed layer), the experimental direct-path distances were approximately 3 km and 4 km for the receivers at 27 m and 61 m depth, respectively. For an 18 m deep source (in the mixed layer) the observed direct-path distance at 27 m depth was between 3 km and 4 km, depending on frequency, while at 61 m depth it was longer than that (exceeded the ranges considered here). Beyond the direct-path distance of the shallower receiver, when the source was 18 m deep, the deeper receiver had better or equal transmission, depending on frequency, than the shallower receiver. These results are in disagreement with both Urick's [2] representation of Marsh and Shulkin's model [4] and Ferla and Porter's [5] theory. Since both models were derived for deep water, it could be that strong reverberation in shallow water caused the mismatch. In addition, channeling of sound in complex SSPs, as explained in Chapter 3, makes it theoretically possible. When the source was 18 m deep, good transmission at the deeper receiver caused the experimental TL to be uniform, at 61 m depth, between 4 kHz and 10 kHz – at ranges shorter than 2 km, and between 11 kHz and 21 kHz – at ranges shorter than 1.5 km.

The experimental TL values from the San Nicolas Basin site indicated direct-path distances between 4 km and 5 km at the 27 m and 122 m deep receivers, when the source was 13 m deep, and between 2 km and 3 km for an 83 m deep source. When the source was 13 m deep (in the mixed layer), transmission was better at the shallower receiver than at the deeper receiver, past the direct-path distance. The gain decreased with increase in frequency, because additional absorption counteracted the ducting gain. When

the source was 83 m deep (below the mixed layer), transmission was better at the 122 m deep receiver than at the 27 m deep receiver. The fact that the transmission was better when the source and a receiver were both in/below the mixed layer is in agreement with Ferla and Porter's model [5] which implies that more optimal receiver depth is closer to the source depth. It is also in good agreement with Urick's [2] representation of the Marsh and Shulkin's model [4], however that study did not include a situation when a source is below the mixed layer and a receiver is in the mixed layer. When the source was 83 m deep, TL at the 27 m deep receiver had more uniform range-frequency dependence than at the 122 m deep receiver, showing no significant frequency variation in the 8 kHz – 11 kHz band at ranges shorter than 3.5 km, and in the 15 kHz – 24 kHz band at ranges shorter than 1.5 km.

Discussion

The results obtained in this thesis provide a rough estimate of TL variation with range and frequency in the study area. They can be used for recognizing the most convenient carrier frequency, for a given source/receiver depth, with respect to desired operating range, with a limitation to no longer than several kilometers. For example, south of China Point, if a communication link is not required to be longer than 1.5 km, with a source at 18 m depth (in the mixed layer) and a receiver at 61 m depth (below the mixed layer), carrier frequencies of 11 kHz and 21 kHz would have approximately the same TL, however lower noise and other common advantages of higher frequencies make 21 kHz a more desirable choice.

Another important indication that emerged from this work is the maximum direct-path range, for a given source/receiver depth, in the study region. Thus, in the aforementioned example, if longer ranges are needed, and efficient coherent communication is required – such that a direct-path link is desirable, the range can be extended to approximately 4 km, at the expense of around 10 dB higher TL.

The foregoing results should be annotated with a few disclaimers. First, the results are more reliable for the section of the track when the ship's propellers were not facing the hydrophones, because of the quieter conditions. Secondly, exact SSPs were not known for the measurement time window and a range-invariant environment was assumed. Thirdly, range uncertainty was particularly high at the San Nicolas Basin site due to the free-floating sonobuoys. Fourthly, the nonlinear effect of a dependence of sound speed on the pressure amplitude of the sound wave generated higher harmonics of the fundamental frequency, yielding additional loss that was not measured.

Radiated noise from the ship towing a source transducer can be reduced by extending the CPA. Another approach could be applying a noise reduction algorithm; however that would require a separate channel. On the other hand, radiated noise inevitably exists in all real communications and is therefore a valuable source of information. With regard to the nonlinear effect that created the harmonics, pre-windowing of a CW pulse, or using a wide-band signal of lower amplitude instead, could be suggested as a possible solution.

When a range exceeds direct-path distance, multipath arrivals are the only signals that a communication system can count on. They introduce additional TL due to scattering of sound from rough surfaces. Some parts of the experimental tracks here were

out of the direct-path bounds. Therefore boundary-interaction loss can be researched in the future, based on the corresponding signals.

After all, there are still unknowns about the TL of the direct-path signals. For the scope of this thesis, the TL was only compared to the theoretical models such as spherical spreading plus absorption, which is just a special case of sound propagation in homogenous medium. In order to explain disagreements between theory and real data, as pointed out in Chapter 6, models will be created that approximate TL across tubes of beams, for a transient signal source.

Coherence in time/frequency is an important issue that could be addressed based on the conducted experiment. Time/frequency spreading and phase deviation due to volume/surface scatters could be quantified for the given source/receiver depth, at the given carrier frequencies, in the study region. In fact, an important question is whether and how-efficiently could coherent communication be performed, at ranges in and out of direct-path bounds, for a given SNR. To that end, the available data from the reference hydrophone and the sonobuoy hydrophones can be compared with respect to phase.

Phase distortion and its variation with range and frequency could be a direction for future research. An example given in Chapter 5 indicated that the signals at frequencies higher than 15 kHz had more varying phase than the signals at frequencies below 15 kHz, considering direct-path pulse intervals. This matter should be researched to a fuller extent. Particularly important would be to see whether and how stable phase is within a pulse interval, depending on wavelength, SNR, volume/surface scatters, etc.

Further work on this project could also include additional simulations and more detailed sonar signal propagation analysis based on range dependent SSPs that could be obtained by putting together the CTD and the XBT measurements.

Noise power distributions, shown to have various patterns at different sites and depths, could get more attention in the future. For example, a software simulation of the entire experiment, including the radiated noise from the ship towing the source transducer, and bathymetry, could give answers to certain questions, raised in Chapter 4, such as the increasing noise spectrum slope of the self-noise in shallow water, or the broad maxima around certain frequencies in the noise spectrum. In addition, testing the existing and seeking new noise reduction algorithms could be based on results of the simulation.

It was shown throughout Chapter 6 that experimental TL could be lower than the free-field model at short ranges. Aside from sound trapping due to ray windowing, excess NL was shown to be related to unexpectedly low TL, within a certain frequency band, in a couple of cases. Both cases corresponded to sections where the ship towing the source transducer was moving away from the sonobuoys, which implied that the propeller noise was a potential problem. On the other hand, TL mismatch was often proportionally high, at short ranges, when the hydrophones were shaded from the propellers by the ship moving toward them and during the moving-away phase. This raises various questions, such as how-much and how-far the radiated noise really matters and how it depends on frequency.

Directional sonobuoys AN/SSQ-53 and AN/SSQ-77 were employed during the experiments and the available data can be used to gain better understanding of the environment, particularly background noise.

APPENDIX

APPENDIX A

RANGE-FREQUENCY VARIATION OF TRANSMISSION LOSS

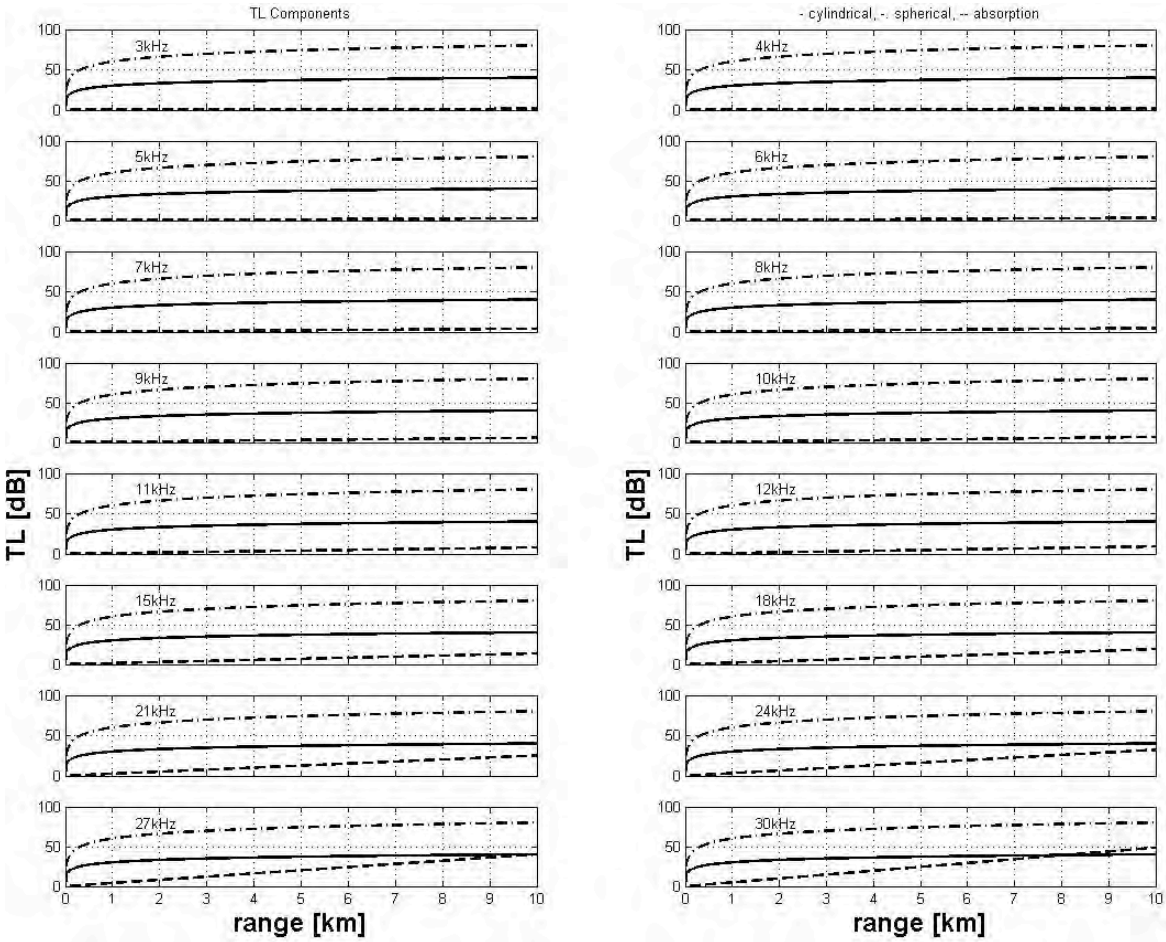

Figure A.1 Comparison of contribution of the generic components of theoretical TL model, spherical spreading, cylindrical spreading and absorption [31-32] in frequency. Assumed temperature for the absorption calculation is 14 °C.

The spreading losses and absorption in Figure A.1 are given separately. At long ranges, losses due to absorption usually dominate system design since they have exponential range dependence. However, at the ranges lower than 10 km spreading has

much higher impact on the transmission loss than absorption at frequencies lower than 18 kHz. As frequencies increases from 18 kHz to 30 kHz relevance of absorption increases more rapidly and at 30 kHz absorption exceeds cylindrical spreading around 8 km.

LIST OF ABBREVIATIONS

ADCP	Acoustic Doppler Current Profiler
AR	Auto Regressive
AUV	Autonomous Underwater Vehicle
CPA	Closest Point of Approach
CTD	Conductivity/Temperature/Depth
DIFAR	Directional Frequency Analysis and Recording
DT	Detection Threshold
FIR	Finite Impulse Response
FFVS	Free Field Voltage Sensitivity
FM	Frequency Modulation
GUI	Graphical User Interface
IIR	Infinite Impulse Response
ISI	Inter-Symbol Interference
LOFAR	Low Frequency Analysis and Recording
MA	Moving Average
NL	Noise Level
PSD	Power Spectral Density
RMS	Root Mean Square
SL	Source Level
SNR	Signal to Noise Ratio

SIO	Scripps Institution of Oceanography
SPL	Sound Pressure Level
SSP	Sound Speed Profile
TL	Transmission Loss
TVR	Transmit Voltage Response
VLAD	Vertical Line Array Directional Frequency Analysis and Recording
WGN	White Gaussian Noise
XBT	Expendable Bathythermograph

LIST OF REFERENCES

[1] Xiaolong Yu, "Wire-line quality underwater wireless communication using high speed acoustic modems", *Proc. OCEANS'00*, pp. 417 – 422.

[2] Urick, R.J., *Principles of Underwater Sound*, McGraw-Hill, 1983.

[3] Marsh, H. W., and M. Schulkin, "Shallow Water Transmission", *J. Acoust. Soc. Am.*, **34**, 863, 1962.

[4] ____, Report on the Status of Project AMOS (Acoustic, Meteorological and Oceanographic Survey), *U.S. Navy Underwater Sound Lab. Rep.* 255A, reprinted 1967.

[5] Ferla C. M. and Porter M. B., "Receiver Depth Selection for Passive Sonar Systems", IEEE J. Oceanic Eng., vol. 16, pp. 267 - 278, July 1991.

[6] Jensen, F.B., and Kuperman, W.A., "Optimum frequency of propagation in shallow water environments", *J. Acoust. Soc. Am.* **73(3)**, 813-819, 1983.

[7] Jensen, F.B., "Wave Theory Modeling: A Convenient Approach and Pulse Propagation Modeling in Low-Frequency Acoustics", *IEEE Journal of Oceanic Engineering*, vol. **13**, no. **4**, 186-197, 1988.

[8] Akal, T., *Effects of environmental variability on acoustic propagation loss in shallow water*, Impact of Littoral Environmental Variability on Acoustic Predictions and Sonar Performance – conference book, pp. 229-236, Kluwer Academic Publishers, 2002.

[9] http://www.mathworks.com

[10] Porter M. B. and Bucker H. P., "Gaussian beam tracing for computing ocean acoustic fields", *J. Acoust. Soc. Am.* **82**, 1349, 1987.

[11] Weinberg, H. and Keenan, R. E., "Gaussian ray bundles for modeling high-frequency propagation loss under shallow-water conditions", *J. Acoust. Soc. Am.*, **100(3)**:1421, 1996.

[12] Whalen, A. D., *Detection of Signals in Noise*, New York: Academic Press, 1971.

[13] Hermand, J-P., and Roderick, W., I., "Acoustic Model-Based Matched Filter Processing for Fading Time-Dispersive Ocean Channels: Theory and Experiment", *IEEE J. Oceanic Eng.*, vol. 18, pp. 447-465, Oct. 1993.

[14] http://www.itc-transducers.com

[15] http://www.fas.org/man/dod-101/sys/ship/weaps/an-ssq-57.htm

[16] Kinsler, L. E. et al, *Fundamentals of Acoustics*, 4th Edition, 2000.

[17] U. S. Department of the Interior, POCS Technical Paper No. 82-2, *Physical Oceanography and Meteorology of the California Outer Continental Shelf*, August 1982.

[18] N88-NTSP-A-50-8910B/A, "Approved NAVY Training System Plan for the NAVY Consolidated Sonobuoys", September 1998.

[19] Vaseghi, S.V., Advanced Digital Signal Processing and Noise Reduction, John Wiley, June 2000.

[20] Kay, S. M., Fundamentals of Statistical Signal Processing – Detection Theory, Prentice Hall, 1998.

[21] Proakis, J., G., and Manolakis, D., G., *Introduction to Digital Signal Processing*, Prentice Hall, 1988.

[22] Oppenheim, A. V., *Digital Signal Processing*, Prentice Hall, 1975.

[23] Chen, C.-T., and Millero, F., J., "Speed of Sound in Sea Water at High Pressure", *J. Acoust. Soc. Am.* **62(5)**, 1129-1135, 1977.

[24] Medwin, H., and Clay, C., S., *Fundamentals of Acoustical Oceanography*, Academic Press, 1998.

[25] Porter, M. B., and Jensen, F. B., "Anomalous Parabolic Equation results for propagation in leaky surface ducts ", *J. Acoust. Soc. Am.* **94**, 1510, 1993.

[26] Wenz, G. M., "Review of Underwater Acoustic Research: Noise", *J. Acoust. Soc. Am.* **51**(3), 1010-1024, 1971.

[27] National Oceanic and Atmospheric Administration (*NOAA*) - National Data Buoy Center, *Historical Data*, 2000 – 2001. URL: http://seaboard.ndbc.noaa.gov.

[28] P. D. Welch, "The Use of Fast Fourier Transform for the Estimation of Power Spectra", *IEEE Trans. Audio Electroacoust.*, Vol. AU-15, June 1970, pp. 70-73.

[29] Kaiser, J. F., "Nonrecursive Digital Filter Design Using the I_0-sinh Window Function*", Proc. 1974 IEEE Symp. Circuits and Systems*, April 1974, pp. 20-23.

[30] Oppenheim, A. V., *Applications of Digital Signal Processing*, Prentice-Hall, 1978.

[31] François, R.E., and Garrison, G.R., "Sound absorption based on ocean measurements. I Pure water and magnesium sulfate contributions", *J. Acoust. Soc. Am.* **72(3)**, 896-907, 1982a.

[32] ____, "Sound absorption based on ocean measurements. II Boric acid contribution and equation for total absorption", *J. Acoust. Soc. Am.* **72(6)**, 1879-1890, 1982b.

[33] Mackenzie, K. V., "Long-Range Shallow-Water Transmission," *J. Acoust. Soc. Am.* **33**, 1505, 1961.

[34] Rachel A. Romond, The Effect of Near-Surface Ocean Currents on High Frequency Underwater Acoustic Signal Intensity, M. S. Thesis, The Pennsylvania State University, May 2004.